

**DEFORMATION AND FRACTURE
OF THIN SHEETS OF NITINOL**

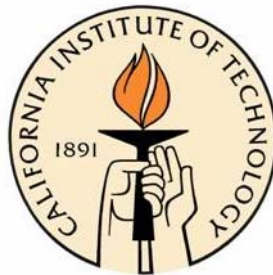
Thesis by

Samantha Hayes Daly

In Partial Fulfillment of the Requirements

for the Degree of

Doctor of Philosophy



California Institute of Technology

Pasadena, California

2007

(Defended May 10, 2007)

Dedicated to my family.

© 2007

Samantha Daly

All Rights Reserved

Acknowledgements

Thank you to the five members of my family. I don't know where I would be without your love and support. You mean the world to me.

This work would not have been possible without my advisors, Kaushik Bhattacharya and Guruswami Ravichandran. Thank you more than I can ever say for your absolute kindness and encouragement. I truly feel like I won the lottery having you as my advisors.

I gratefully acknowledge the support of the Army Research Office (W911NF-O4-1-0156), the National Science Foundation (DMS-0311788), and the Powell Foundation, for providing the funding that allowed me to do this work. I also thank Correlated Solutions, Inc., for providing the DIC Vic-2D software used in these experiments.

It is a pleasure to acknowledge the rest of my committee, Professors Chiara Daraio, Wolfgang Knauss, Alain Molinari, and Daniel Rittel, for their efforts and continued support. In particular, the experimental assistance that I received from Daniel Rittel during his visits to and sabbatical at Caltech has been invaluable in learning new techniques and approaches. Thank you to Petros Arakelian for his support and technical advice, as well as to the many other faculty and staff at Caltech for their advice, support, and the use of their labs - particularly, Richard Murray, who was a fantastic Master's advisor, Christopher Brennen, Nadia Lapusta, Ma Chi, Sosina Haile, Carol Garland, Jess Adkins, George Rossman, Ramon DeVera, and the Mechanical, Aerospace, and Physics shops on campus. Thank you to Vijay Chalivendra, Tracy Kidd, and Min Tao for help with the experimental setup and suggestions. I would also like to thank Sylvie Gertmenian, who has always made sure that my experiments were never delayed due to a lack of parts, and has helped me numerous times in other ways during my time at Caltech.

I have been fortunate enough to be a part of two research groups, and I am so appreciative of everything that I have learned from discussions with my colleagues in these groups. I have also been fortunate to have had the support and friendship of Nathalie Vriend, Mark Hesselink, Cindy Tognazzini, Lynn Burgess, Kaushik Dayal, Vikram Gavini, and Craig Vieregge during my time at Caltech. Last, but certainly not least, thank you to Elizabeth French, who in the past ten years has been with me through thick and thin. I am lucky to have found a friend like you.

Abstract

Nickel-Titanium (Nitinol) is a Shape Memory Alloy (SMA) that exhibits superelasticity (pseudoelasticity) and shape memory by a solid-solid state diffusion-less phase transformation. Phase transformation and the resulting strain localization in Nitinol has long been a topic of study, both for its inherent scientific interest and also because of the large number of practical applications of this bimetallic alloy. Although Nitinol devices are extensively used in the medical industry, there is a fundamental gap in the amount of high-quality quantitative experimental data detailing strain localization. The numerous applications of shape memory alloys provide the motivation to understand the deformation and failure mechanisms of these materials, particularly their fatigue and fracture behavior. By using an *in-situ* optical technique called Digital Image Correlation (DIC), quantitative measures of strain localization in Nitinol are presented for the first time in both deformation and failure modes. In addition, a finite element small-scale transformation analysis near a crack tip in Nitinol subjected to mode-I loading under plane stress conditions is performed for the first time. The experimental results and finite element analysis provide new and detailed insights concerning the structure of phase transformation and crack tip fields in Nitinol.

Table of Contents

Acknowledgements

Abstract

List of Illustrations

List of Tables

1. Introduction

1.1 The Discovery of Nitinol

1.2 Superelasticity and the Shape Memory Effect

1.3 Motivation

1.4 Digital Image Correlation

1.5 Outline

2. Stress-Induced Martensitic Phase Transformation in Thin Sheets of Nitinol

2.1 Introduction

2.2 Materials and Experimental Details

2.3 Experimental Observations

2.3.1 Uniaxial Tension Parallel to Rolling Direction

2.3.2 Uniaxial Tension in Various Orientations

2.3.3. Repeatability

2.3.4 Strain Fields around Surface Features

2.3.4.1 Surface Feature: Hole

2.3.3.2 Surface Feature: Notch

2.4 Discussion

3. An Experimental Investigation of Crack Initiation in Thin Sheets of Nitinol

3.1 Introduction

3.2 Material and Experimental Details

3.3 Results and Discussion

3.3.1 Stress Intensity Factor and Fracture Toughness

3.3.2 Fracture Surface

3.3.3 Strain Fields

3.3.3.1 Elastic Field

3.3.3.2 Phase Transformation Field

4. FEM Paper

4.1 Introduction

4.2 Constitutive Model

4.2.1 Auricchio-Taylor-Lubliner Model

4.2.2 Small Scale Transformation (SST) Analysis

4.3 Results

4.3.1 The Transformation Zone

4.3.2 The Stress Field

4.3.3 The Size of the Transformation Region

4.3.4 J-Integral

4.4 Sensitivity to Material Parameters

5. Summary

6. References

List of Illustrations

Figure 1.1: Stress-strain curve demonstrating the superelasticity of Nitinol, at a constant temperature above A_f

Figure 1.2: Amplatzer septal-defect occlusion device made of Nitinol, post-insertion

Figure 1.3: Stress-strain-temperature curve of Nitinol detailing the shape memory effect

Figure 2.1: The specifications of dog-bone test specimens

Figure 2.2: Optical micrograph of NiTi sheet at 60x at 3 different orientations: parallel to RD (1), perpendicular to RD (2), and 45 degrees to RD (3)

Figure 2.3: X-ray diffraction data of Nitinol thin sheets and corresponding reference pattern for Nitinol

Figure 2.4: Pole plots of crystallographic orientations $\langle 110 \rangle$ and $\langle 211 \rangle$, observed to have high intensity in the x-ray diffraction data of Figure 2.3

Figure 2.5: A schematic (top) and photograph (bottom) of the experimental setup. The schematic is adapted from a picture by D. Garcia, Ecole Mines des Albi, France.

Figure 2.6: The macroscopic response of a dog-bone specimen cut parallel to the RD with corresponding DIC images. The macroscopic response is the spatially averaged strain value from each DIC image plotted against the MTS stress value.

Figure 2.7: The corresponding DIC images for the ϵ_{xx} , ϵ_{yy} , and ϵ_{xy} strain components for the points 1-10 labeled in Figure 2.6, which shows the macroscopic response of a dog-bone specimen cut parallel to the RD.

Figure 2.8: The macroscopic response of a dog-bone specimen cut parallel to the RD with corresponding DIC images for ϵ_{xy} . The macroscopic response is the spatially averaged strain value from each DIC image plotted against the MTS stress value.

Figure 2.9: The loading curve from Figure 2.3, examining three specific points during the loading phase: prior to the appearance of any macroscopic localization (blue), halfway through the transformation when all the bands have nucleated and are nominally halfway through growing (green), and immediately after the coalescence of the bands with no remaining localization (red)

Figure 2.10: Strain down the centerline of a dog-bone specimen cut parallel to the RD during various localization stages

Figure 2.11: The uniaxial stress-strain response of various specimens with different orientations to the rolling direction

Figure 2.12: The variation of transformation initiation stress and transformation strain with orientation

Figure 2.13: An example of the crossing bands found in some specimens

Figure 2.14: Strain localization in a non-homogenous stress field: Hole. Panels (a) and (b) show the development of kidney-shape lobes, which grow and develop into crossing bands as strain continues to increase. The pictures are shown at different resolutions in order to capture the development of the strain. The top picture shows a snapshot full-field progression of band localization.

Figure 2.15: Strain localization in a non-homogenous stress field: Notch. Panels (a) and (b) show the development of lobes around the notch, which grow and develop into two symmetrically oriented bands as the strain increases. The pictures are shown at different resolutions in order to capture the development of the strain. The top picture shows a snapshot full-field progression of band localization.

Figure 3.1: Nominal (engineering) stress-strain curve for nitinol deformed in uniaxial tension at room temperature under a strain rate of 10^{-3} s^{-1}

Figure 3.2: Edge-cracked specimen geometry showing the coordinate system and dimensions. An idealized conception of various phase transforming zones near the cracktip is illustrated (1--Martensite, 2--Phase Transforming Zone, 3--Austenite). This figure is not to scale. The actual transformation regions are much more closely confined to the crack tip.

Figure 3.3: Fracture toughness (K_{Ic}) values obtained for thin ($\approx 150 \mu\text{m}$ thickness) sheet of Nitinol using an edge cracked specimen (see insert) for various values of (a/w)

Figure 3.4: Scanning electron micrographs of fracture surfaces in the vicinity of the crack tip for a crack oriented (a) along the rolling direction (RD), (b) 45 degrees from the RD, and (c) perpendicular to the RD

Figure 3.5: Full field normal (ϵ_{22}) strain fields obtained using DIC in the vicinity of the crack tip for various values of applied K_I (in $\text{MPa}\sqrt{\text{m}}$), (a) 25, (b) 33, and (c) 44. The field of view is 9 mm (width) by 7 mm (height).

Figure 3.6: Normal (ϵ_{22}) strain distribution along a line ahead of the crack tip at various values of applied K_I shown in the legend

Figure 3.7: Full field normal (ϵ_{22}) strain fields obtained using DIC in the close vicinity of the crack tip for various values of applied K_I (in $\text{MPa}\sqrt{\text{m}}$), (a) 28, (b) 38, (c) 47, and (d) 51. The field of view is 2 mm (width) by 1.6 mm (height). The field of view is a zoom of the region near the crack tip visualized in Figure 3.5.

Figure 3.8: Normal (ϵ_{22}) strain distribution as a function of distance along a line ahead of the crack tip at various levels of K_I shown in the legend.

Figure 3.9: Radius of the saturation zone (r_{SAT}) and phase transformation zone (r_{TRA}) as a function of $\frac{K_I^2}{2\pi\sigma_0^2}$. K_I is in $\text{MPa}\sqrt{\text{m}}$, σ_0 denotes the stress at which phase transformation begins, and is taken to be 500 MPa (see Figure 3.1). The radii of the saturation and transformation zones are in meters.

Figure 4.1 Schematic of a typical stress-strain curve for Nitinol. Schematic and nomenclature for material properties adapted from ABAQUS [52]

Figure 4.3 Typical shapes of saturation and phase transforming regions near the crack tip ($K_I=0.001$)

Figure 4.4 Angular variation of the normalized stress component σ_{11} versus θ for normalized $K_I=0.0005$, 0.00075, and 0.001 in the (a) fully transformed (martensite), (b) partially transformed (mixed phase), and (c) untransformed (austenite) regions. The theoretical (elastic) solution is compared only in the austenitic region.

Figure 4.4 Angular variation of the normalized stress component σ_{22} versus θ for normalized $K_I=0.0005$, 0.00075, and 0.001 in the (a) saturated (martensite), (b) partially transformed (mixed phase), and (c) untransformed (austenite) regions. The theoretical (elastic) solution is compared only in the austenitic region.

Figure 4.5 Angular variation of the normalized stress component σ_{12} versus θ for normalized $K_I=0.0005$, 0.00075, and 0.001 in the (a) saturated (martensite), (b) partially transformed (mixed phase), and (c) untransformed (austenite) regions. The theoretical (elastic) solution is compared only in the austenitic region.

Figure 4.6 Normalized stress component σ_{22} for material I as a function of distance ahead of the crack tip, along $\theta=0$, for varying levels of normalized K_I

Figure 4.7 Normalized crack opening displacement u_2 as a function of distance on a logarithmic scale along the crack face ($\theta=\pi$) for various values of $K_I=0.0005$, 0.00075, and 0.001.

Figure 4.8 The radii of the saturation and the transition zones ahead of the crack tip ($\theta=0$) as a function of normalized length scale $\left(K_I^2/2\pi\sigma_o^2\right)$

Figure 4.9 J_{tip} versus $J_{applied}$ (K_I^2/E_A) for various materials (I, II, III) of the material parameters. Note that J_{tip} is normalized with E_A and R .

Figure 4.10 Typical stress-strain curves of Nitinol (materials I, II, and III) used to study the effect of material parameters on small scale transformation analysis

Figure 4.11 Angular variation of the normalized stress component σ_{22} versus θ for normalized $K_I=0.001$ in the (a) fully transformed (martensite), (b) partially transformed (mixed phase) and (c) untransformed (austenite) regions, for various materials (I, II, III) of the material parameters. The theoretical (elastic) solution is compared only in the austenitic region.

Figure 4.12 Normalized stress component σ_{22} as a function of distance ahead of the crack tip, along $\theta=0$, for normalized $K_I = 0.001$ for various materials (I, II, III) of the material parameters

Figure 4.13 The radii of the saturation and transition zones ahead of the crack tip ($\theta=0$) as a function of normalized K_I for various materials (I, II, III) of the material parameters

Figure 5.1: Simultaneous digital image correlation and transmission x-ray setup at the Stanford Synchrotron Radiation Laboratory

List of Tables

Table 4.1 Chapter 4 nomenclature

Table 4.2 Convergence tolerance parameters used in equilibrium iterations

1. Introduction

1.1 The Discovery of Nitinol

In 1959, luck smiled on a man named William J. Buehler. As a metallurgist at the Naval Ordnance Laboratory, he had been assigned a project to develop metallic materials for the nose cone of the U.S. Navy Polaris re-entry vehicle. Buehler decided to focus on one of the sixty intermetallic alloys under consideration, a nearly equiatomic mixture of Nickel and Titanium (50 at.% Ni - 50 at.% Ti), which had a higher impact resistance and ductility than the other metals. This metal later became known as Nitinol, an acronym for Nickel-Titanium Naval Ordnance Laboratory. Buehler's personal recollection of his experience with this metal is recounted by Kauffman and Mayo in "The Story of Nitinol: The Serendipitous Discovery of the Memory Metal and Its Applications" [1]:

I distinctly remember my very exciting discovery of the acoustic damping change with temperature change near room temperature. This unusual event unfolded when my... assistant... and I were melting a number of [Nitinol] bars in the arc-melting furnace. On the day in question (circa 1959), six arc-cast bars were made. While cooling on the transite-topped table, the first bars arc-cast into bar form had cooled to near room temperature, while the last bars to be cast were still too hot... to be handled with bare hands. Between the cool (first bar) and the very warm (last bar) were four arc-cast bars possessing a broad spectrum of temperatures.... My "hands-on" approach caused me to take the cooler bar(s) to the shop grinder to manually grind away any surface irregularities that might produce a subsequent scaly or bad...surface. In going from the table to the bench grinder, I *purposefully* dropped the cool (near room temperature) bar on the concrete laboratory floor [a quick test to determine roughly the damping capacity of an alloy]. It produced a very dull "thud," very much like what one would expect from a similar size and shape lead bar. My immediate concern was that the arc-casting process may have in some way produced a multitude of micro cracks within the bar -- thus producing the unexpected damping phenomena. With this possibly discouraging development in mind, I decided to drop the others on the concrete floor. To my amazement, the warmer bars rang with a bell-like quality.

Because the bars had the same composition and processing history, Buehler correctly postulated that the acoustic damping change that occurred when varying the temperature of the bars had to be related to an atomic structural change. After further investigation, Buehler

also realized that Nitinol was, as he later recounted, “an overtly dimensionally mobile alloy capable of major atomic movement in a rather low temperature regime -- near room temperature” [1].

1.2 Superelasticity and the Shape Memory Effect

What later became evident is that Nitinol is not only “mobile,” as Buehler suggested, but can actually exist in two different solid state phases, and is capable of major atomic movement between these phases. The first phase, called *austenite*, is the high-temperature, stable phase. In Nitinol, the austenite phase is cubic. The second phase, called *martensite*, is the low-temperature, low-symmetry phase. In Nitinol, the martensite phase is monoclinic. When Nitinol transforms between the two phases, from austenite to martensite or from martensite to austenite, it is a solid to solid, diffusion-less phase transformation. The transformation between these two phases can be induced by changes in either temperature or stress. On heating, the macroscopic transformation from the martensite to the austenite begins at the austenite start temperature (A_s) and ends at the austenite finish (A_f) temperature. On cooling, the transformation from the austenite to the martensite begins at the martensite start temperature (M_s) and ends at the martensite finish (M_f) temperature.

The ability of Nitinol to transform between these solid states, austenite and martensite, enables two interesting and useful properties called *superelasticity* (pseudoelasticity) and *shape memory*. Superelasticity describes the ability of a material to elastically recover large strains. The typical strain that a material (for example, steel) can recover is on the order of 0.2%. Nitinol, which exhibits superelasticity, can elastically recover strains on the order of 6-8%. The stress-strain curve for Nitinol that is above the austenite finish (A_f) temperature, and at a constant temperature, is shown in Figure 1.1. Because it is above the austenite finish

temperature, the Nitinol at point O is in austenite. From point O to point A, the austenite is elastically loaded. At point A, the macroscopic transformation from austenite to martensite begins, and proceeds until point B, at which time the Nitinol is considered macroscopically martensite. From point B to point C, the martensite is elastically loaded. If one were to continue to load the martensite after point C, plasticity and eventual failure would result. It is seen in Figure 1.1 that the majority of the recoverable strain is achieved in the flat plateau between points A and B, where the transformation between austenite and martensite is taking place. From points C to D, the martensite is elastically unloaded. From points D to E, the monoclinic martensite transforms back into cubic austenite. The reversion back to austenite occurs with no permanent strain because the austenite is unique, and no bonds are broken during the transformation. From points E to O, the austenite is elastically unloaded and the original position with no permanent strain is recovered.

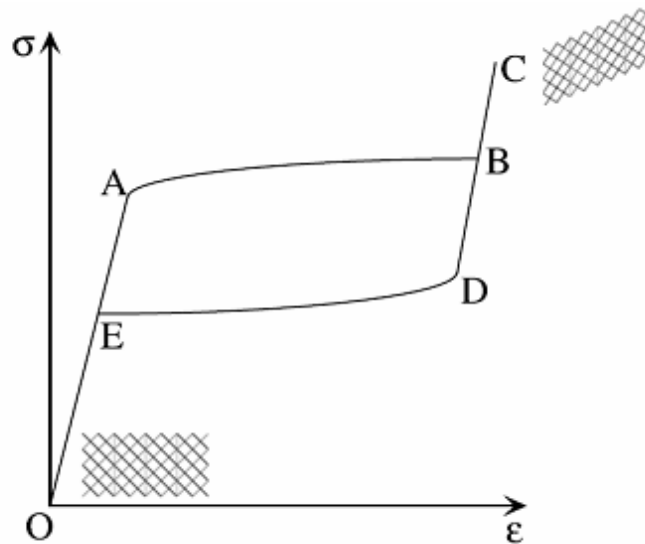


Figure 1.1: Stress-strain curve demonstrating the superelasticity of Nitinol, at a constant temperature above A_f

Superelasticity is useful in a wide variety of practical applications, most notably in the biomedical industry, in the form of stents, vena-cava filters, braided catheters, surgical tools, etc. [2]. One example illustrating the superelastic property in biomedical applications is shown in Figure 1.2, which shows an Amplatzer septal-defect occlusion device made of Nitinol that has been placed to seal a hole in the heart wall. Because Nitinol is superelastic, each side of the occlusion device can be tightly compressed and wrapped around a catheter. Instead of opening the chest in order to install this occlusion device, the device is then inserted on the two catheters through a vein, generally in the leg, and moved through the body to the heart. The two sides of the patch can then be placed into position and used to seal the hole in the heart wall with a special torquing catheter in a much less intrusive procedure than would be possible with traditional materials. This technique leads to significantly less mortality and a shorter hospital stay.



Figure 1.2: Amplatzer septal-defect occlusion device made of Nitinol, post-insertion

Although there are several metals that exhibit superelastic effects, only Ni-Ti-based alloys appear to be chemically and biologically compatible with the human body [3]. In addition to being biocompatible, Nitinol is also MRI compatible, kink resistant, corrosion

resistant, and has the ability to maintain a constant stress. Because of these properties, and its high range of recoverable strain, Nitinol is by far the most commonly used shape memory alloy, particularly in biomedical and MEMs applications.

The transition from austenite to martensite also enables what is known as the shape memory effect. If one takes a wire of Nitinol, deforms it, and then heats it past a set transformation temperature, it will return to its original shape – hence, the term “shape memory.” The stress-strain-temperature curve that occurs during this process is detailed in Figure 1.3. At first, the wire of Nitinol is twinned martensite at point F, which is below the M_f temperature. To explain the terminology ‘twinned martensite,’ recall that the austenite has higher symmetry (cubic) compared to the martensite (monoclinic). Therefore there are twelve symmetry-related variants of martensite: crystals with identical structure but oriented differently with respect to the austenite. These different variants can coexist in very characteristic mixtures, and these mixtures are called twinned martensite.

From point F to G, the twinned martensite is then stressed (deformed) until it is detwinned martensite (single variant of martensite). Further loading causes the detwinned martensite to load elastically from point G to point H. When the stress is released, the detwinned martensite unloads elastically from point H to point I. In particular, the strain does not recover to point F. The reason is that all variants of martensite, and consequently the twinned and detwinned martensite, have the same energy. Therefore there is no energetic driving force to compel the detwinned martensite back to the twinned martensite. This strain, however, is then recovered by heating above A_f as the material goes from point I to point O. During heating, each variant of martensite transforms back to the unique austenite thereby recovering the strain. As the wire cools, from point O to point F, the

microstructure reverts back to twinned martensite and the process is back to its starting point.

The shape memory effect has been used in aerospace applications, including Nitinol latches on the solar panels of the Hubble Space Telescope. These latches kept the solar panels down until it was safe to deploy them, at which point the latches were heated and returned to their original (unlatched) shape, releasing the panels [4].

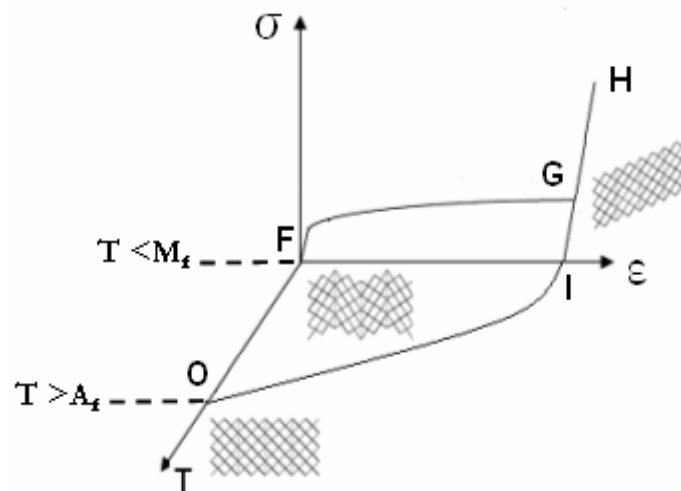


Figure 1.3: Stress-strain-temperature curve of Nitinol detailing the shape memory effect

2.3 Motivation

The unique properties of shape memory alloys make these materials, and in particular Nitinol, attractive for a variety of applications. Important amongst these are stents, guidewires, and other bio-medical applications, where relatively slender structures are subjected to rather complex deformation. These motivate us to understand the deformation and failure mechanisms in these materials.

A broad overview of the heuristics of transformation has been described in Section 2.2. However, the specific details of this transformation are still not fully understood. The transformation is not homogenous, a fundamentally important feature that is not apparent in the macroscopic stress-strain-temperature picture. Under laboratory conditions, there are regions of martensitic transformation that nucleate and grow inhomogeneously throughout the material. In addition, we rarely see single crystals -- in practice, what we have are polycrystalline shape memory alloys, where there are multiple grains. These grains are comprised of identical material, but they are oriented differently with respect to one another. Cold working, hot working, and annealing are commonly used techniques used to meet the thermo-mechanical property requirements of Nitinol that are specified by the consumer. These and other processes invariably create complicated textures, resulting in a much more complex transformation behavior than the broad overview presented in Section 2.2.

Although the mechanism of transformation is reasonably well understood in single crystals (see, for example, [5, 6] and the references therein), it is incompletely understood in polycrystals. What is currently known is that during the stress-induced transformation from austenite to martensite, strains in Nitinol localize as phase transformation occurs -- that is, the material deforms in one region and not elsewhere. This phenomenon has been well established through several different experimental techniques (see, for example, [7 - 9] and the references therein). In 2004, Brinson et al. [10] looked at stress-induced transformation behavior in polycrystalline Nitinol on both the macro- and microscopic scale, via *in-situ* microscopy. What she found was that “in contrast to the perception that transformation occurs only in the macroscopically visible transformation bands ... the martensitic transformation occurs throughout the material at all strain levels.” Even when a strained region was macroscopically austenite, there existed significant martensitic variants

throughout the grains when viewed microscopically. These and other experiments [6,11 - 14] point to a much more complex transformation mechanism in polycrystalline shape memory alloys than previously assumed, in part due to intergranular constraints. Intergranular constraints arise during transformation due to the fact that during transformation in a polycrystal, there are grains that are favorably oriented for transformation, and grains that have orientations unfavorable for transformation. When favorably oriented grains transform, they change the local stress state, and can cause other untransformed grains to self-arrest. The results of Brinson et al. [10] show that even at a macroscopically full transformation of the specimen (i.e., 10% global strain), the actual martensitic transformation of polycrystalline Nitinol arrests at around 60 - 70%.

It has been observed that localized transformation occurs at all scales throughout the material, and that processes occurring on one scale can significantly influence the properties of another. What is currently missing from the experimental literature is a full-scale measurement of the localized strain during transformation. There have been recent experiments utilizing Transmission Electron Microscopy (TEM) to measure nanoscale strain fields around Ni_4Ti_3 precipitates [15] and to observe stress-induced martensitic transformation in Nitinol [13, 14]. This technique is an excellent method of obtaining high-resolution images of martensitic formation on the nanoscale, but an obvious limitation of these measurements is the exceptionally small region to which they are confined. The combination of these precise nanoscale strain measurements with a macroscopic full-field picture of the deformation has the potential to greatly enhance our understanding of the mechanisms behind martensitic transformation. This thesis provides, for the first time, a method for full-field quantitative strain mappings of localization as a means for tracking martensitic transformation. This information, combined with the spatially averaged

macroscopic stress-strain behavior, provides new and valuable information for understanding and modeling the behavior of deformation in Nitinol.

This thesis also discusses phase transformation near the crack tip in fracture. Full-field quantitative strain mappings of localization near the crack tip are obtained for the first time, and the K_{IC} value for plane strain fracture toughness is experimentally determined for thin sheets of Nitinol ($\approx 150 \mu\text{m}$). In the past, there have been numerous experiments on fracture fields in single-crystal shape memory alloys (see for example [16 - 19]). Many of these experiments were designed to give unconstrained microstructures, but most applications utilize polycrystalline materials, where there are significant intergranular constraints. This thesis addresses a clear need for experiments detailing the process of fracture in the presence of these microstructural constraints. The experiments detailed within this thesis are the first strain fields obtained for fracture in polycrystalline Nitinol.

Previously, there was also a limited knowledge of the fracture toughness of Nitinol and no determined value for thin sheets. The experiment described in Chapter 3 provides the first quantitative measurements of fracture toughness for polycrystalline thin sheets of Nitinol. The strain fields and fracture toughness measurements provide new information that expands our knowledge of how this martensitic transformation proceeds, and the effectiveness of the transformation in cracktip shielding and transformation toughening.

When considering practical applications, the localized deformation that occurs during phase transformation can affect the performance of Nitinol devices and accelerate failure. As a simple example of how strain localization can affect performance, consider a MEMS pump. If the pump is deforming to a greater extent on one side than the other, this will clearly affect the performance of the pump. Strain localization affects the fatigue performance and failure rate of Nitinol as well. A region in a Nitinol device that is

undergoing more strain (deformation) will fatigue and fail more quickly. Although Nitinol devices are extensively used in the medical industry, there is a fundamental gap in the amount of high-quality quantitative experimental data detailing localization. The numerous applications of shape-memory alloys provide the motivation to understand the deformation and failure mechanisms of these materials, particularly their fatigue and fracture behavior. This is of great importance and concern in the medical industry, where, for example, stent failure by either fatigue or fracture can cost a patient and hospital considerable time, expense, and hazard towards the patient's health.

1.4 Outline

The structure of this thesis is as follows. Chapter 2 will discuss stress-induced martensitic phase transformation in thin sheets of Nitinol. Using Digital Image Correlation (DIC), an *in-situ* optical technique, full-field quantitative strain maps of localization are obtained for the first time in Nitinol. The use of DIC provides new information connecting previous observations on the micro- and macro-scale. It shows that the transformation from austenite to martensite initiates before the formation of localized bands, and that the strain inside the bands does not saturate when they nucleate. The effect of rolling texture on the macroscopic stress-strain behavior is observed, and it is shown that the resolved stress criterion or Clausius-Clapeyron relation does not hold for polycrystalline Nitinol. Finally, the effect of geometric defects on localization behavior is observed.

In Chapter 3, an experimental investigation into the fracture properties of 150 μm thick edge-cracked specimens of austenitic Nitinol under uniaxial tension is presented. Using Digital Image Correlation (DIC), strain fields directly relating to phase boundary nucleation and propagation of fracture samples were observed for the first time. The shape and size of

the saturation and transformation zones as a function of loading near the crack tip were examined. The crack initiation fracture toughness K_{IC} , determined from the maximum load value, was determined to be $51.4 \pm 3.6 \text{ MPa}\sqrt{m}$. The extent and nature of the phase transformation obtained from DIC, combined with the relatively high value of K_{IC} , underscores the importance of crack tip shielding in the fracture of shape memory alloys.

In Chapter 4, the importance of crack tip shielding in the fracture of shape memory alloys, shown in the fracture experiments of Chapter 3, is investigated in depth through finite element methods. A small-scale transformation analysis based on numerical finite element modeling is presented near a crack tip in Nitinol under plane stress conditions. Under far field mode-I loading, the deforming domain containing the crack can be divided into three distinct regions: a fully transformed zone around the crack tip, an annular transition zone, and an untransformed elastic region in the far field. The nature of the stress and strain fields in the various regions, and the relationship between J_{tip} and $J_{applied}$ in light of the transformation process are discussed. Scaling relations are proposed for the radii of the saturation and transition regions as a function of the applied stress intensity factor, K_I . The effect of material parameters on fracture behavior is discussed for various uniaxial behaviors of Nitinol. The structure of the crack tip field and the scaling relations introduced here provide a foundation for understanding the fracture mechanics of thin sheets of Nitinol and other shape-memory alloys.

In Chapter 5, the findings of this doctoral work will be summarized. General conclusions from this work and the directions for future research in this field will be discussed.

2. Stress-Induced Martensitic Phase Transformation in Thin Sheets of Nitinol

2.1 Introduction

Of particular interest in the study of strain localization in Nitinol is its propensity to form localized bands of large strain. Leo et al. [20] and Shaw and Kyriakides [7] studied stress-induced transformation in polycrystalline Nitinol wires, and observed that the transformation proceeded through the nucleation and propagation of regions of large strain. Leo et al. [20] also observed that the nature of the hysteretic stress-strain curves depended heavily on the strain rate applied to the wire, and developed a theoretical model to explain this phenomenon. Unlike many of the models currently in the literature, their model does not make use of a kinetic relation or use parameter fitting. Shaw and Kyriakides [7] performed a series of studies at different temperature and deformation ranges in order to probe the thermomechanical properties of Nitinol wire. The wire was tested in a range of approximately -20 to 100 degrees C, in which the fundamental material response of Nitinol varied widely. They observed, as did Leo et al., that the strain rate has a significant effect on the stress-strain response, as well as on the choice of ambient medium.

Subsequently, Shaw and Kyriakides [8] observed the formation of Lüders-like bands in flat strips of Nitinol during deformation. The Nitinol strips were processed to leave a thin ($\approx 5 \mu\text{m}$) black TiO_2 layer on the material. This brittle TiO_2 oxide layer tends to crack when subjected to significant strain changes, like that experienced during the transformation from austenite to martensite. The surface changes of the brittle TiO_2 oxide coating on Nitinol were photographically recorded to qualitatively establish the deformation history; higher reflectivity, where the TiO_2 layer had cracked, indicated the presence of martensite. In the

resulting photographs, the two phases were separated by a sharp ($A \rightarrow M$) transformation front that could be accurately tracked. Simultaneously, temperature changes in the Nitinol strips were observed using an infrared thermal imaging camera. The photographic and infrared data were synchronized and presented with the corresponding stress histories to give a coherent picture of the evolution of stress-induced phase boundary propagation in superelastic Nitinol. Shaw and Kyriakides concluded that nucleation stress is greater than the stress required to subsequently continue the transformation, and that deformation during transformation is inhomogeneous and takes the form of two or more phases connected by a transition front. They also observed that the transition front was usually nearly straight and at an angle of about 60 degrees to the axis of loading, but it did occasionally form a criss-crossing pattern. Later work by Shaw and Kyriakides [21] on Nitinol strips found that the martensite nucleates in sharp bands inclined at 55 degrees to the axis of loading, and that the martensite propagates by either a steady-state propagation of inclined transition fronts or by a criss-crossing pattern. The experimental results obtained in this chapter are consistent with these conclusions.

Others have also used infrared imaging to track martensitic band formation in superelastic Nitinol. In 2004, Pieczyska et al. [13] performed displacement-controlled tension tests on Nitinol sheet specimens at a strain rate of 10^{-2} s^{-1} , obtaining high-resolution infrared images. The infrared measurements were compared with the stress-displacement test history. Temperature distributions were inhomogeneous during macroscopic transformation and clearly showed the appearance of martensitic bands, visible by the latent heat released during transformation.

In addition to these techniques, changes in surface morphology have been successfully used to track macroscopic localization. In 2006, Feng and Sun [11] reported on

domain morphology evolution observed during the transformation to stress-induced martensite in commercially-available polycrystalline Nitinol micro-tubing under tension. The observation system included an imaging camera, high-speed motion camera, measuring microscope, surface profiler, and infrared camera. By synchronizing the load-deformation and this surface morphology observation technique, they were able to observe and record the nucleation, growth, and eventual vanishing of a single stress-induced deformation domain in the polycrystalline Nitinol tube.

As can be seen by the overview given above, strain localization has been a topic of intense interest with a wide range of experimental investigations [8 - 11, 14, 21 - 24]. The interest in strain localization is both for its inherent scientific interest and also motivated by the use of shape memory alloys in medical devices. Yet surprisingly, there are no full-field quantitative measurements of the strain and its evolution during deformation. In this chapter, we present full-field measurements of the strain during stress-induced martensitic transformation in thin sheets of Nitinol for the first time. These full-field strain mappings are presented with the corresponding stress histories for displacement controlled uniaxial tension tests of a range of specimen geometries.

These measurements are obtained by Digital Image Correlation (DIC), an *in-situ* optical method that measures displacement on the surface of an object by tracking and correlating a random pattern on the sample surface [25]. Our measurements show that the progress of the transformation is much more complex than commonly assumed. The transformation initiates before the nucleation of bands. It is not complete within the bands on nucleation, but proceeds with increasing load. The transformation is not complete even upon apparent saturation. We examine the role of texture by extracting specimens with

different orientations with respect to the rolling direction. We also examine the role of geometric defects on localization.

2.2 Material and Experimental Details

Dogbone shaped tensile specimens as shown in Figure 2.1 were extracted by wire-EDM (Electrical Discharge Machining) from rolled sheets with a nominal thickness of $160\ \mu\text{m}$ and a composition of 48 wt.% Titanium and 52 wt.% Nickel. The sheets were flat annealed with an A_f temperature of 11.3 degrees Celsius. The low A_f temperature ensured that the specimens were fully austenitic when unloaded and that the stress-induced martensite occurred upon loading.

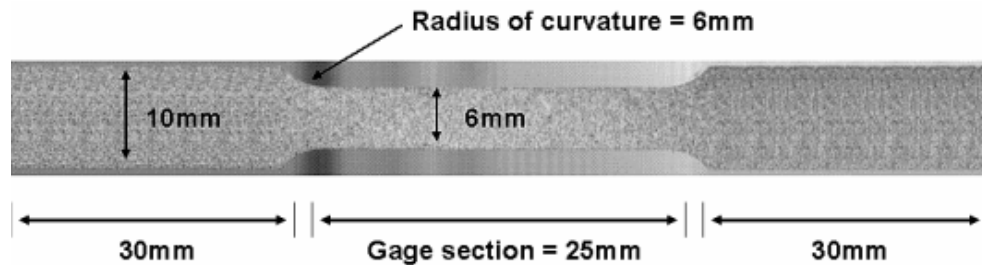


Figure 2.1: The specifications of dog-bone test specimens.

Tensile specimens with varying orientation with respect to the rolling direction (RD) were extracted from the same sheet. To understand the texture of the rolled sheet, optical micrographs of the tensile specimens were obtained by heavily etching them in $1\text{HF} + 4\text{HNO}_3 + 5\text{H}_2\text{O}$ for 30 - 45 seconds. This recipe was adapted from work performed by Shabalovskaya et al. [26]. The results are shown in Figure 2.2 for three specimens numbered 1 - 3; oriented along the RD, perpendicular to RD, and 45 degrees to RD, respectively. The micrographs show elongated etch pits in the rolling direction underscoring the texture.

Further, the three micrographs are very similar except for orientation, demonstrating the homogeneity of the rolled sheet. Finally these, and more lightly etched specimens, demonstrate that the grain size in this rolled sheet is of the order of 100 nm.

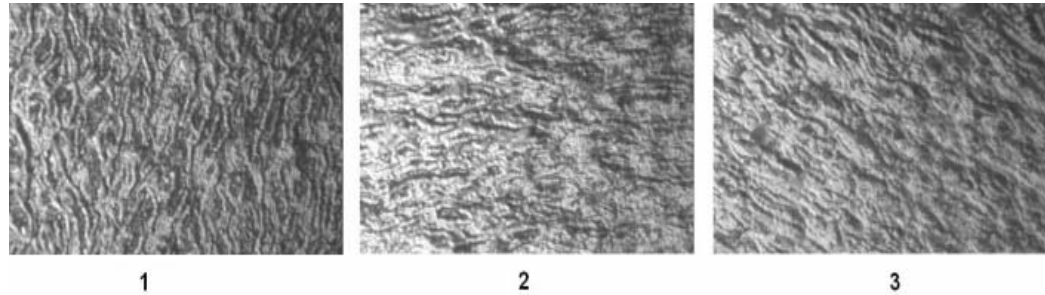


Figure 2.2: Optical micrograph of NiTi sheet at 60x at 3 different orientations; parallel to RD (1), perpendicular to RD (2), and 45 degrees to RD (3)

The texture of the specimens was also probed using X-Ray Diffraction (XRD) techniques, as seen in Figure 2.3 and Figure 2.4. Figure 2.3 shows the XRD data of the Nitinol thin sheets used in these experiments, and the corresponding reference pattern indicating crystallographic orientations of possible intensity peaks. The sheets showed the presence of $\langle 211 \rangle$ but were dominated by $\langle 110 \rangle$ in XRD. This texture was further examined in the pole plots shown in Figure 2.4. In each pole plot, a specific crystallographic orientation was picked based on the results from Figure 2.3. The distribution of this picked crystallographic orientation, with respect to in-plane rotation (ϕ) and out-of-plane rotation (ψ), was examined by measuring the intensity of the x-ray reflection from the relevant lattice planes, and the measured intensity (z), in-plane angle (θ), and out-of-plane angle (radius) were plotted in three-dimensional polar coordinates. The $\langle 110 \rangle$ pole plot is clearly anti-symmetric, with a strong ϕ (in-plane) and ψ (out-of-plane) preference, whereas the $\langle 211 \rangle$ pole plot is symmetric, with no clearly defined preference. The pseudo-Gaussian

drop off in the intensity with respect to psi is expected, due to the fact that when the sample's rotation out-of-plane increases, the reflected intensity of the x-rays decreases.

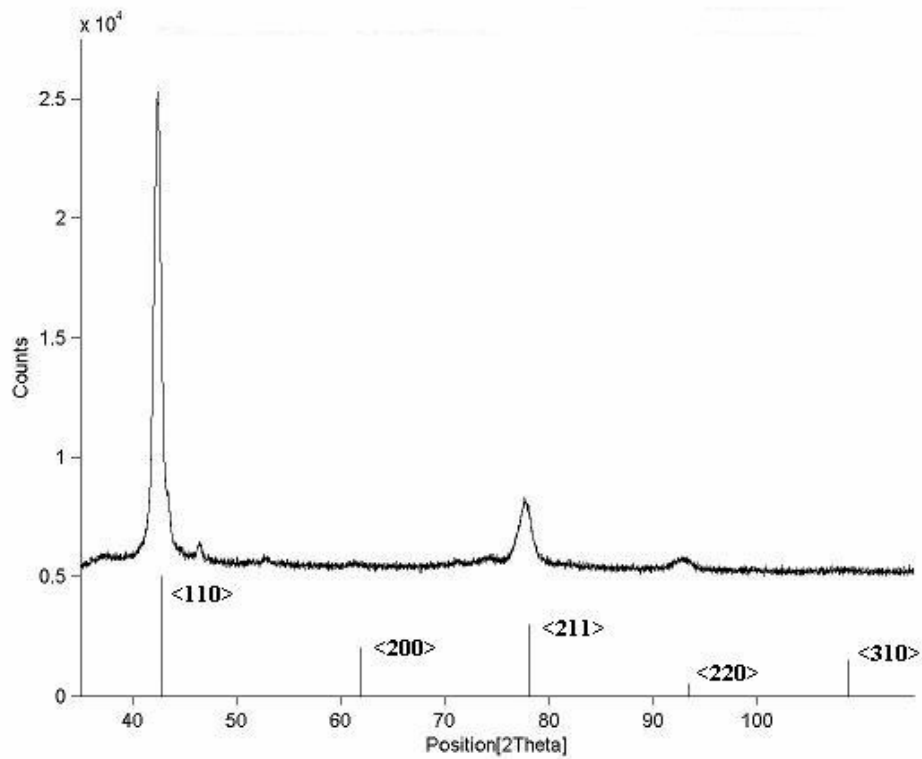


Figure 2.3: X-ray diffraction data of Nitinol thin sheets and corresponding reference pattern for Nitinol

The samples used for XRD in both Figures 2.3 and 2.4 were cut from the same sheet as those used in the following experiments. They were smooth sheet, $\sim 150 \mu\text{m}$ thick, samples that were cut into circular shapes in order to minimize the effect of changing area on the intensity measurement as the sample was tilted to look at out-of-plane dependence of crystallographic orientation. Figure 2.4 illustrates the highly complicated texture of these rolled sheets.

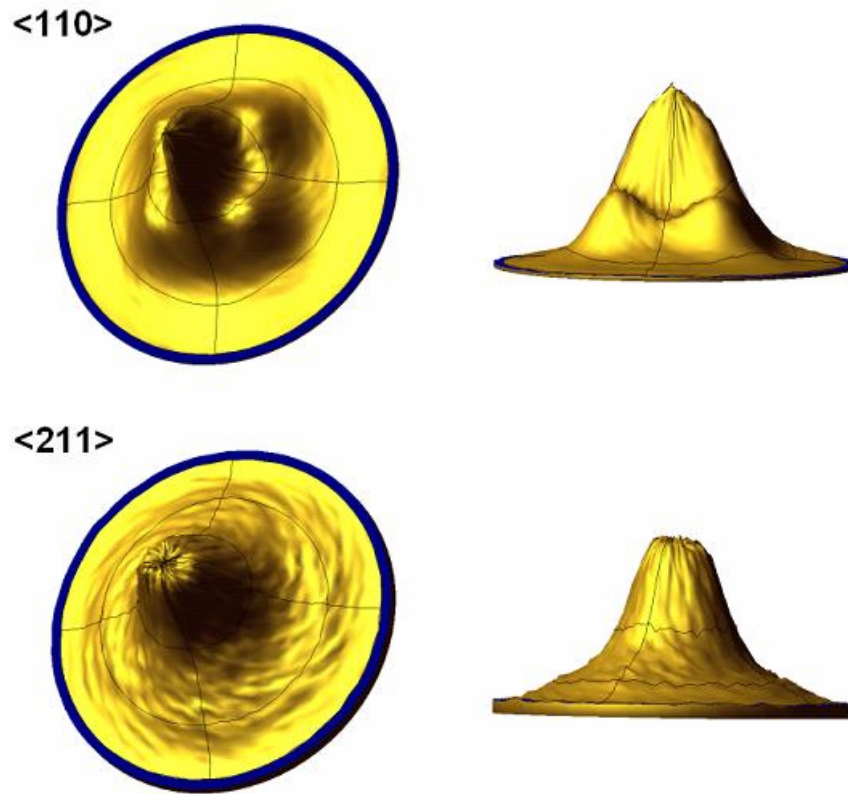


Figure 2.4: Pole plots of crystallographic orientations $\langle 110 \rangle$ and $\langle 211 \rangle$, observed to have high intensity in the x-ray diffraction data of Figure 2.3

The specimens were tested in uniaxial tension under displacement control using a computer-controlled servo-hydraulic machine (MTS Model no. 358.10), as shown in Figure 2.5. Figure 2.5 shows a schematic of the experimental setup (top) as well as a photograph of the setup (bottom). Knurled tension grips were used to minimize slippage and were carefully aligned to minimize out-of-plane loading and displacement. Grip slippage was also minimized by attaching emery paper to the grip sections of the sample in order to maximize friction in the connection between the grips and the sample. Specimens were tested with a fixed bottom grip and moving upper grip, both of which were supported by pivots to minimize bending and shear in the specimens. The applied strain rate was 10^{-3} s^{-1} . This is somewhat higher than the 10^{-4} s^{-1} recommended by various researchers for isothermal tests,

but was found to be adequate for our thin sheets and enabled the variety of observations that we conducted.

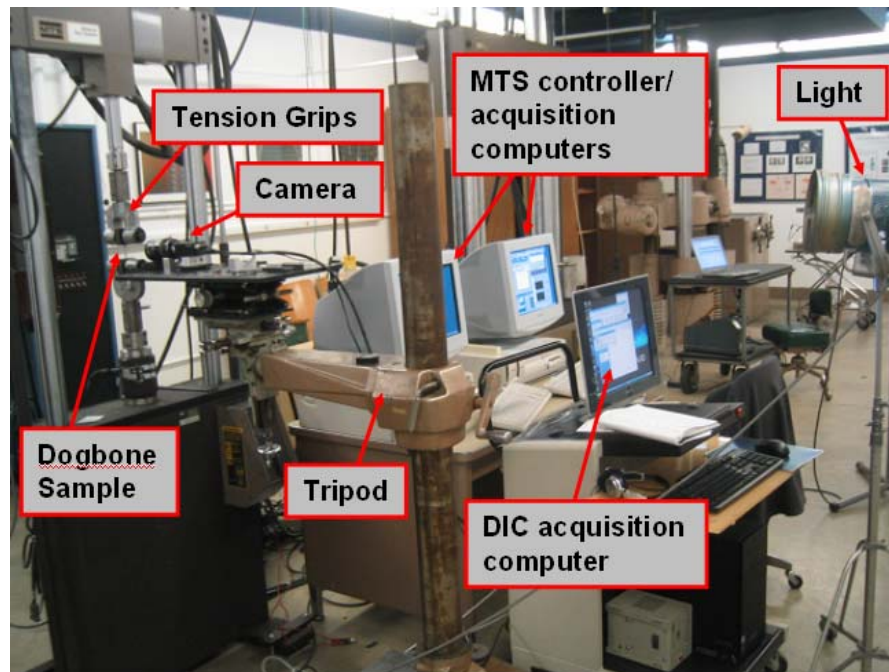
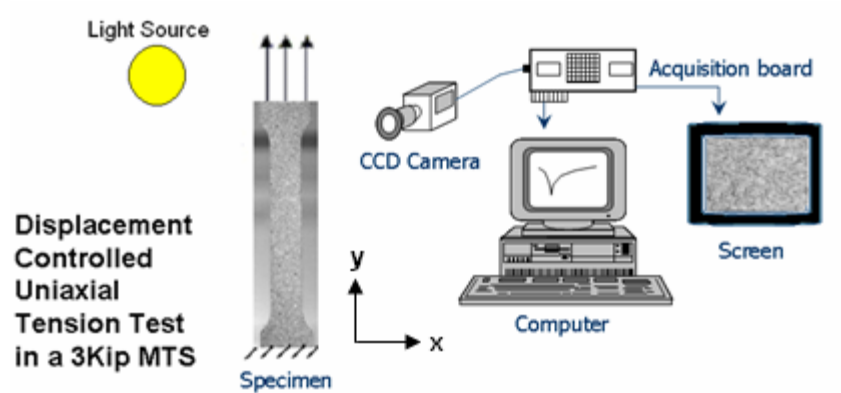


Figure 2.5: A schematic (top) and photograph (bottom) of the experimental setup. The schemia is adapted from a picture by D. Garcia, Ecole Mines des Albi, France.

The strain in the specimen was measured using Digital Image Correlation (DIC).

This is an *in-situ* optical correlation method used to measure displacement on the surface of

an object by tracking a random pattern on the sample surface. The random pattern could be inherent surface features or an artificially applied pattern, but must provide a sizeable number of correlation points at the magnification of imaging. In this experiment, the pattern was applied pre-test by first coating the sample in white paint and then spraying a light mist of black paint in a fine speckle pattern. Images were recorded using 1200x1600 pixel CCD camera focused on the specimen surface and linked to a computer for data acquisition. Between one to three photographic lenses were used to focus the image depending on the area of interest; a 50 mm Nikon was used as the main lens, and two Sigma x2 and Sigma x1.4 lenses were also utilized for zooming purposes. Since the deformation was in-plane, a single CCD camera could be used to capture the deformation. Images were taken after each displacement increment and post-processing was achieved with the software Vic-2D developed by Correlated Solutions [27] to extract the strain fields.

There are certain sources of error in these experiments that need to be briefly discussed. There is grip slippage, although testing for stability of MTS applied force pre-test helped to minimize this error. There is grip alignment error, which was minimized by carefully aligning the grips and checking alignment with each experiment, and the self-aligning nature of the grip. There are also analysis errors due to any out-of-plane deformation of the specimen. There are numerous parameters in the Vic-2D Correlated Solutions program that can be adjusted, and these parameters have a significant effect on the success of the computation. Improper lighting, dust, marks on the camera lens, inadequate camera shutter speed, or inadequate aperture can produce a faulty or blurred speckle pattern and cause failure. With our specifications and settings, we estimate the strain accuracy to be approximately 0.1%.

2.3 Experimental Observations

2.3.1 Uniaxial Tension Parallel to the Rolling Direction

Figure 2.6 presents a detailed progression of the mesoscopic and macroscopic stress-strain behavior of a dog-bone specimen cut parallel to the rolling direction (RD) and subjected to uniaxial tension under displacement control. Snap-shots of the specimen were taken after each displacement increment, and the strain distributions were computed. The overall strain of the specimen in the longitudinal direction is obtained from the average of the strain over the entire specimen. The spatially averaged strain of the specimen in the longitudinal direction obtained from DIC was verified by extensometer and strain gages. This overall axial strain is plotted against the nominal stress applied by the MTS machine in Figure 2.6. The 2-pixel spatial resolution is approximately 0.05 mm. The pictures that accompany the macroscopic stress-strain curve show the evolution of normal component of strain in the longitudinal direction, ϵ_{yy} . The pictures are numbered 1-10 for comparison with the ϵ_{xx} and ϵ_{xy} strain components at the corresponding locations in Figure 2.7. The unloading curve was recalibrated and adjusted downwards to compensate for the offset in the MTS loading frame.

The specimen is fully austenitic at the beginning of the test, and behaves in a linear elastic manner with an approximate modulus of 45 GPa. It begins to deviate from linearity with an apparent drop of modulus around a stress of 460 MPa and strain of 1%. The accompanying image shows that the strain is almost but not completely uniform throughout the specimen. As the loading continues, the level of strain continues to increase throughout the specimen, until we begin to see the appearance of a localized band of high strain close to the bottom grip at around 1.5% strain. Further deformation occurs by the broadening of and nucleation of new bands with little apparent increase of stress. The bands are all parallel

in this specimen and oriented at approximately 55 degrees from the loading axis. The bands gradually coalesce and the stress begins to increase around a macroscopic strain of 4.25%. A short transition follows and the behavior becomes linear beyond that, with a modulus of approximately 15 GPa.

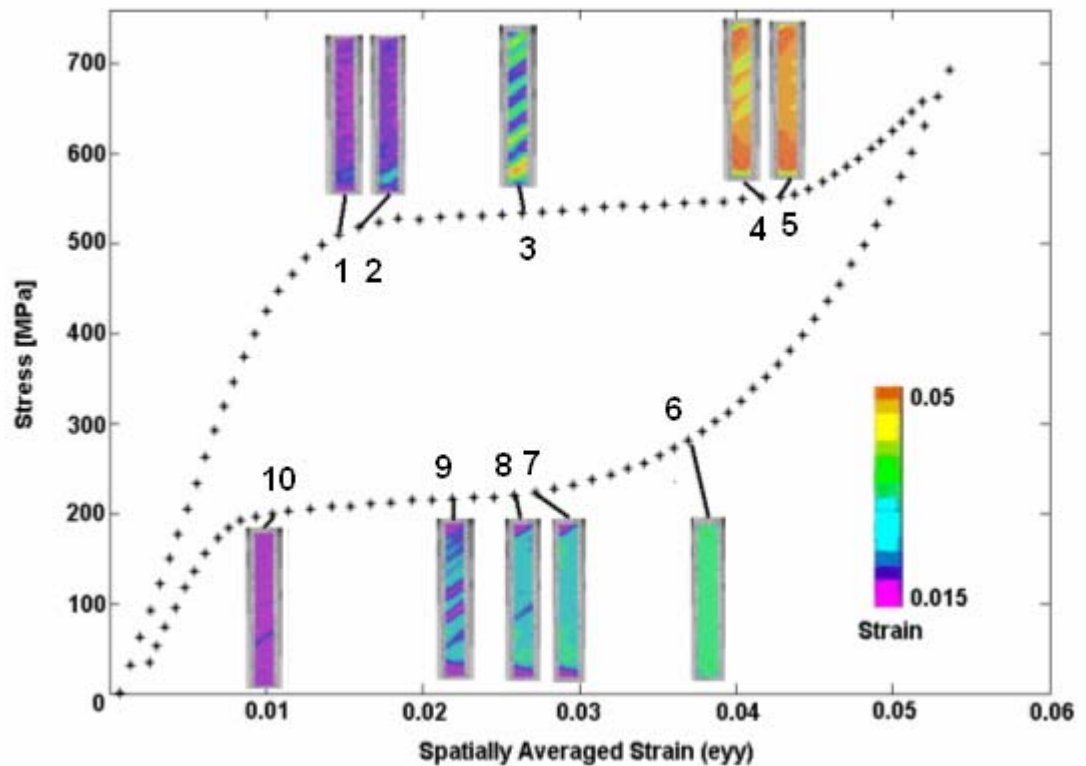


Figure 2.6: The macroscopic response of a dog-bone specimen cut parallel to the RD with corresponding DIC images for ϵ_{yy} . The macroscopic response is the spatially averaged strain value from each DIC image plotted against the MTS stress value.

The unloading follows a similar pattern. It begins with an almost linear unloading with a modulus of approximately 30 GPa. There is a departure from linearity at about 4% strain, and the first localized band with small strain appears around 2.8% strain. There follows subsequent decrease in strain preceded by the growth of and nucleation of new bands with little apparent decrease of stress. The bands eventually coalesce and this is followed by linear unloading. There is a small amount of residual strain, as is expected for

any virgin specimen. For future use, we label the stress at which we see deviation from linearity on loading as the transformation onset stress (σ_T), and the residual strain that would be obtained if the unloading were purely linear as the transformation strain (ϵ_T).

Figure 2.7 shows the ϵ_{xx} , ϵ_{yy} , and ϵ_{xy} strain components at points 1-10 labeled in Figure 2.6. In Figure 2.8, the macroscopic stress-strain curve for the rotation of the sample, ϵ_{xy} , is shown. As in Figure 2.6, this curve is the spatially averaged strain value from each DIC image plotted against the MTS stress value when the image was taken. Because the spatially averaged values of ϵ_{xy} are on the order of the 0.01% - 0.1% strain, i.e. the resolution of the DIC technique, this graph shows significant scatter. However, it still displays the hysteric curve characteristic of Nitinol, illustrating the robustness of this technique.

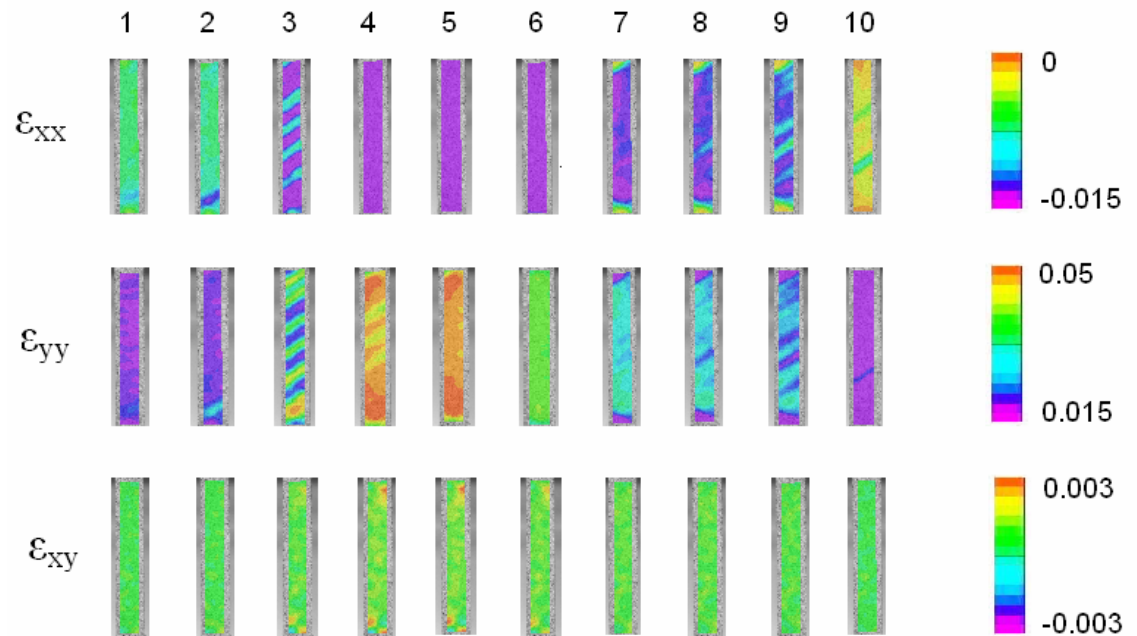


Figure 2.7: The corresponding DIC images for the ϵ_{xx} , ϵ_{yy} , and ϵ_{xy} strain components for the points 1-10 labeled in Figure 2.6, which shows the macroscopic response of a dog-bone specimen cut parallel to the RD.

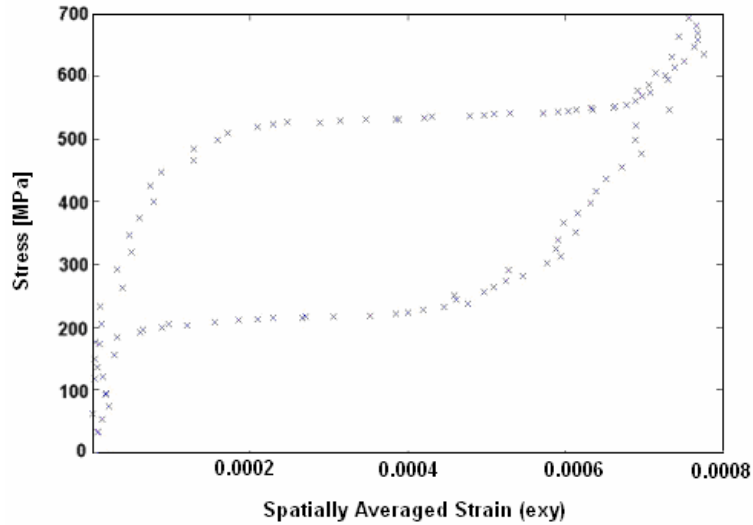


Figure 2.8: The macroscopic response of a dog-bone specimen cut parallel to the RD with corresponding DIC images for ϵ_{xy} . The macroscopic response is the spatially averaged strain value from each DIC image plotted against the MTS stress value.

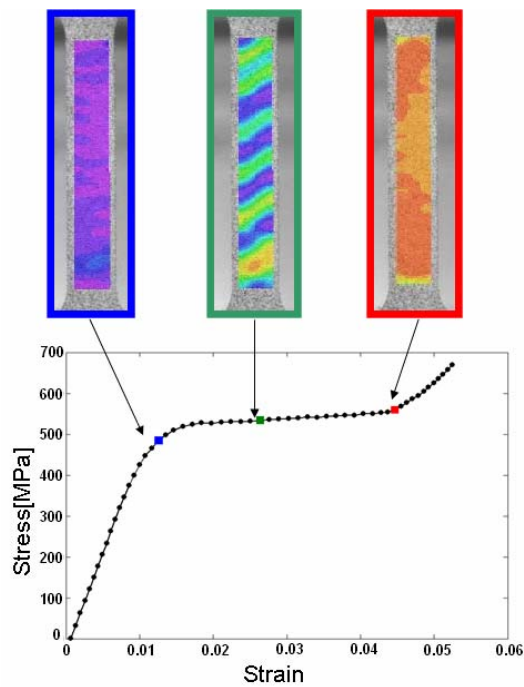


Figure 2.9: The loading curve from Figure 2.3, examining three specific points during the loading phase: prior to the appearance of any macroscopic localization (blue), halfway through the transformation when all the bands have nucleated and are nominally halfway through growing (green), and immediately after the coalescence of the bands with no remaining localization (red).

Figure 2.9 shows the same loading curve as Figure 2.6, with the examination of three specific points during the loading phase: prior to the appearance of any macroscopic localization (blue), halfway through the transformation when all the bands have nucleated and are nominally halfway through growing (green), and immediately after the coalescence of the bands with no remaining localization (red). The DIC image corresponding to each of these three points is shown. In Figure 2.10, the longitudinal strain (ϵ_{22}) down the centerline of the sample is shown for the three points during the loading phase detailed in Figure 2.9. Note that the strain levels are quite high -- above 1.2% -- before there is any macroscopic localization. Further note that the strain is not perfectly uniform but suffers from small fluctuations. Once localization begins, the value of the strain inside the band does not jump directly to the maximum (saturation) level. Instead, it gradually increases even as the bands grow. Finally, once the bands coalesce at the end of localization, the strain is almost, but not perfectly, uniform throughout the specimen.

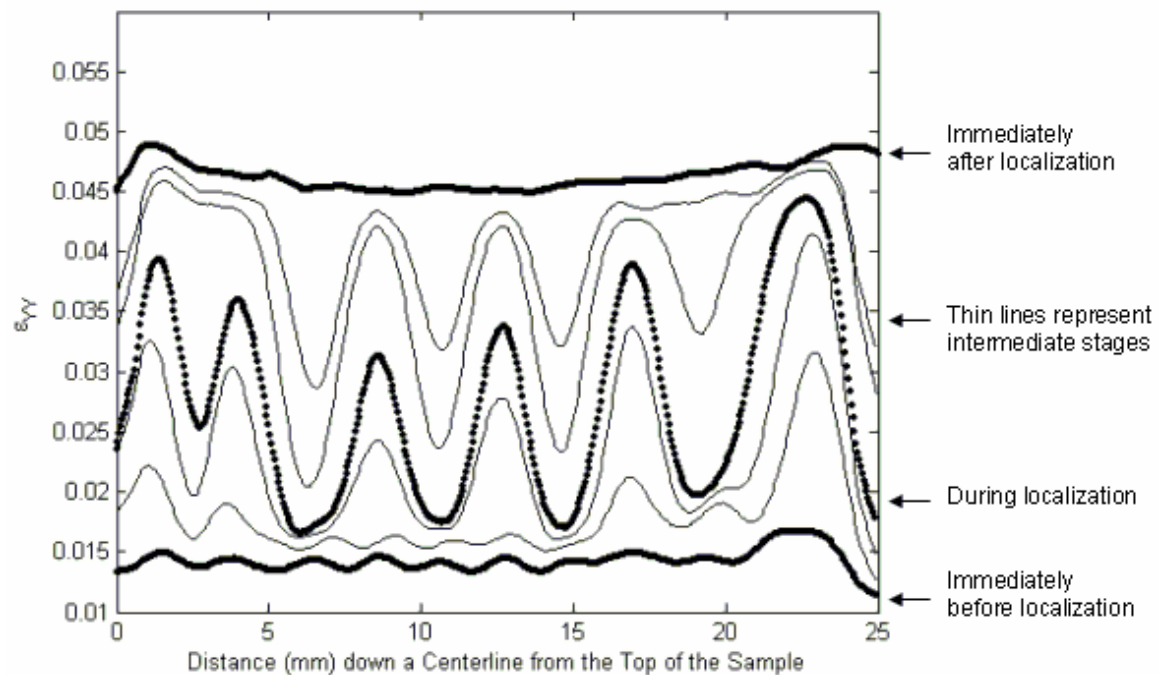


Figure 2.10: Strain down the centerline of a dog-bone specimen cut parallel to the RD during various localization stages

2.3.2 Uniaxial Tension in Various Orientations

Figures 2.11 and 2.12 detail the macroscopic stress-strain behavior under uniaxial tension of dog-bone specimens cut out of the same sheet, but at various orientations relative to the rolling direction. As before, a photograph of the specimen is taken after each displacement increment, and this image is used to calculate the strain field. The macroscopic strain is obtained by averaging.

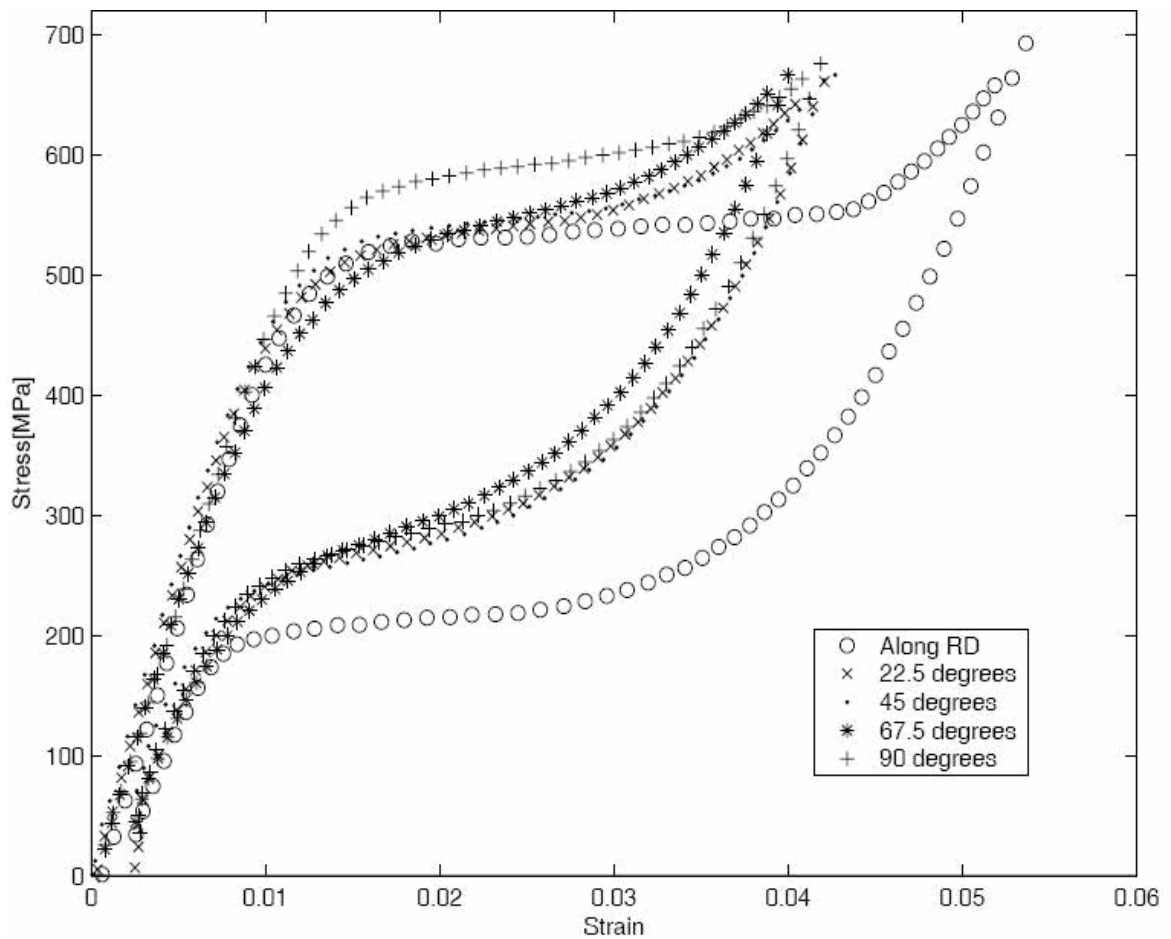


Figure 2.11: The uniaxial stress-strain response of various specimens with different orientations to the rolling direction

The qualitative behavior is very similar to that described above. It begins linearly, with a deviation and associated small oscillations in strain from linearity at 1% strain; the appearance of localized bands of strain at approximately 1.5% strain, accompanied by a plateau in the stress-strain curve; growth of the bands and growth of the strain in the bands until coalescence, followed by a rising stress-strain curve; and a similar pattern on unloading. However, the transformation onset stress and transformation strain depend on orientation. The transformation strain decreases as we move away from the rolling direction, reaching a minimum at 67.5 degrees and then recovering a little. The transformation onset stress is approximately the same for all orientations, except for specimens cut at 90 degrees from the rolling direction. The observed localization patterns and the evolution of strain are similar.

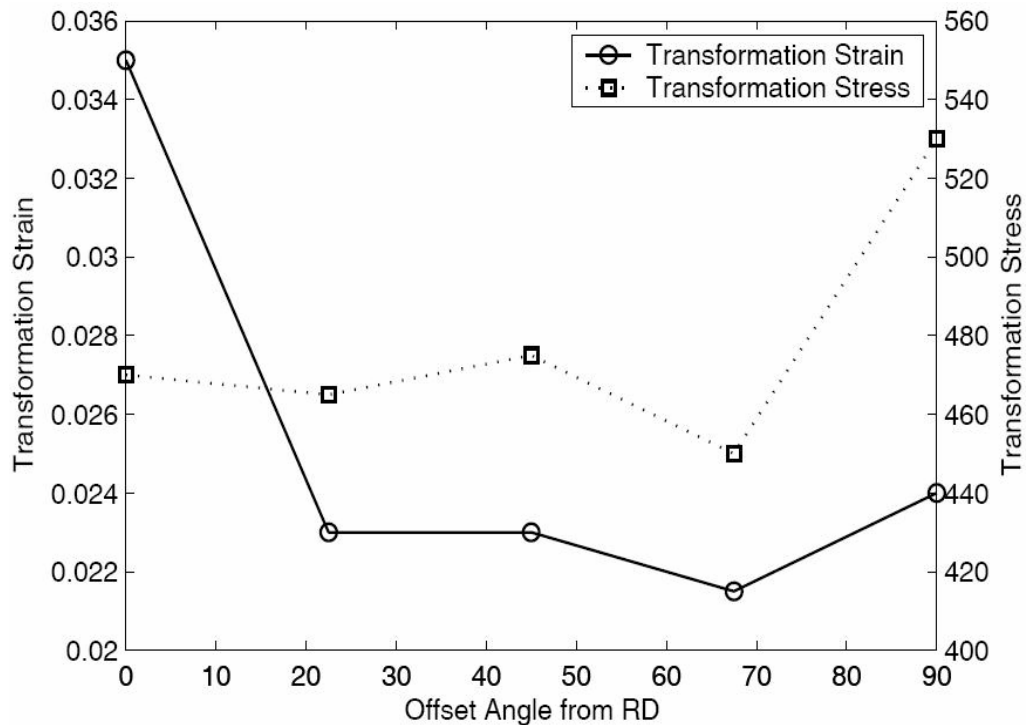


Figure 2.12: The variation of transformation initiation stress and transformation strain with orientation

2.3.3. Repeatability

The same test was repeated in the same specimen multiple times, including taking the specimen off of the loading frame and then remounting. The results, specifically the stress-strain curve and localization patterns, were repeatable, except for the small residual strain in the first few cycles.

The same test was repeated in specimens cut from various sheets obtained from the same manufacturer. The characteristics of the macroscopic stress strain curves were very similar, with a variation in transformation onset stress and transformation strains less than 25% from sheet to sheet. However, the localization in some specimens showed a crossing pattern as shown in Figure 2.13, with both sets of bands oriented at approximately 55 degrees to the loading axis. This phenomenon was also reported in work by Shaw and Kyriakides [21].

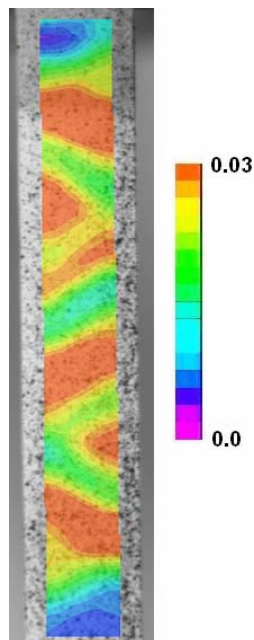


Figure 2.13: An example of the crossing bands found in some specimens

2.3.4 Strain Fields Around Surface Features

To understand the origin of the strain localization and the sensitivity to defects, the tests above were also repeated in specimens with holes and side notches.

2.3.4.1 Surface Feature: Hole

Dogbone specimens oriented along the rolling axis were prepared with a 1 mm hole centered bi-axially in the gage region. Observations of strain were at low magnification with the entire specimen in the field of view, and repeated at high magnification close to the hole. Figure 2.14 shows the results of these tests in separate specimens for the low and high magnification so that both sets show the results for a virgin specimen. The macroscopic stress-strain behavior is the similar to that observed earlier. As expected, we see larger strains in the immediate vicinity of the hole, and two bands of localized strain in a crossing pattern nucleate from there. Once again, the strains in these bands are less than the fully saturated values when these bands first form, and gradually increase with increasing loading. The bands also increase in size. As the loading continues to increase, other bands oriented approximately 55 degrees to the loading axis form in the regular portions of the gage section.

The high-resolution images provide further insight into the development of the strains. It is important, however, to note that DIC is unable to resolve the strains in a small annulus around the hole. So it is possible and likely that there is increased strain at some points in this annulus. Two small regions of increased strain adjacent to the hole become visible and develop into kidney-shaped lobes in Figure 2.14-a. These lobes are reminiscent of plastic zones in an elastic-plastic body. As the loading is further increased, the lobes close to the hole grow and develop into crossing bands (Figure 2.14-b). Finally, we did not observe any significant residual stress in the vicinity of the hole on unloading.

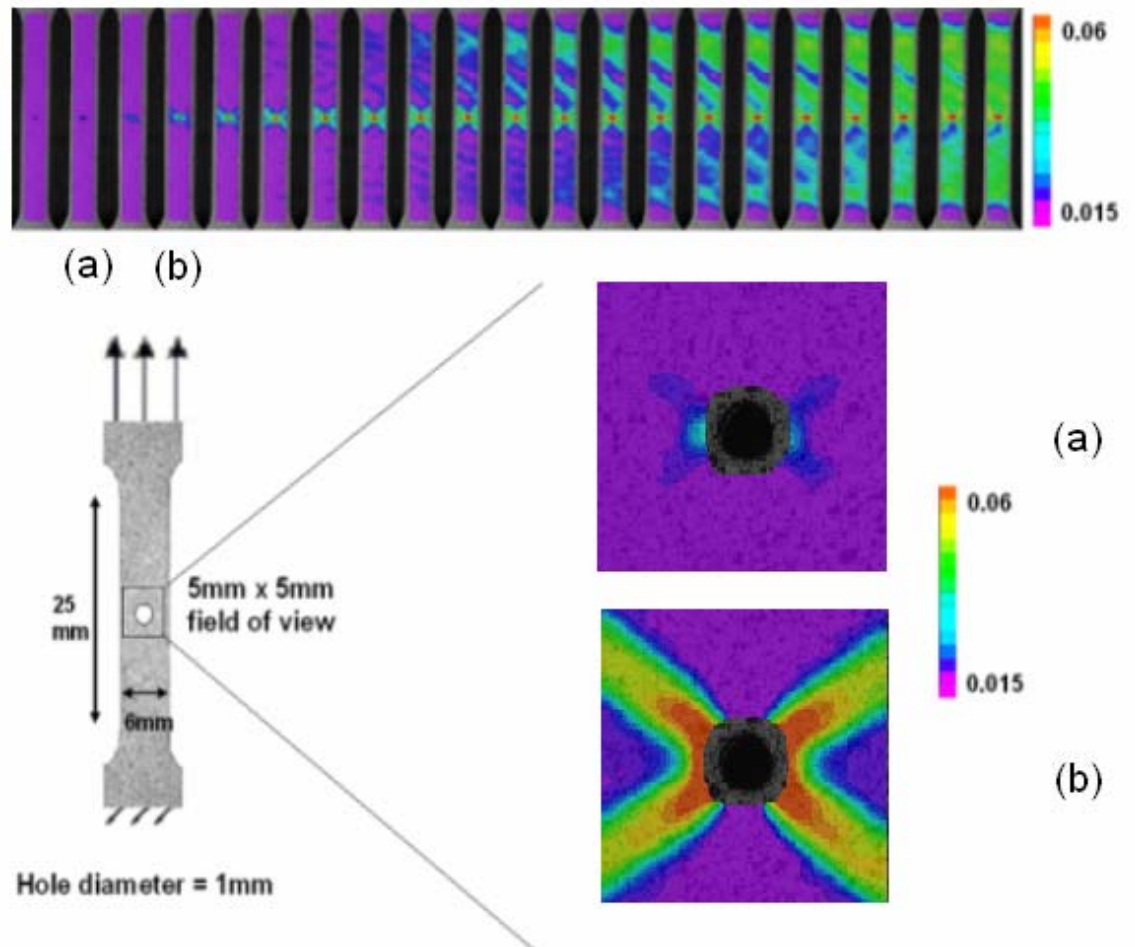


Figure 2.14: Strain localization in a non-homogenous stress field: Hole. Panels (a) and (b) show the development of kidney-shape lobes, which grow and develop into crossing bands as strain continues to increase. The pictures are shown at different resolutions in order to capture the development of the strain. The top picture shows a snapshot full-field progression of band localization.

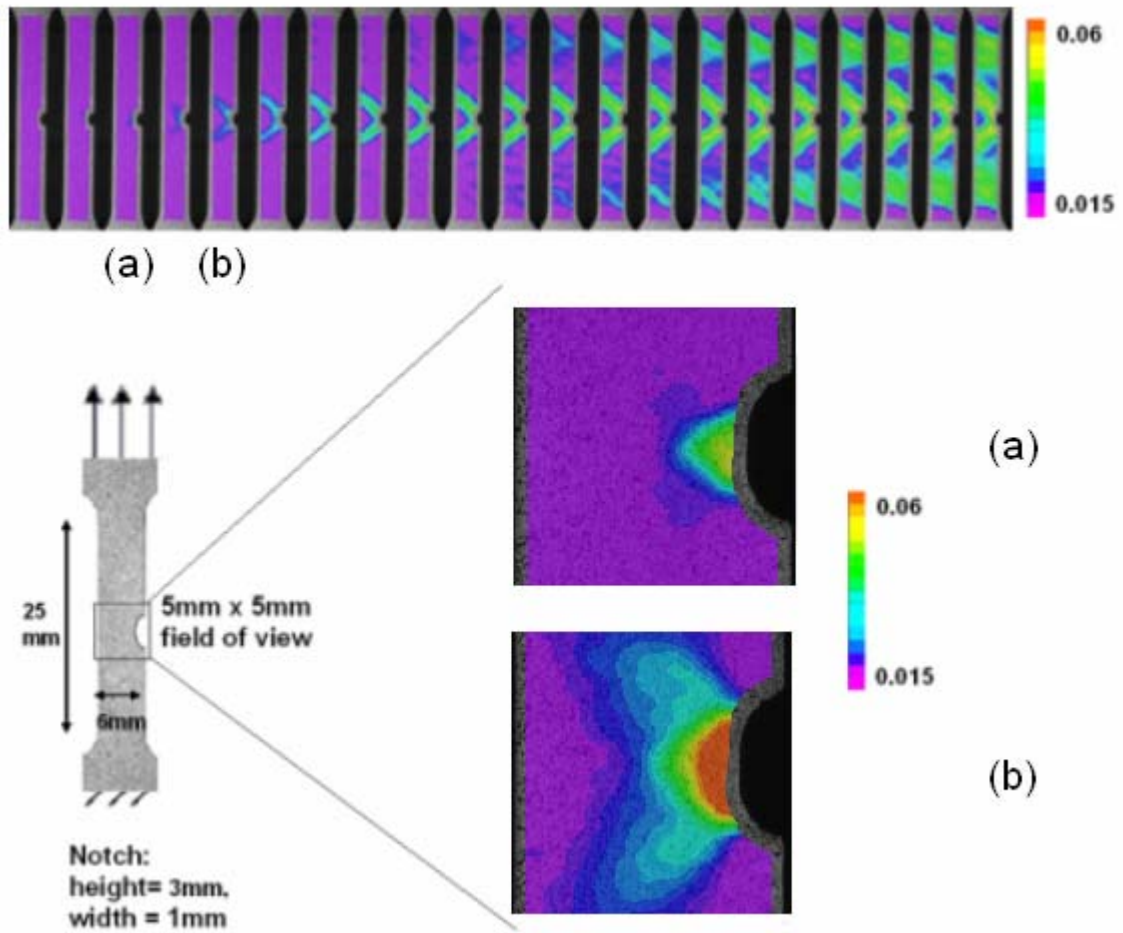


Figure 2.15: Strain localization in a non-homogenous stress field: Notch. Panels (a)-(b) show the development of lobes around the notch, which grow and develop into two symmetrically oriented bands as the strain increases. The pictures are shown at different resolutions in order to capture the development of the strain. The top picture shows a snapshot full-field progression of band localization.

2.3.4.2 Surface Feature: Notch

Dogbone specimens oriented along the rolling axis were prepared with an elliptical notch along one edge but centered along the gage length. The notch is 3 mm high and 1 mm wide. Low and high magnification observations were made as before, and the results are reported on two specimens so that both low and high resolution observations in Figure 2.15 correspond to virgin specimens. The macroscopic stress-strain behavior is the similar to those observed earlier. As expected, we see larger strains in the immediate vicinity of the notch, and two symmetrically oriented bands of localized strain nucleate from there. Once again, the strains in these bands are less than the fully saturated values when these bands first form, and they gradually increase with increasing loading. The bands also increase in size. As the loading continues to increase, other bands oriented approximately 55 degrees to the loading axis form in the regular portions of the gage section. The high resolution images show a kidney-shaped region of increased strain develops and begins to grow (Figure 2.15- a, b) eventually developing into the macroscopic bands. Finally, we did not observe any significant residual stress in the vicinity of the notch on unloading.

2.4 Discussion

The experimental observations presented in the previous section provide various insights into the mechanism of deformation and stress-induced transformation in rolled sheets of Nickel-Titanium (Nitinol).

The specimens tested were in the austenite state at room temperature, and initially responded linearly on loading. The departure from linearity began around 1% macroscopic strain, as shown in Figures 2.6 and 2.11. We interpret this as the beginning of the phase

transformation in the specimen from the austenitic to the martensitic state. However, this departure from linearity was *not* accompanied by the formation of any localized band of deformation, but displayed almost uniform strain (Figure 2.6). This leads us to conclude that the transformation begins homogeneously on a macroscopic scale throughout the specimen without any localization. Niemczura and Ravi-Chandar [23] have reached the same conclusion based on dynamic loading of shape-memory strips.

At the same time, Figure 2.6 clearly shows that the strain is not perfectly uniform throughout the specimen but shows some spatial variation. This leads us to conclude that the transformation is microscopically heterogeneous. These conclusions are also supported by the recent experimental observations of Brinson et al. [10]. They performed tensile tests of small specimens extracted from sheets while observing the specimen *in-situ* with an optical microscope. They observed that the transformation initiates in small regions inside isolated grains. They are also supported by the observations of Barney et al. [24] who examined a tensile specimen extracted from a flattened tube using micro-diffraction through synchrotron radiation. Their technique allows a grain by grain map of the strain, and the results show that the transformation begins in isolated grains.

The small oscillations in the strain field eventually lead to the formation of localized bands of large strain. These bands are oriented approximately 55 degrees to the loading axis. Note that the austenite to martensite transformation is effectively volume-preserving, and can be considered close to isotropic, i.e. it is bounded anisotropic. In comparison to the observed band orientation of 55 degrees, the classical Hill calculation gives 54.7 degrees. Importantly, the strain in the bands is not equal to the saturation value of the transformation strain and we conclude that the transformation does not proceed to saturation inside the bands. Instead the transformation is only partially complete when the bands form and

continues with further loading. These observations are consistent with those of Schmahl et al. [14] who also studied rolled sheets using synchrotron radiation. They found that regions inside the deformation band contained significant portions of strained austenite.

Furthermore, reorientation of the martensitic variants can also contribute to increasing strain.

As the bands coalesce and the stress begins to rise following the plateau, the transformation begins to saturate. However, we notice that the martensitic modulus on loading is noticeably smaller than the martensitic modulus on unloading in this region. This suggests that the transformation is not complete in this apparently saturated region and one still has residual pockets of austenite which continue to transform with increasing loading. The small modulus on loading is a reflection of this. This is consistent with the microscopic observations of Brinson et al. [10] and Schmahl et al. [14].

Our results also show that geometric defects like grips, notches and holes that cause stress enhancement promote localization. However, localization can also occur in uniform regions of the gage section. This leads us to conclude that localization in shape-memory alloys is not a purely geometric instability, but a competition between material and geometric instabilities.

Putting all of these together leads to the following scenario: As we begin to load the austenite, the transformation begins inside isolated grains that are oriented preferentially with respect to the applied stress. These grains are distributed homogeneously on a larger scale, and therefore the transformation initiates homogeneously on the macroscopic scale (much larger than grain size) but heterogeneously on the microscopic scale (comparable to the grain size). This gives rise to an inhomogeneous stress state on the microscopic scale. A combination of these and geometric stress raisers initiate localization. This is resisted by two

factors. The first is intergranular constraint. The second is the latent heat that is released, which raises the temperature and the stress required for further transformation and impedes progress of the transformation. Thus, the transformation is not complete even in the bands but requires increasing stress to sustain. Further, the heating can arrest the development of the bands [7, 20], which provides opportunity for other bands to nucleate and grow. Finally, as the bands coalesce, the transformation is arrested by intergranular constraints and can only proceed by increasing the applied load.

In short, the transformation initiates in well-oriented grains and is saturated by the constraints imposed by the poorly oriented grains. The former is consistent with the observation that the Sachs model, which assumes that each grain deforms independently in response to the uniform applied stress with no regard to the constraint imposed by its neighbors, is a good predictor of the stress at initiation [28]. The latter is consistent with the observation that the Taylor model, which assumes that intergranular constraints are so strong that the mesoscale deformation is uniform, is a good predictor of the transformation strain [29, 30]. A synthesis of these two ideas is inherent in the heuristic network model of Novak and Sittner [27] and the mathematical analysis of Schlömerkemper and Bhattacharya [32].

The fact that the initiation and saturation are controlled by two different aspects has important consequences. Schlömerkemper [31] has pointed out that the Sachs and Taylor models give rise to transformation surfaces that differ dramatically in their eccentricity. This means that the transformation can initiate in one strain direction but saturate in another. This change of strain direction with increasing stress may provide a material mechanism for localization. This implies that texture and crystallography are important factors in

determining the propensity of a material to localize. A similar point has been argued by Sittner et al. [22].

Further, this means that one can not use the resolved stress criterion or Clausius-Clapeyron relation to predict the onset of transformation. Such a criterion is widely used to predict the onset of various deformation modes, and has been shown to be reasonably accurate for stress-induced transformation of single crystals by Miyazaki [5], Shield [6], and others. In this criterion, it is assumed that the transformation begins when the component of applied stress in the direction of transformation strain reaches a critical value that depends on temperature and latent heat:

$$\sigma \cdot \varepsilon_T = L(T - T_C) \quad (2.1)$$

where σ is the macroscopic initiation stress, ε_T is the transformation strain, L is the latent heat, T the temperature, and T_C the transformation temperature.

In our case of uniaxial tension and constant temperature, Equation 2.1 becomes simply,

$$\sigma_T \varepsilon_T = C \quad (2.2)$$

where σ_T is the uniaxial transformation initiation stress, ε_T is the uniaxial transformation strain, and C is a constant independent of the orientation. We can easily verify from the data presented in Figure 2.12 that this equation does not hold. To elaborate, it follows from Equation 2.2 that

$$\frac{\sigma_T(\theta = 0^\circ)}{\sigma_T(\theta = 90^\circ)} = \frac{\varepsilon_T(\theta = 0^\circ)}{\varepsilon_T(\theta = 90^\circ)}$$

The experimental data in Figure 2.11 and 2.12, however, shows that

$$\frac{\sigma_T(\theta = 0^\circ)}{\sigma_T(\theta = 90^\circ)} \approx 0.89 \neq \frac{\varepsilon_T(\theta = 0^\circ)}{\varepsilon_T(\theta = 90^\circ)} \approx 1.46$$

in contradiction of the resolved stress criterion or Clausius-Clapeyron relation.

We finally comment on the finger-shaped localization observed at low values of applied macroscopic strain in the notched specimen. Since the notch is cut asymmetrically, the gage section in the vicinity of the notch is subjected to bending deformation. In other words, the side with the notch has higher compliance and elongates more than the side without the notch. Thus the extensional strain has to decrease as one passes from the side with the notch to the other, and the material accomplishes this using the strain fingers. In this regard, these are the polycrystalline analogs of the tapered twins that have been observed in single crystals subjected to bending [32]. Further, they also show the propensity of the material to have localized deformation at this mesoscale.

3. An Experimental Investigation of Crack Initiation in Thin Sheets of Nitinol

3.1 Introduction

Almost immediately following its development, there was significant research on the fatigue behavior of Nitinol, stemming mainly from its suitability for medical applications (for examples see [2, 33 - 38]). Interest in improving the design and performance of medical stents for implantation in the human body motivates many of these studies, for example the experiments of McKelvey and Ritchie [33, 34] on fatigue-crack propagation in Nitinol. They found that in general, “fatigue-crack growth resistance ... increase[d] with decreasing temperature, such that fatigue thresholds were higher and crack-growth rates slower in martensite compared to stable austenite and superelastic austenite” [33]. They also found that stress-induced transformation of the superelastic austenite could be suppressed in plane strain conditions, but that this effect was not seen in thinner specimens. Robertson and Ritchie [37] recently conducted an experiment to investigate fatigue-crack growth and fracture toughness behavior of a thin-walled ($\approx 400 \mu\text{m}$ thick) superelastic Nitinol tube. Their tests found significantly a higher fatigue threshold and a lower measured toughness than previously reported values for bulk Nitinol material.

Although the fatigue behavior of Nitinol has been a topic of strong interest, fracture, an equally important issue, has received scant attention. There have been recent developments in the modeling of fracture in shape memory alloys, but there has been little experimental work. Ni-Mn-Ga, a ferromagnetic shape memory alloy which is prone to fracture under thermal cycling, contrary to most SMAs, is one exception. Xiong et al. [16] studied the thermally induced fracture of single crystal Ni-Mn-Ga using *in-situ* optical

microscopy coupled with Scanning Electron Microscope (SEM) observation. They found that the coexistence of several martensitic variants lead to the formation of a crack network in the Ni-Mn-Ga crystal, and ultimately to fracture. They also found that the fracture surface related to a specific plane in the martensite, in this case the $\{1\ 1\ 2\}$ twin planes. Shen et al. [39] used a different experimental approach, studying cracking in a Ni₂-Mn-Ga alloy using differential interference contrast microscopy. They found that martensite formed first during loading, with the appearance of a plastic zone upon increasing the applied stress. However, these experiments were largely qualitative and performed on Ni-Mn-Ga alloys.

Experimental studies have also been performed on the shape memory alloy CuAlNi. Loughran et al. [17] conducted an experimental investigation into the fracture of single crystals of the shape memory alloy CuAlNi using a high resolution CCD camera attached to a metallurgical microscope to optically observe fracture behavior. These experiments show that details of crack growth in single crystals depend strongly on both the type of microstructure that forms and how this microstructure interacts with the growing crack. Specifically, the observed fracture behavior was strongly dependent on the structural phase transformation the material undergoes. However, as Loughran et al. note, these experiments were designed to give unconstrained microstructures. In the case of polycrystalline shape memory alloys, which are much more commonly used, intergranular constraints will be present. There is a strong need to study the effect of these constraints on the process of fracture.

In addition to the studies of Loughran et al., there have been other studies on the fracture behavior of CuAlNi shape memory alloys. Vasko et al. [18] looked at the formation of martensite near the crack tip in single crystal CuAlNi loaded in tension. The experimentally observed martensitic microstructures near the crack tip were compared with

predictions from the combined stress field and Crystallographic Theory of Martensite (CTM). It was found that this method could accurately predict the orientation, number, and order of the austenite-martensite interfaces that initially form near a crack. Shek et al. [19] experimentally determined the fracture toughness of CuAlNi single crystals, and found that the parent phase has a higher value of fracture toughness than the martensite phase due to stress-induced transformation. Lu et al. [40] studied the CuAlNi alloy by using *in-situ* microscopy to investigate the mechanism of microcrack initiation. They found that various martensite phases appeared around the notch tip on loading, followed by microcracks that initiated along the martensite/parents interface. Recent work by Crone et al. [41] discusses a combination of indentation techniques and crystallographic information obtained by Electron Backscatter Diffraction (EBSD) in order to compare observed surface features to predicted austenite-martensite interfaces, slip planes, and possible fracture planes of CuAlNi. There have been an increasing number of experimental studies utilizing indentation techniques, particularly on thin films on Nitinol (see, for example, [41] and the references therein).

Although there have been a number of experimental investigations into the fracture properties of shape memory alloys, many of them concentrate on single crystals, and few of them concern the fracture properties of Nitinol. Though some measurements can be found in a study of the effect of hydride and hydrogen-induced martensite on the fracture toughness of Nickel-Titanium [42, 43], no clear value has been established to date. The usual setups for fracture toughness measurements have generally included bulk material (thickness > 1 mm) with compact tension specimens or thin sheets (thickness < 10 microns) using indentation methods. Very few researchers have investigated the intermediate thickness

range of 100 microns, which is of practical importance in biomedical applications such as stents.

In this chapter, full-field measurements of the strain during stress-induced martensitic phase transformations near the crack tip of an edge-cracked specimen of a nominally 150 micron polycrystalline Nitinol sheet under uniaxial tension are presented for the first time. These measurements are obtained using Digital Image Correlation (DIC), an *in-situ* optical method that measures displacement on the surface of an object by tracking and correlating a random pattern on the sample surface [25]. The observations show the shape of the martensite and transformation regions as well as strain distribution inside those regions. The value of the fracture toughness K_{IC} for thin sheets is also determined for the first time. These measurements are the first full-field strain measurements detailing localization in Nitinol during fracture. Combined with the relatively high fracture toughness, they indicate a complex mechanism where phase transformation contributes to toughening around the crack tip. The results presented here, including the full-field evolution of strain fields, could provide important insights for developing appropriate fracture criteria as well as for phase transformation under multi-axial loading conditions.

3.2 Material and Experimental Details

Samples were cut from rolled sheets with a nominal thickness of 160 μm and composition of 52 wt.% Nickel and 48 wt.% Titanium. The sheets were flat annealed with an A_f temperature of 11.3 degrees Celsius. The low A_f ensured that the specimens were fully austenitic when unloaded and that the stress-induced martensite occurred upon loading at room temperature. The nominal (engineering) stress-strain curve at room temperature for the Nitinol material deformed at 10^{-3} s^{-1} in uniaxial tension under investigation is shown in

Figure 3.1. This stress-strain curve was obtained with the techniques described in Chapter 2. The superelastic plateau stress is around 500 MPa. The strains at the onset (austenite to martensite) and completion (fully martensite) are approximately 0.015 and 0.05, respectively.

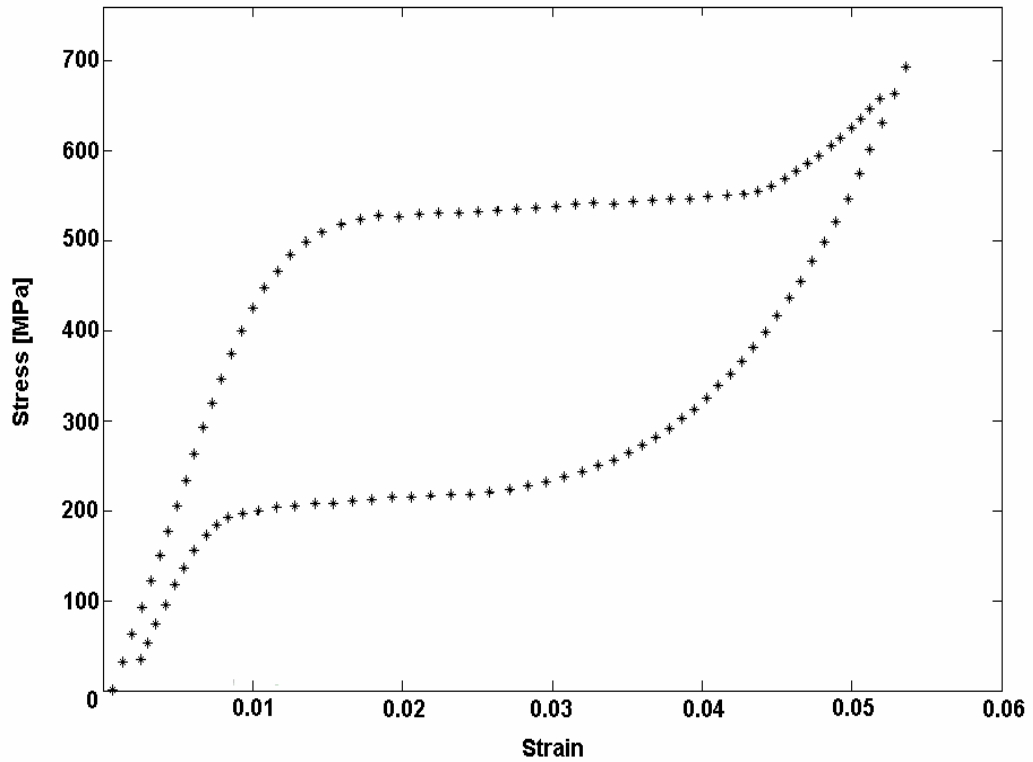


Figure 3.1: Nominal (engineering) stress-strain curve for Nitinol deformed in uniaxial tension at room temperature under a strain rate of 10^{-3} s^{-1}

Rectangular samples of 13 mm x 30 mm with a nominally 6 mm long sharp edge crack were cut parallel to the rolling direction of the sheet. The specimen geometry of the edge cracked panel and the idealized conception of various regions undergoing phase transformation for Nitinol are shown in Figure 3.2. In Figure 3.2, x_1 - x_2 are the cracktip coordinates and a and w are the crack length and width of the specimen, respectively.

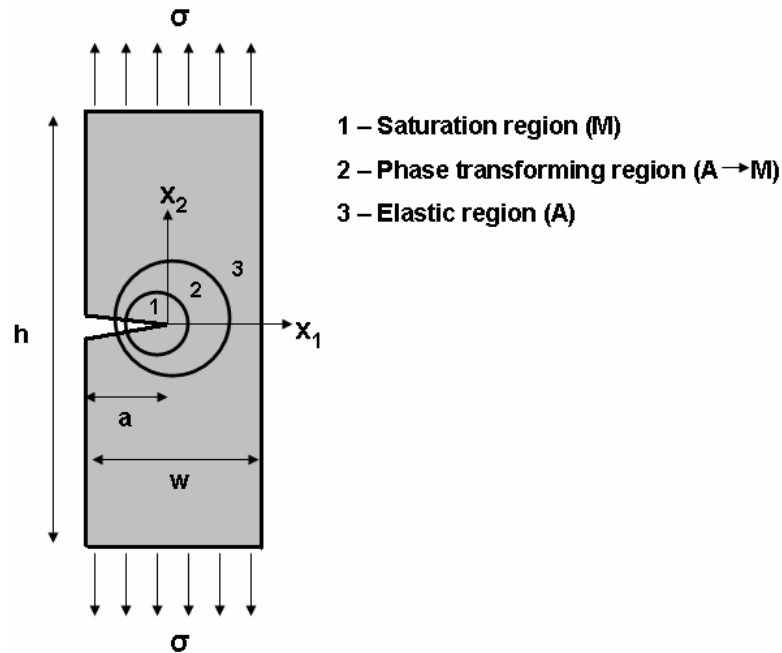


Figure 3.2: Edge-cracked specimen geometry showing the coordinate system and dimensions. An idealized conception of various phase transforming zones near the cracktip is illustrated (1 - Martensite, 2 - Phase Transforming Zone, 3 - Austenite). This figure is not to scale. The actual transformation regions are much more closely confined to the crack tip.

The edge cracked specimens were tested in uniaxial tension at room temperature under displacement control using a computer-controlled servo-hydraulic machine (MTS model #358.10). Knurled grips were used to minimize slippage and were carefully aligned to minimize out-of-plane loading and displacement. Grip slippage was also minimized by attaching emery paper to the grip sections of the sample in order to maximize friction in the connection between the grips and the sample. Specimens were tested with a fixed bottom grip and moving upper grip, both of which were supported by pivots to minimize bending and shear in the specimens. The specimens were deformed at a nominal strain rate of 10^{-3} s^{-1} . This is somewhat higher than the 10^{-4} s^{-1} recommended by various researchers for isothermal tests, but was found to be adequate for our thin sheets and enabled the variety of observations that were recorded.

Strain in the specimen was measured using the optical technique of Digital Image Correlation (DIC). Details of this technique and a discussion of possible sources of error can be found in Section 2.2.

3.3 Results and Discussion

The main goals of this work were to apply DIC to study the fracture of pseudoelastic shape memory alloys, provide high quality quantitative visualization of the cracktip fields during phase transformation at the cracktip for the first time, and to determine the value of the fracture toughness K_C for thin sheets of Nitinol.

3.3.1 Stress Intensity Factor and Fracture Toughness

The mode-I stress intensity factor for an edge-cracked panel under uniaxial tension is,

$$K_I = f\sigma\sqrt{\pi a_{eff}} \quad (3.1)$$

where f is a dimensionless parameter or function dependent on specimen and crack geometry, σ is the global applied stress, and a_{eff} is the effective crack length. Since the phase transformation zone is small and confined to the region close to the crack tip, we will

approximate $a_{eff}=a$. The function f for an edge crack in an infinite length sheet with $\frac{a}{w} \leq 0.6$

[44] is,

$$f\left(\frac{a}{w}\right) = \sec\left(\frac{\pi a}{2w}\right) \sqrt{\left(\frac{2w \tan\left(\frac{\pi a}{2w}\right)}{\pi a}\right)} \left[0.752 + 2.025\left(\frac{a}{w}\right) + 0.37\left(1 - \sin\left(\frac{a}{w}\right)\right)^3\right] \quad (3.2)$$

where w is the width of the sample, which is 13 mm. Sharp edge cracks were cut into the sample before each test and the length, a was measured prior to testing. The applied stress σ was calculated by dividing the measured load by the cross-sectional area of the specimen.

Several tests with different a/w ratios were performed until failure. The maximum load was recorded and was used to compute the fracture toughness using Equation 3.1. The corresponding values for the fracture toughness K_{IC} are shown in Figure 3.3. The results are independent of the ratio a/w , which is as expected. The average value of $\overline{K_{IC}} = 51.4$

$MPa\sqrt{m}$ and the standard K_{IC} deviation is $3.6 MPa\sqrt{m}$.

The relatively high value of the fracture toughness in this case is attributed to the effect of phase transformation on crack tip shielding. This is supported by a small-scale transformation (SST) analysis of a crack in Nitinol under plane stress conditions, details of which are found in Chapter 4. Studies on the fatigue-crack propagation behavior of Nitinol conducted by McKelvey and Ritchie [33] also conclude that stress-induced martensitic phase transformation occurs in the vicinity of the crack tip for very thin superelastic austenite samples. However, in plane strain samples, McKelvey and Ritchie found that superelastic phase transformation ahead of the crack tip is suppressed, leading to a low fatigue threshold and high crack-growth rate in Nitinol compared to other biomedical metallic alloys. The difference in fatigue and crack growth behavior observed in samples in plane stress versus plane strain is a topic necessitating further study, especially when considering the numerous biomedical applications of Nitinol devices with widely varying dimensions and states of stress.

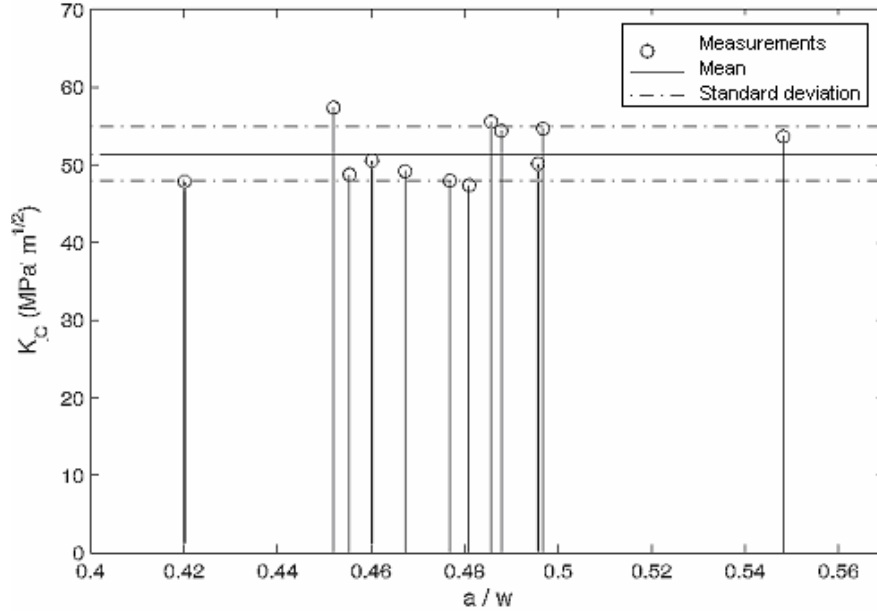


Figure 3.3: Fracture toughness (K_c) values obtained for thin ($\approx 150 \mu\text{m}$ thickness) sheet of Nitinol at room temperature, using an edge cracked specimen, for various values of (a/w)

3.3.2 Fracture Surface

Edge-cracked fracture samples with varying orientation with respect to the rolling direction (RD) were extracted from the same sheet and subjected to a quasi-static uniaxial tension test until failure. SEM images of the resulting fracture surfaces are shown in Fig. 3.4 for three specimens, oriented along the RD, 45 degrees to the RD, and perpendicular to RD, respectively.

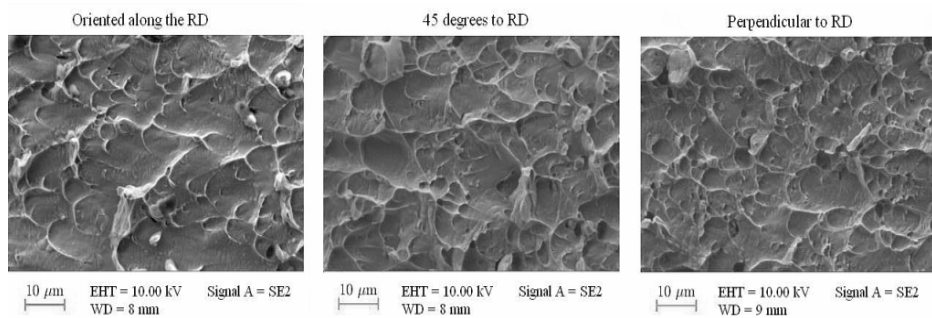


Figure 3.4: Scanning electron micrographs of fracture surfaces in the vicinity of the crack tip for a crack oriented (a) along the rolling direction (RD), (b) 45 degrees from the RD, and (c) perpendicular to the RD

The fracture surfaces observed using scanning electron microscopy (SEM) are consistent with previous experimental observations made in Chapter 2, where uniaxial tensile specimens aligned along the RD accommodated a significantly higher transformation strain than other textures. In Figure 3.4, all images show the void growth and coalescence characteristic of ductile fracture. However, the void growth in the fracture surface of the specimen with the crack oriented along the RD shows a reduced symmetry, indicating a higher amount of shear at failure which may be due to the elongated austenite grains in the RD. The micromechanics of fracture and its dependence on texture need further investigation.

3.3.3 Strain Fields

Two aspects of the strain field in the vicinity of the cracktip will be highlighted in the following section: the elastic field outside the phase transformation zone, and the field close to the crack tip where phase transformation (from austenite to martensite) and saturation (martensite) occurs. The strain field, ϵ_{22} , is the strain along the direction normal to the crack tip. The samples used were edge-cracked specimens with nominally $a/w = 0.48$ and a nominal thickness of 150 μm , where a and w are the length of the crack and width of the specimen respectively. The strain fields around the cracktip are characterized using the DIC technique described in Section 3.2.3.

3.3.3.1 Elastic field

First, the elastic field far from the crack tip is considered. Figures 3.5a - c present a detailed progression of the fracture behavior for the edge-cracked specimen subjected to

uniaxial tension under displacement control for applied $K_I = 25, 33, \text{ and } 44 \text{ MPa}\sqrt{\text{m}}$, respectively. Snap-shots of the specimen were taken after each displacement increment, and the strain distributions (ϵ_{22}) were computed using DIC. The field of view of each image is 600 x 500 pixels (9 x 7.5 mm).

In Figure 3.5a, the strain field shows two inclined lobes, pointing in a direction of approximately 60 degrees from the x_1 axis (crack line). The area of phase transformation and saturation near the crack tip is visible as a small lobe extending parallel to the crack tip. Phase transformation will be discussed in greater detail with higher resolution in the next section, but one should be aware that it is still present and visible at this scale. In Figures 3.5b and 3.5c, the two elastic lobes grow significantly but maintain the same shape and orientation as the load increases.

Figure 3.6 shows strain as a function of distance from the cracktip for various levels of the stress intensity factor. Far from the crack tip, the strain is relatively constant. As one approaches about 1.5 mm from the crack tip, one begins to see the $\frac{1}{\sqrt{r}}$ dependence predicted by linear elastic fracture mechanics, until approximately $x_1 \leq 0.3 \text{ mm}$, where phase transformation begins. The actual value of strain when phase transformation and saturation begin is of course dependent on K_I . This dependency is discussed in the following section.

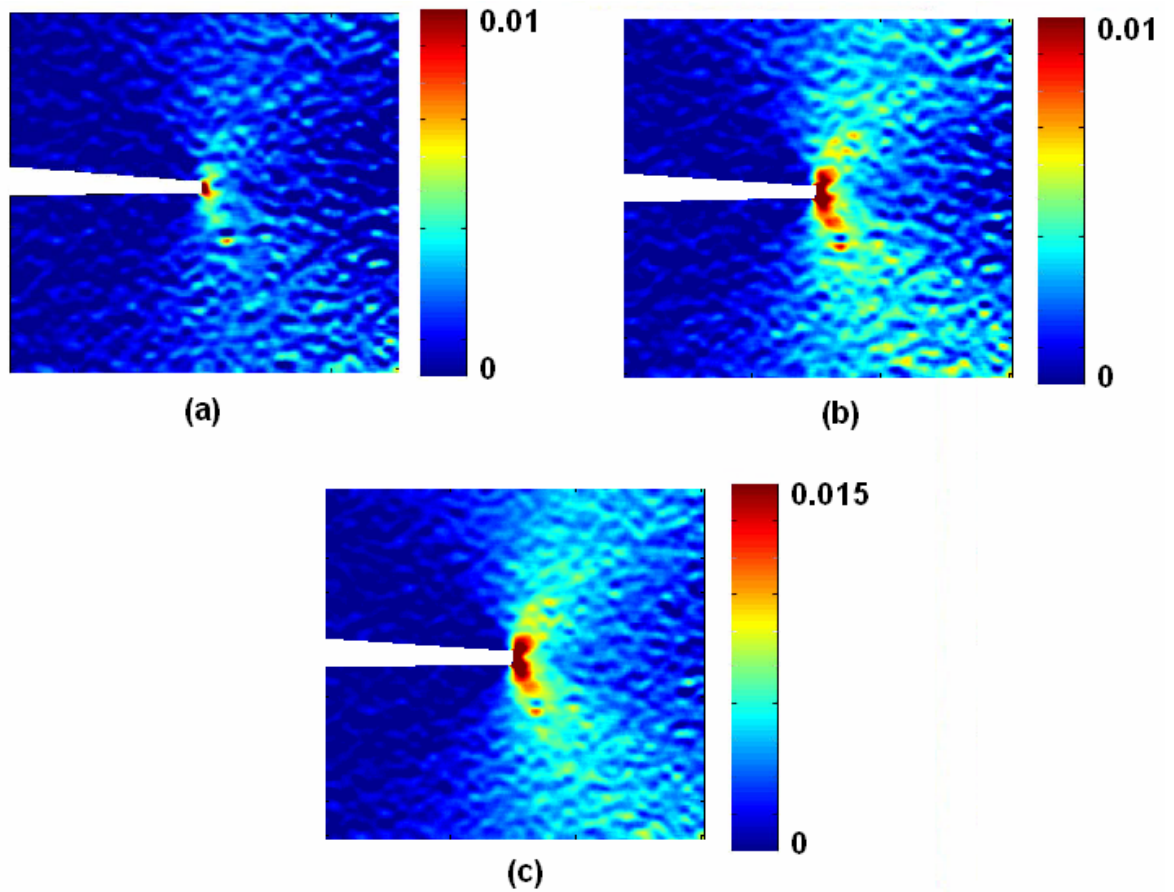


Figure 3.5: Full field normal (ϵ_{22}) strain fields obtained using DIC in the vicinity of the crack tip for various values of applied K_I (in $MPa\sqrt{m}$), (a) 25, (b) 33, and (c) 44. The field of view is 9 mm (width) by 7 mm (height).

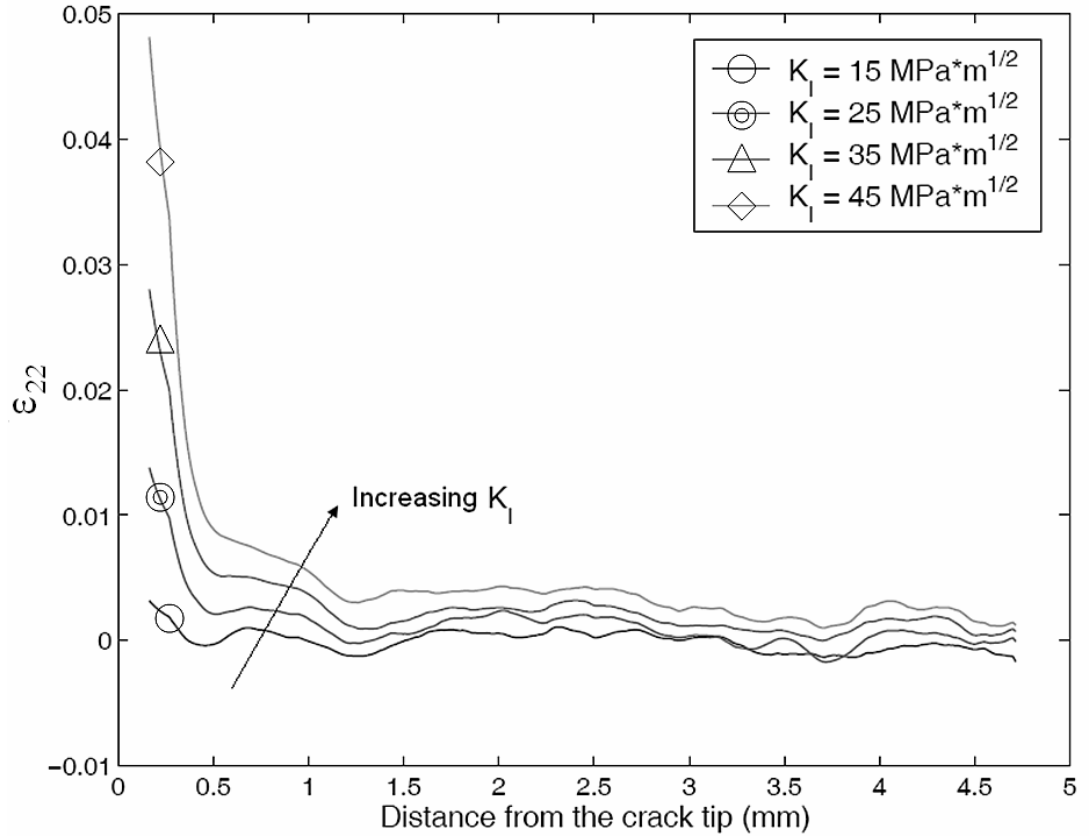


Figure 3.6: Normal (ϵ_{22}) strain distribution along a line ahead of the cracktip at various values of applied K_I shown in the legend.

3.3.3.2 Phase Transformation Field

Figures 3.7a - d present a detailed progression of the phase transformation in the edge-cracked specimen subjected to uniaxial tension under displacement control, but at higher resolution than in Figures 3.5a - c shown in the study of the much larger elastic field. Here the strain fields are shown in a 110 x 150 pixel (1.6 x 2.2 mm) field of view centered on the cracktip, which allows us to investigate the area of high stress and phase transformation immediately around the crack tip. Snap-shots of the specimen were taken at this higher magnification after each displacement increment, and the strain distributions were computed using DIC.

Figures 3.7a - d show the crack tip strain field for applied $K_I = 28, 38, 47,$ and 51 $MPa\sqrt{m}$, respectively. Assuming that the phase transformation from austenite to martensite occurs for strains approximately between 1.5% and 4.5% from the stress-strain curve shown in Figure 3.1, it is straightforward to visually track the transformation zones. Following this convention for transformation strain and looking along the line $\theta=0$ and $x_1 \geq 0$ in Figure 3.7a, there is saturation from the crack tip at $x_1=85$ pixels until $x_1=105$ pixels, when we are sufficiently far enough away from the crack tip for the strain to decrease to 4.5%. The spatial resolution of the measurements is 67 pixels per mm. Thus, the size of the saturation zone is 0.3 mm. From $x_1=105$ pixels, the phase transition zone extends to the right until the strain decreases to 1.5% at $x_1=120$ pixels, which corresponds to an additional distance of 0.2 mm past the saturation zone along the line ahead of the crack tip. The material is untransformed austenite for distance, $r > 0.5$ mm. At this applied level of loading K_I , the shape of the transformation zone can be viewed as a lobe that is an extension of the previously existing crack.

As we increase K_I to $38 MPa\sqrt{m}$ in Figure 3.7b, the shape of the transformation zone grows longer. It still grows primarily in the x_1 direction, although there is a hint of the formation of lobes at 60 degrees to the x_1 axis. Following the same methodology as for $K_I=28 MPa\sqrt{m}$, here the saturation zone ($\epsilon_{22} > 4.5\%$) extends to $x_1=0.37$ mm ($x_1=110$ pixels) and the transformation zone extends an additional 0.23 mm past the saturation zone along the line ahead of the crack tip. The material is untransformed austenite at $x_1 > 0.60$ mm.

As K_I continues to increase in Figures 3.7c - d, the transformation zone extending horizontally ahead of the cracktip continues to slowly increase in length. In addition, there is

now the formation of two distinct lobes pointing 60 degrees from the x_1 axis at the end of the horizontal transformation zone. Figure 3.7c, for $K_I=47 \text{ MPa}\sqrt{\text{m}}$, shows the two lobes emanating from the end of this high-strain region that extends parallel to the crack. In Figure 3.7d, for $K_I=51 \text{ MPa}\sqrt{\text{m}}$, it is observed that both the region parallel to the crack and the two lobes continue to grow.

The variation of the strain field ahead of the crack tip along the x_1 axis is shown on Figure 3.8. In comparison to Figure 3.6, which details the nominally elastic region defined by $r \in [0,5] \text{ mm}$ and $\varepsilon_{22} \in [0,0.05] \text{ mm}$, Figure 3.8 details the phase transformation region defined by $r \in [0,1] \text{ mm}$ and $\varepsilon_{22} \in [0,0.4] \text{ mm}$. Note that the curves in Figure 3.8 have been smoothed in the post-processing algorithm, due to the large strains and small region under investigation. The nature of the strain field in the vicinity of the crack tip can be characterized as follows:

- For $x_1 > 0.5 \text{ mm}$, the region is elastic and the strain field can be adequately described by $\frac{1}{\sqrt{r}}$.
- The phase transformation region is approximately $0.2 < x_1 < 0.5 \text{ mm}$. The variation of the strain in this region is approximately linear.
- The strain versus distance curve changes its curvature and becomes convex for the 0.2 mm closest to the crack tip. This change in curvature and convexity could be evidence of the elastic behavior of the martensite in the fully transformed region near the crack tip.

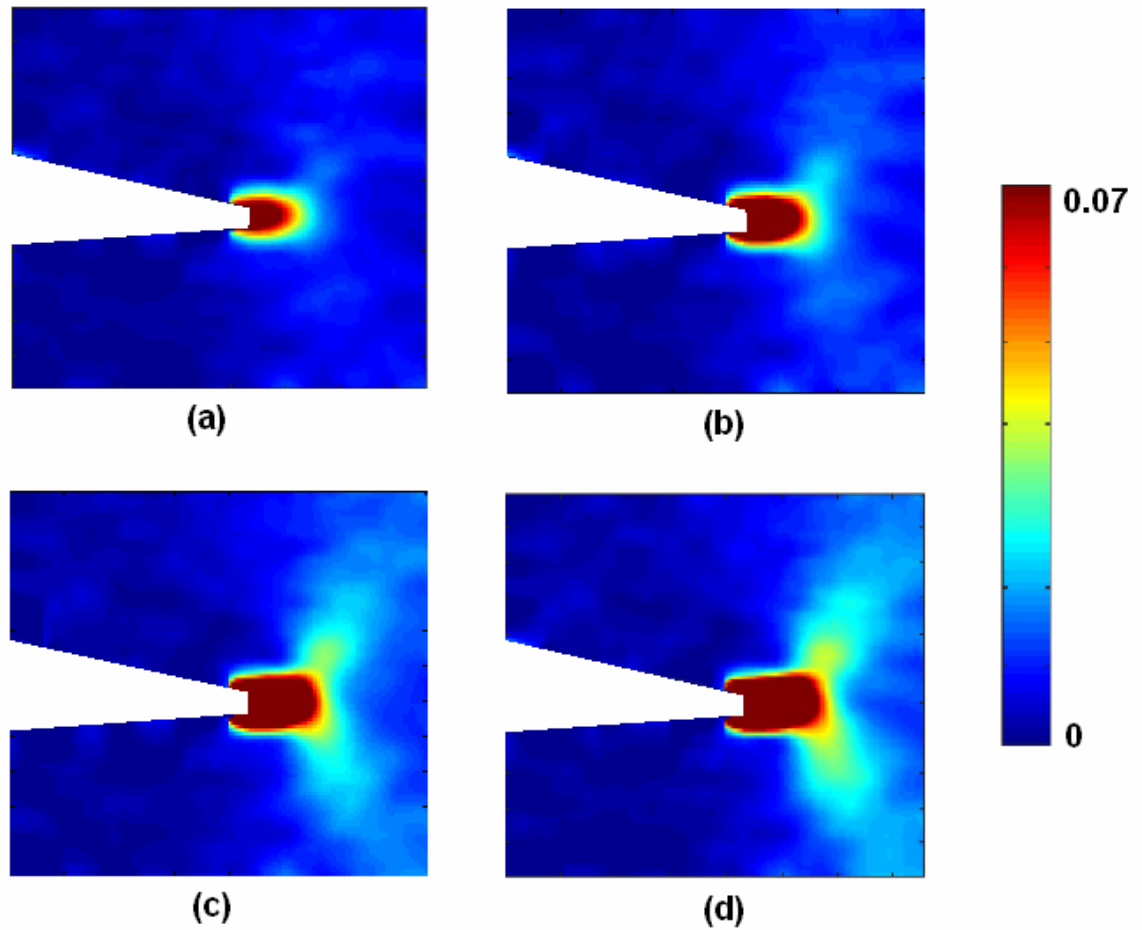


Figure 3.7: Full field normal (ϵ_{22}) strain fields obtained using DIC in the close vicinity of the crack tip for various values of applied K_I (in $MPa\sqrt{m}$), (a) 28, (b) 38, (c) 47, and (d) 51. The field of view is 2 mm (width) by 1.6 mm (height). The field of view is a zoom of the region near the crack tip visualized in Figure 3.5.

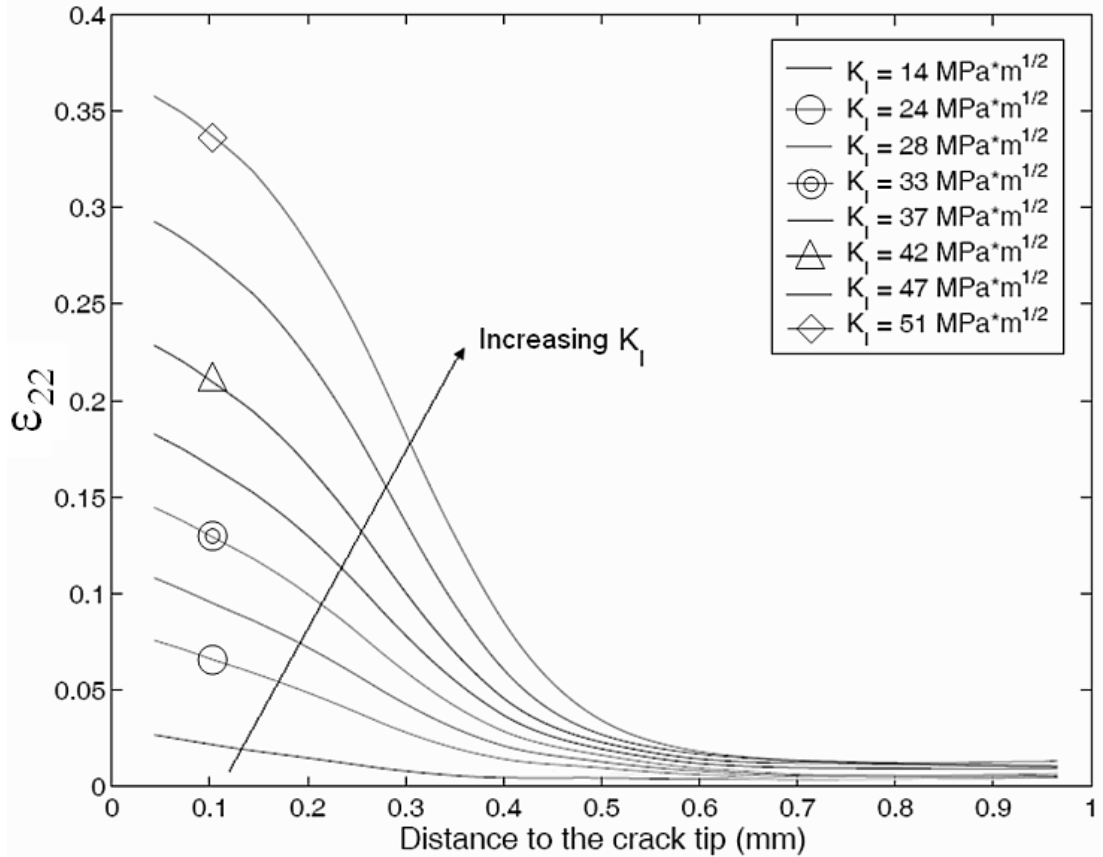


Figure 3.8: Normal (ϵ_{22}) strain distribution as a function of distance along a line ahead of the crack tip at various levels of K_I shown in the legend.

The radius of the phase transforming ($A \rightarrow M$) zone, r_{TRA} , and of the saturation zone (M), r_{SAT} , are plotted as functions of loading parameter $\frac{K_I^2}{2\pi\sigma_0^2}$ in Figure 3.9. The loading parameter K_I is in units of $\text{MPa}\sqrt{\text{m}}$, and σ_0 , the stress at which transformation begins, is taken to be 500 MPa. The zone sizes in meters are defined as the intersection of constant strain contours corresponding to 1.5% ($A \rightarrow M$) and 4.5% (M) with the line ahead of the crack tip. The zone sizes increase linearly with the chosen loading parameter, which is consistent with the results of the small scale transformation (SST) analysis detailed in Chapter 4. However, note that there is a slight change in the slope of the radius of

transformation from 0.238 between $K_I = (28, 38) \text{ MPa}\sqrt{\text{m}}$ to 0.160 between $K_I = (47, 51) \text{ MPa}\sqrt{\text{m}}$. This is attributed to the formation of lobes at $K_I = 47 \text{ MPa}\sqrt{\text{m}}$, as seen in Figure 3.7c. Since the radius of the transformation zone is taken to be the intersection of the 4.5% constant strain contour with the line ahead of the crack tip, this measurement only takes into account the main lobe extending parallel to the crack tip, not the new lobes angled to the crack tip. When the new lobes appear, there is a perceived decrease in the rate of expansion of the phase transformation zone extending directly parallel to the crack tip.

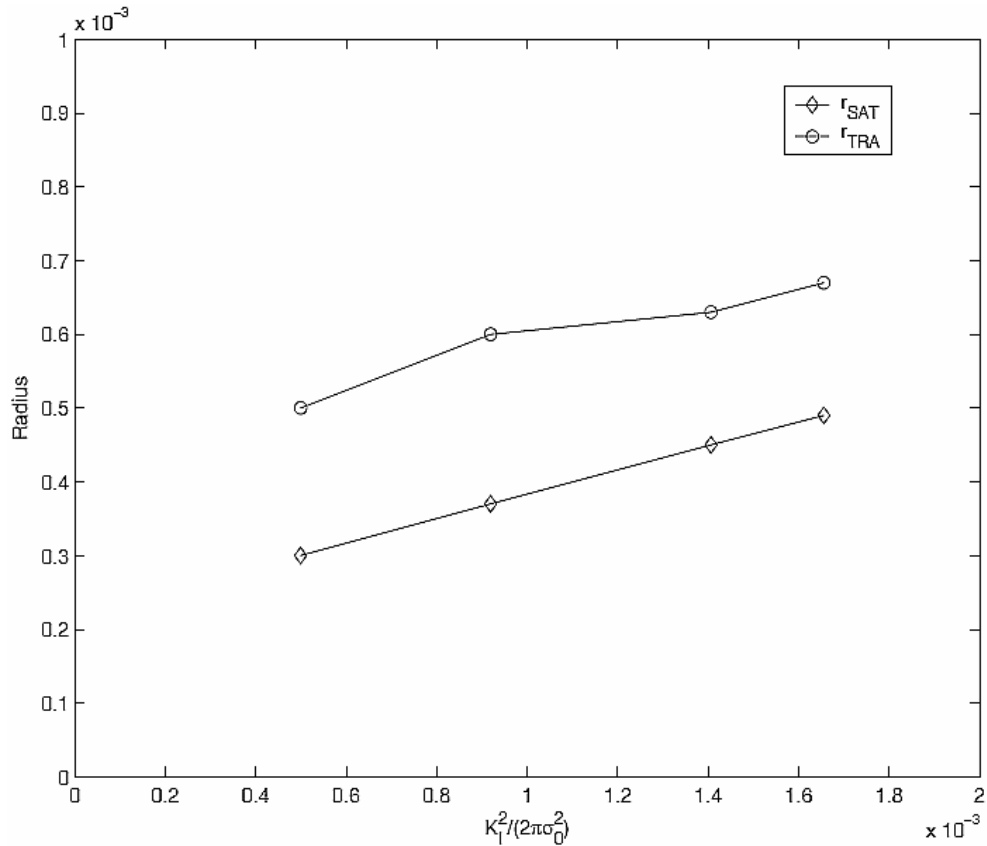


Figure 3.9: Radius of the saturation zone (r_{SAT}) and phase transformation zone (r_{TRA}) as a function of $\frac{K_I^2}{2\pi\sigma_0^2}$. K_I is in $\text{MPa}\sqrt{\text{m}}$, σ_0 denotes the stress at which phase transformation begins, and is taken to be 500 MPa (see Figure 3.1). The radii of the saturation and transformation zones are in meters.

Using this convention, the saturation and phase transforming zone sizes can be expressed as a function of the loading parameter,

$$r_{SAT} = 0.164 \frac{K_I^2}{2\pi\sigma_0^2} \quad (3.3)$$

$$r_{TRA} = 0.136 \frac{K_I^2}{2\pi\sigma_0^2} \quad (3.4)$$

It is noted that r_{TRA_C} at crack initiation ($K_I=K_C$) is ≈ 0.7 mm, which is much smaller than the crack length ($\frac{a}{r_{TRA_C}} \approx 9$) and the specimen width ($\frac{w}{r_{TRA_C}} \approx 20$). This validates the specimen design as well as the measured value of K_C under small-scale transformation conditions.

3.4 Summary

This chapter details the experimental investigation of martensitic transformation around the crack tip in thin sheets of Nitinol. Many applications of Nitinol require its use in the form of thin sheets. One of the important failure criteria for the analysis and design of such devices is the fracture toughness, of which there are currently no recorded values for thin sheets on the order of 100 microns thickness. Using edge-cracked specimens, an average fracture toughness (K_C) value of $51.4 \pm 3.6 \text{ MPa}\sqrt{\text{m}}$ for fine-grained polycrystalline Nitinol sheets ($A_f = 11.4$ °C) at room temperature was measured.

The use of DIC in these fracture experiments enabled a non-contact optical method of obtaining information about the crack tip fields in these thin sheets under displacement-

controlled uniaxial tension. The shape of the transformation zone can be described in the form of three lobes, one along the x_1 axis that grows larger with the load, and two lobes pointing at 60 degrees from the x_1 axis that appear at larger values of K_I . Using the strain fields obtained from DIC, and assuming that phase transformation occurs from 1.5% to 4.5% strain, the approximate lengths of the saturation and transformation zones for various values of K_I were determined. The use of DIC enabled the first full-field quantitative mapping of the strain fields in the vicinity of the crack tip of edge-cracked specimens of Nitinol. The images, combined with the relatively high value of fracture toughness for thin sheets of Nitinol, indicate a complex mechanism where phase transformation contributes to toughening around the crack tip. The criteria for phase transformation and saturation near the crack tip need further investigation. The results presented here, including the full-field evolution of strain fields, could provide important insights for developing appropriate fracture criteria as well as for phase transformation under multi-axial loading conditions.

4 Small-Scale Transformation Analysis of Nitinol Near a Crack Tip Under Plane Stress Conditions

4.1 Introduction

The fracture properties of shape memory alloys are relatively poorly understood both from an analytical and an experimental point of view. This is due to the lack of constitutive models for this class of materials that are amenable to computational implementation, as well as the limited availability of these materials in bulk form for laboratory measurements.

Recent numerical studies on shape memory alloys have been performed by Yi and Gao [45, 46]. In 2000, they investigated the fracture toughening mechanism of shape memory alloys due to martensitic transformation in plane strain under mode I loading [45]. The analytic results show that martensitic transformation reduces the crack tip stress intensity factor and increases fracture toughness. By performing a fracture toughening analysis of shape memory alloys with a macrocrack under mixed mode loading [46], they saw non-symmetric transformation boundaries for both static and steadily advancing cracks, and showed that under mixed-mode loading the martensitic transformation again reduced crack tip energy release rate and increased toughness. Interestingly, in experimental fatigue studies on plane strain samples, McKelvey and Ritchie [33, 34] found that superelastic phase transformation ahead of the crack tip is suppressed, leading to a low fatigue threshold in Nitinol compared to other biomedical metallic alloys.

Birman [47] conducted an analytical and numerical study on the mode-I isothermal fracture of shape-memory alloy plates in plane stress. The study was based on a two-dimensional version of the Tanaka constitutive model for shape memory alloys [48]. Birman found that the effect of phase transformation on the stress-intensity factor is relatively small, and suggests that the magnitude of the stress intensity factor can be based on the properties

of the austenite. However, he notes that “the principal problem in estimating the anticipated failure of a SMA component is related to the evaluation of the fracture toughness. This parameter will also be affected by the stress-induced transformation in front of the crack and an extensive experimental investigation is needed to generate reliable estimates.” A challenging topic that still needs future investigation numerically and experimentally is how a complex texture, like that found in polycrystalline Nitinol, influences the martensitic transformation around the crack tip and the fracture toughness of the sample.

In another approach towards understanding the effect of martensitic transformation on fracture properties, Dang and Grujicic [49] performed molecular dynamics simulations to investigate the region surrounding a crack tip in a gamma-TiAl phase impinging at a right angle onto the interface between a gamma-TiAl phase and a metastable Ti-15V (at.%) phase. The crack tip behavior for this two-phase gamma beta material was compared with the crack tip behavior in the corresponding single-phase materials (pure gamma and pure beta crystals). It was found that under the same amount of applied stress, the crack tip blunted and the crack stopped propagating in the two-phase gamma beta material and the single-phase beta material. However, in the single-phase gamma material, the crack extended by brittle cleavage. They found that the blunting process that took place in the two-phase gamma beta and the single-phase beta material was controlled by the martensitic transformation that took place in the beta-phase ahead of the crack tip. These experiments are one example showing that the implications of martensitic transformation on the toughness of materials are not solely limited to Nitinol.

More recently, 3-D constitutive models with appropriate computational algorithms have been proposed for shape memory alloys, such as the Auricchio-Taylor-Lubliner model [50, 51], which has been implemented in the commercial computational finite element

software such as the ABAQUS [52]. Wang et al. [53] investigated the formation of martensite in front of cracks in superelastic Nitinol using the ABAQUS implementation for superelastic Nitinol. The material parameters required in the model were obtained in this case from data from pull-pull tests on pseudoelastic Nitinol wires. They examined the stress-induced martensitic transformation zone near the crack tip of a compact tension (CT) specimen with and without pre-cracks. They found that the size of the martensitic and transformation zones increases with crack length, and that cracks propagate into the stress-induced martensite. Wang et al. also noted the similarities between the formation of stress-induced martensite in front of a crack tip and the formation of a plastic zone in front of a crack tip in a material undergoing plastic deformation. This assertion is supported by the experimental investigations detailed in Chapter 3, in which the transformation zones obtained through DIC bear noticeable resemblance to the plastic zones that appear in more traditional materials during fracture.

The focus of this chapter is to provide a basic foundation for understanding the fracture mechanics of Nitinol under plane stress conditions by modeling the two-dimensional small-scale transformation behavior. For this purpose, the Auricchio-Taylor-Lubliner constitutive model [50, 51] implemented in the finite element code ABAQUS [52] is used. Realistic material properties of thin sheets of Nitinol are estimated from the displacement-controlled uniaxial tension data obtained in Chapter 2. Nomenclature that will be used throughout this chapter can be found in Table 4.1.

This chapter is outlined as follows. The constitutive model used to investigate small-scale yielding of Nickel-Titanium alloy (Nitinol) is discussed briefly in Section 2. Section 3 is devoted to a detailed case study of small-scale transformation with specific material parameters. Section 4 then expands upon Section 3 to parametrically study the effect of

material parameters on the fracture properties and transformation zones near the crack tip. In Section 5, conclusions for the finite element study are presented.

Table 4.1: Chapter 4 Nomenclature

E_A	Young's modulus (austenite)
E_M	Young's modulus (martensite)
K_I	Stress intensity factor (applied)
T_0	Reference temperature
$\left(\frac{\delta\sigma}{\delta T}\right)_L$	Rate of stress increase with change in temperature during loading
ε^L	Transformation strain
ε_V^L	Volumetric transformation strain
ε_{pt}	Strain at which phase transformation occurs
ε_{sat}	Strain at which saturation occurs
σ_L^S	Stress at the start of transformation during loading
σ_L^E	Stress at the end of transformation during loading
σ_U^S	Stress at the start of transformation during unloading
σ_U^E	Stress at the end of transformation during unloading
ν_A	Poisson's ratio (austenite)
ν_M	Poisson's ratio (martensite)
α	Pressure sensitivity parameter

4.2 Constitutive Model

The uniaxial stress-strain curve for Nitinol deformed at a temperature well above its austenitic finish (A_f) temperature is shown schematically in Figure 4.1. Prior to deformation, the material is entirely austenitic (A). Upon loading, the material behaves in a linearly elastic manner, until it reaches the stress at which the material begins to transform to the

low-temperature phase, martensite (S). Upon further loading the austenite is further transformed to martensite resulting in complete transformation at a stress level, σ_L^E . Upon further loading, the material once again deforms in a linearly elastic manner, with a moduli corresponding to that of the stress-induced martensite. Upon unloading, the material unloads and the reverse transformation from martensite to austenite starts at a stress level, σ_U^S , and reverts to austenite at a stress level, σ_U^E .

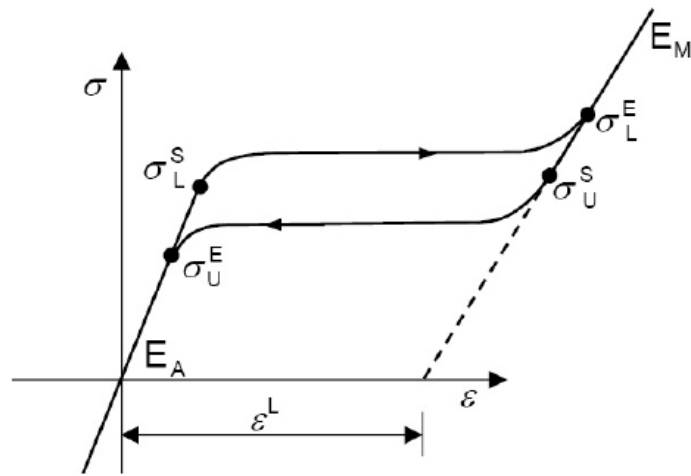


Figure 4.1. Schematic of a typical stress-strain curve for Nitinol. Schematic and nomenclature for material properties adapted from ABAQUS [52].

An important consideration when modeling the behavior of Nitinol is its superelastic property. The transition between austenite and martensite covers a large amount of strain at a nominally constant stress, as seen in Figure 4.1 between points σ_L^S and σ_L^E upon loading and σ_U^S and σ_U^E upon unloading. As seen in Figure 4.1, Nitinol exhibits large hysteric behavior in stress-strain response. In this chapter, the material begins as austenite prior to deformation and is stress-induced to transform to martensite at the crack tip under displacement control at a constant temperature. Only displacement-controlled loading is

considered and no unloading is allowed in any part of the material domain. This allows one to use the concept of the J -integral [54] in determining the energy release rate by idealizing the material to be a nonlinear deformation solid.

4.2.1 Auricchio-Taylor-Lubliner Model

The time discretized three-dimensional thermomechanical constitutive model resulting from Auricchio-Taylor-Lubliner's work [50, 51] has been implemented using an ABAQUS UMAT [52]. Instead of basing the constitutive model for shape memory alloys on the phase-transition micromechanics, they approached modeling from a thermo-mechanical continuum viewpoint based on internal-variable formalism. UMATs are subroutines in ABAQUS that specify user-defined constitutive models for mechanical behavior of solids.

First, the material is assumed to be isotropic; therefore, there is no distinction between the different single-variant species pertinent to single crystals [55, 56]. There are only two phases under consideration, the austenite (\mathcal{A}) and the martensite (\mathcal{S}). Three phase transformations are considered in the model: the conversion of austenite into martensite, the conversion of martensite into austenite, and the reorientation of martensite. Assuming small deformations, the model is based on an additive strain decomposition, in which the total strain is taken as the sum of the elastic strain and the transformation strain. The transformation strain is of the order of 6%, but the elastic strain is much smaller and is limited to a maximum of 2% [52].

The free-energy functional is taken to be quadratic in the elastic strain. Since some transformations display tension-compression asymmetry, a Drucker-Prager-type loading function is introduced to model this effect in all three transformations. For example, in the phase transformation from $\mathcal{A} \rightarrow \mathcal{S}$,

$$F^{AS}(\tau, T) = \|\underline{\boldsymbol{\tau}}\| + 3\alpha p - C^{AS}T \quad (4.1)$$

where $\underline{\boldsymbol{\tau}}$ is the deviatoric part of the stress tensor, p is the pressure, C^{AS} (stress temperature coefficient) and α (pressure sensitivity) are material parameters, and $\|\bullet\|$ indicates the Euclidean norm. Conditions for the transition are based on material parameters such as the relevant transformation stresses and temperatures (T). The initial and final transformation functions are:

$$\begin{aligned} F_s^{AS} &= F^{AS} - R_s^{AS} \\ F_f^{AS} &= F^{AS} - R_f^{AS} \end{aligned} \quad (4.2)$$

where

$$\begin{aligned} R_s^{AS} &= \left[\sigma_s^{AS} \left(\sqrt{\frac{2}{3}} + \alpha \right) - C^{AS} T_s^{AS} \right] \\ R_f^{AS} &= \left[\sigma_f^{AS} \left(\sqrt{\frac{2}{3}} + \alpha \right) - C^{AS} T_f^{AS} \right] \end{aligned} \quad (4.3)$$

In Equations 4.2 and 4.3, σ_s^{AS} , σ_f^{AS} , T_s^{AS} , and T_f^{AS} are material parameters. For the conversion from austenite into single variant martensite [50],

$$F_s^{AS} > 0, F_f^{AS} > 0, \dot{F}_s^{AS} > 0 \quad (4.4)$$

Backward Euler-integration is used to integrate the time-continuous evolutionary equations in order to get the time-discrete evolutionary equations. Strain is the only control variable in the time-discrete models, since from the point of view of the integration scheme, the time-discrete problem is considered to be strain driven. A return-mapping algorithm is used as the integration scheme for the time-discrete model, and a tangent matrix consistent with the time-discrete model is calculated. Note that the constitutive model does not include

the irreversible energy release associated with transformation. For a more detailed discussion of the constitutive model behind the ABAQUS UMAT, refer to [50, 51].

2.2 Small Scale Transformation (SST) Analysis

A static, perfectly sharp crack in two-dimensional (2D) space undergoing small-scale transformation under symmetric (mode-I) loading under plane stress conditions is considered. For computational efficiency, the finite element model is constructed as a half-circle with normalized radius, $R=1$, where it is subjected to displacement boundary conditions corresponding to mode-I loading. The purpose of this analysis is to elucidate the mechanics of transformation at a crack tip in Nitinol and to develop scaling laws for the transforming region and other relevant features. The analysis is performed in the same spirit as the small scale yielding analyses in elastic-plastic fracture problems. The term small scale transformation (SST) is used to denote problems where the transforming and fully transformed region near the crack tip are fully engulfed by the elastically deforming region, and the asymptotic structure of the solution at the crack tip and the transforming region can be studied in terms of the far field elastic loading. The size of the phase transforming zone is very much smaller than the domain of computation.

Since only mode-I loading (symmetric) is considered, only the upper half of the circular domain is discretized using 4 node quadrilateral plane stress elements (CPS4 in ABAQUS). The aspect ratio $r_{i+1}\Delta\theta / (r_{i+1} - r_i)$ of each element is held constant throughout the mesh. This design avoids excessive mesh distortion and efficiently clusters the elements at the crack tip (Figure 4.2). The radii along the $\theta = 0$ line were determined iteratively, given an initial starting radii for the mesh of $r_1 = 1 \times 10^{-5}$ and $r_2 = 1.2 \times 10^{-5}$. A typical mesh used in the

simulations consists of 1281 nodes and 1216 four node quadrilateral plane stress elements. The mesh consisted of 64 and 20 radial and angular sectors, respectively. Due to convergence issues caused by quarter-point and/or eight-noded elements near the crack tip, all the elements in the domain were 4 node quadrilateral elements. The simulation used large displacement theory, and automatic stabilization with a dissipated energy fraction =2.00x10⁻⁴. Automatic time control was used with a total time period of 1.00, a minimum time increment of 1.00x10⁻⁵, and a maximum time increment of 1.00. The convergence tolerance parameters used in the equilibrium iterations can be found in Table 4.2.

Table 4.2: Convergence tolerance parameters used in equilibrium iterations

Criterion for residual force for a nonlinear problem	5.000x10 ⁻³
Criterion for displacement correction in a nonlinear problem	1.000x10 ⁻²
Initial value of time average force	1.000x10 ⁻²
Alternate criterion for residual force for a nonlinear problem	2.000x10 ⁻²
Criterion for zero force relative to time average force	1.000x10 ⁻⁵
Criterion for residual force when there is zero flux	1.000x10 ⁻⁵
Criterion for displacement correction when there is zero flux	1.000x10 ⁻³
Criterion for residual force for a linear increment	1.000x10 ⁻⁸
Criterion for zero force relative to time average maximum force	1.000x10 ⁻⁵
Criterion for zero displacement relative to characteristic length	1.000x10 ⁻⁸

Plane stress K-field displacement [57] was prescribed as a boundary condition at the outer boundary, R. Assuming that the crack tip is perfectly sharp and that the crack faces remain free of tractions, the asymptotic displacement components for a mode-I crack are,

$$\begin{Bmatrix} u_1 \\ u_2 \end{Bmatrix} = \frac{K_I}{2E_A} \left(\frac{r}{2\pi} \right)^{1/2} \begin{Bmatrix} (1+\nu_A)[(2\kappa-1)\cos(\theta/2) - \cos(3\theta/2)] \\ (1+\nu_A)[(2\kappa+1)\sin(\theta/2) - \sin(3\theta/2)] \end{Bmatrix} \quad (4.5)$$

where E_A is austenite Young's modulus, K_I is the mode-I stress intensity factor, ν_A is the austenite Poisson's ratio, and $\nu = (3 - \nu)/(1 + \nu)$ for plane stress.

Displacements were applied on the boundary according to Equation 4.5 for values of $K_I \in [0, 0.001]$. This ensured that $\left. \frac{r_{sat}}{R} \right|_{\sigma_L^S}$ was on the order of 0.01 and the small-scale transformation condition was satisfied, where r_{sat} is the radius of the fully transformed zone. For all materials considered in this paper,

$$\left(\frac{\delta \sigma}{\delta T} \right)_L = 5.71 \text{ MPa/K [2]}$$

$$\nu_A = \nu_M = 0.33$$

$$E_A = 75 \text{ GPa}$$

$$E_M = 28 \text{ GPa}$$

$$a = 0$$

$$T_0 = 22 \text{ }^\circ\text{C},$$

$$\epsilon_V^L = \epsilon^L$$

All parameters were normalized with R and E_A . The notation convention for material parameters that will be used throughout the paper is adopted from ABAQUS [52] and is shown in Fig. 4.1.

4.3 Results

The room temperature uniaxial true-stress true-strain curve of material I is first considered, in which the (dimensionalized) material values are $\epsilon^L = 0.04$, $\sigma_L^S = 400 \text{ MPa}$,

$\sigma_L^E = 410$ MPa, $\sigma_U^S = 310$ MPa, and $\sigma_U^E = 300$ MPa. These properties approximately correspond to the values for the as received Nitinol alloy with an A_f of 11.4°C investigated in Chapter 2.

4.3.1 The Transformation Zone

In a typical simulation, as K_I increases, there is the relatively quick initiation and progression of a phase transformation region extending outwards from the crack tip. As one continues to increase K_I , the phase transformation region at the point of highest stress, near the crack tip, becomes fully transformed martensite. An example is shown for a high value of $K_I=0.001$ in Figure 4.2. Taking a snapshot at a high value of K_I and moving outwards from the crack tip, a saturation region (fully martensite) is seen immediately around the crack tip, followed by a transition region (partially transformed), and finally ending up in the untransformed (fully austenite) or elastic region.

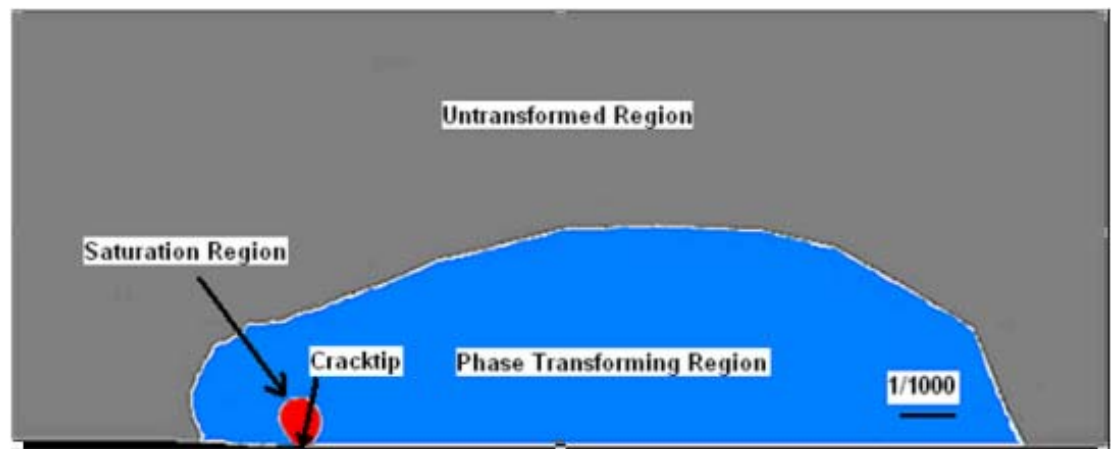


Figure 4.2. Typical shapes of saturation and phase transforming regions near the crack tip ($K_I=0.001$)

4.3.2 The Stress Field

Figures 4.3 - 4.5a, b and c display the angular variation of the stress components, σ_{11} , σ_{22} , and σ_{12} as functions of θ for varying K_I in (a) the saturation (martensite) region near the crack tip, (b) the phase transition region, and (c) the untransformed material far from the crack tip (austenite), respectively. Under the multi-dimensional condition, the criterion for determining saturation is based on effective stress. All the stress components have been normalized by $K_I/\sqrt{2\pi r}$ with appropriate K_I and r , the radius of the circular arc which lies entirely within the corresponding region. In the austenite region, the computed stresses are nearly identical to the theoretical elastic solution for austenite, for all three stress components. Note that in the saturated (martensite) region, the extrapolation of the stress components at nodes where the gradients are steep causes the σ_{22} component to overshoot 0 as θ approaches 180 degrees.

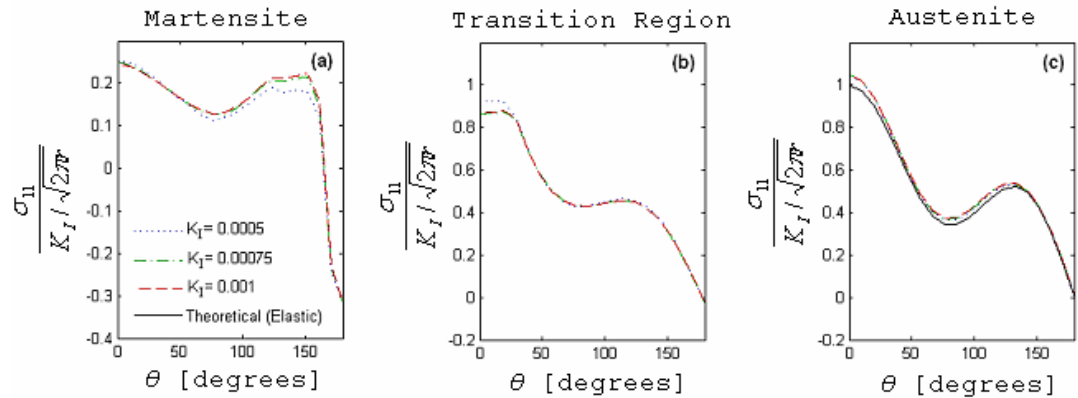


Figure 4.3. Angular variation of the normalized stress component σ_{11} versus θ for normalized $K_I=0.0005$, 0.00075, and 0.001 in the (a) saturated (martensite), (b) partially transformed (mixed phase), and (c) untransformed (austenite) regions. The theoretical (elastic) solution is compared only in the austenitic region.

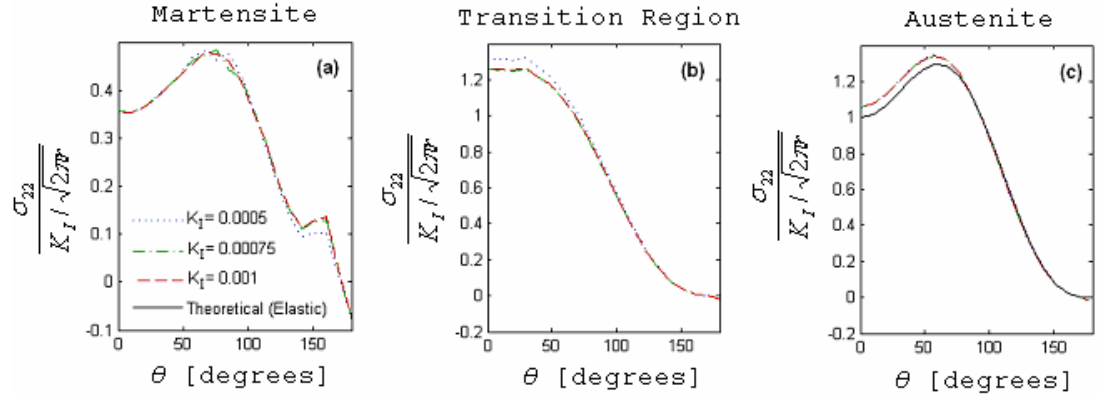


Figure 4.4. Angular variation of the normalized stress component σ_{22} versus θ for normalized $K_I = 0.0005, 0.00075,$ and 0.001 in the (a) saturated (martensite), (b) partially transformed (mixed phase), and (c) untransformed (austenite) regions. The theoretical (elastic) solution is compared only in the austenitic region.

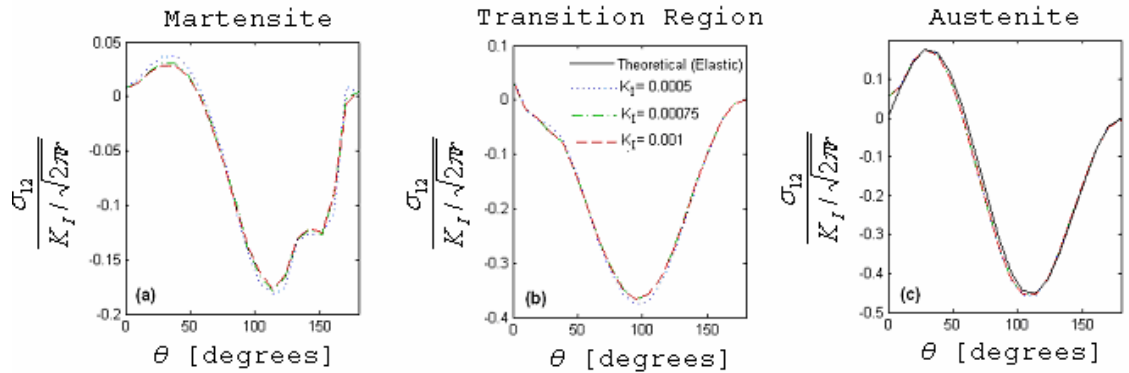


Figure 4.5. Angular variation of the normalized stress component σ_{12} versus θ for normalized $K_I = 0.0005, 0.00075,$ and 0.001 in the (a) saturated (martensite), (b) partially transformed (mixed phase), and (c) untransformed (austenite) regions. The theoretical (elastic) solution is compared only in the austenitic region.

The finite element elastic solution for $\sigma_{22}(K_I, r)$ along $\theta = 0$ for Nitinol undergoing small scale transformation is shown in Figure 4.6 plotted in the logarithmic scale, with the stress normalized with $K_I / 2\pi$. Once again the solution is independent of the applied stress intensity factor in the fully transformed martensite near the crack tip and in the

untransformed austenite region far from the crack tip. In Figure 4.6, the slope of $\sigma_{22}(K_I, r)$ as $r \rightarrow 1$ asymptotically converges to a slope of $-1/2$, since it is in the elastic regime of the untransformed austenite. The rate of this asymptotic convergence slows as the value of K_I is increased. As $r \rightarrow 0$ and one approaches the saturated region near the crack tip, it is expected to be in fully transformed martensite for all values of K_I . As $r \rightarrow 0$, $\sigma_{22}(K_I, r)$ plotted as a function of r in the logarithmic scale has a slope that is approximately -0.55 for $K_I = 0.0005$, -0.66 for $K_I = 0.00075$, and -0.70 for $K_I = 0.001$. The reasons for the deviation of the crack tip singularity from $-1/2$ are not entirely clear at present and need further analysis.

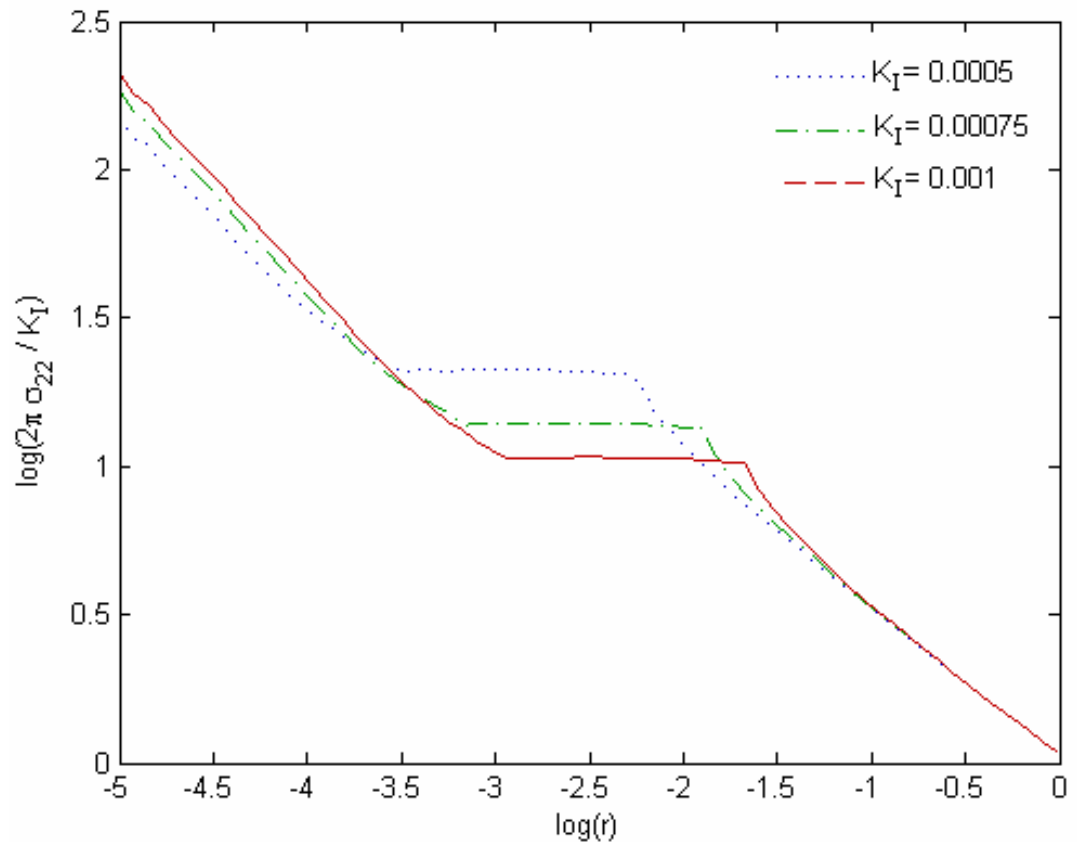


Figure 4.6. Normalized stress component σ_{22} for material I as a function of distance ahead of the crack tip, along $\theta=0$, for varying levels of normalized K_I

An interesting feature of the solution in Figure 4.6 is the relatively constant value of σ_{22} ahead of the crack tip in the mixed phase region undergoing phase transformation. The normalized stress in this region is clearly dependent on the applied loading in a nonlinear manner. Along the line in front of the crack tip ($\theta = 0$), increasing K_I decreases the plateau value of $\sigma_{22}(K_I, r)$ because the saturation zone and phase transition zone are both increasing in size. The expansion of these zones is seen in Figure 4.6, where the plateau value of $\sigma_{22}(K_I, r)$ shifts to higher values of r as K_I increases. The stress plateau in Figure 4.6 also shifts down as K_I increases because the stress is being more evenly distributed throughout these larger transforming zones.

The crack opening displacement u_2 normalized by K_I is plotted in Figure 4.7 as a function of distance on a logarithmic scale along the crack face ($\theta = \pi$) for various values of K_I . For reference, the elastic solution is plotted as a solid line. As expected, the numerical solution agrees with the elastic solution in the far field ($r \rightarrow 1$) austenitic region with the slope of $1/2$. However in the near tip region, the slope is greater than $1/2$, though the behavior of the martensite in this region is once again linear. This result is in agreement with the observations regarding the stress component σ_{22} ahead of the crack tip in the fully transformed region (Figure 4.6).

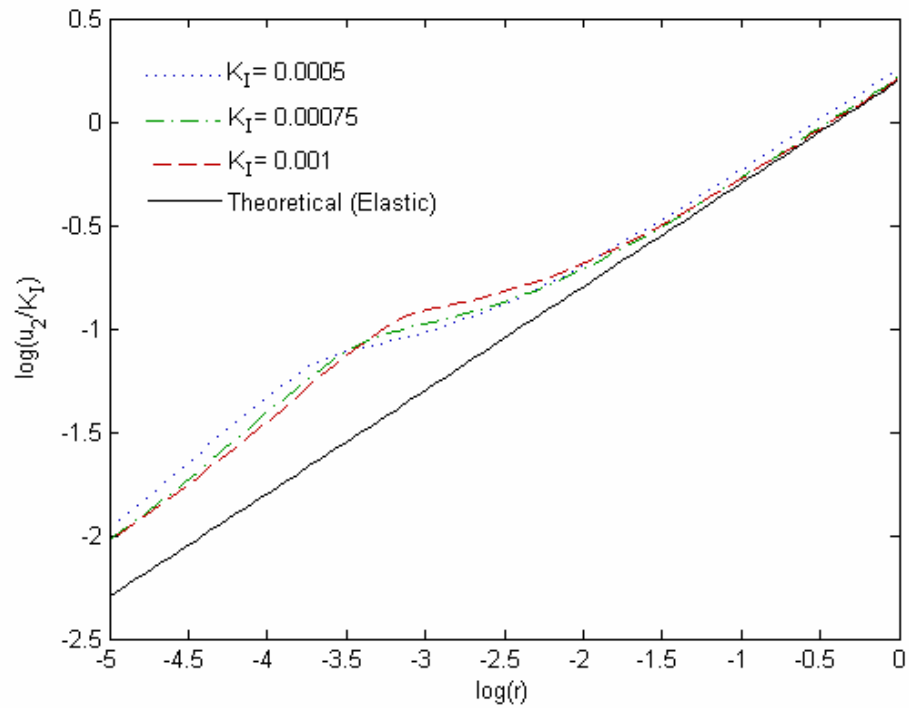


Figure 4.7. Normalized crack opening displacement u_2 as a function of distance on a logarithmic scale along the crack face ($\theta=\pi$) for various values of $K_I=0.0005$, 0.00075 , and 0.001

4.3.3 The Size of the Transformation Region

Figure 4.8 displays the relationship between the radii of the saturation (r_{sat}) and phase transforming (r_{tra}) zones measured along $\theta=0$ versus a normalized length scale, $(K_I^2/2\pi(\sigma_L^S)^2)$, where σ_L^S is the stress at which the transformation begins. These results can be collected into the following scaling laws for the size of the saturation and transformation zones with the far field applied K_I :

$$r_{sat} = 0.029 \frac{K_I^2}{2\pi(\sigma_L^S)^2} \quad (4.6)$$

$$r_{tra} = 3.035 \frac{K_I^2}{2\pi(\sigma_L^S)^2} \quad (4.7)$$

Note that these relations may not hold for very small K_I when the radii become comparable to the numerical discretization.

These scaling laws apply to the radius of the saturated martensite and phase transforming zones in front of the crack tip along $\theta=0$. In reality, both zones have oblong shapes. The saturated zone is oriented along the x_2 direction while the phase transforming zone is oriented along the x_1 direction, as seen in Figure 4.2. The orientation of the saturation and phase transition zones are important, particularly when viewed in context of the effect they have on the fracture toughening and crack tip shielding in Nitinol. Fracture toughening of materials occurs with the introduction of energy-absorbing or dissipating effects into the medium. By allowing phase transformation and thus dissipating energy at the crack tip, the crack tip is shielded.

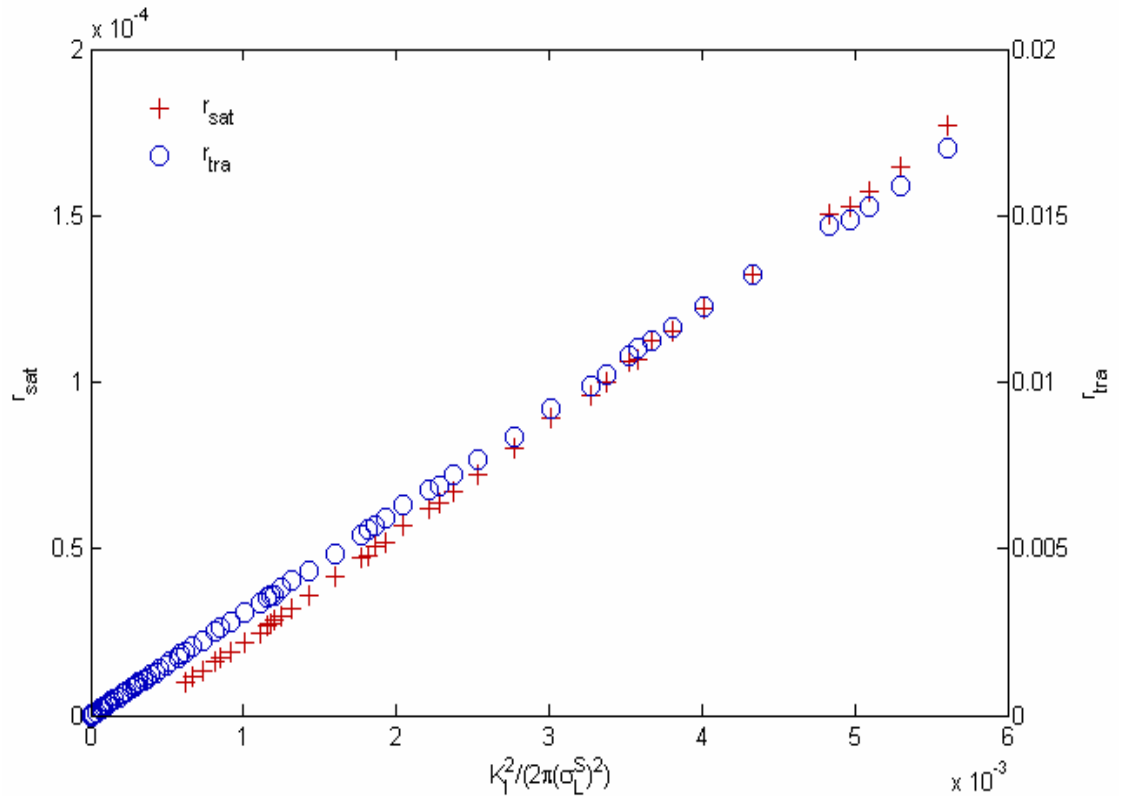


Figure 4.8. The radii of the saturation and the transition zones ahead of the crack tip ($\theta=0$) as a function of normalized length scale $\left(K_I^2 / 2\pi(\sigma_L^S)^2\right)$

4.3.4 *J-Integral*

The *J*-integral, developed by Rice [54], is a well-known expression for the characterization of the driving force on a crack in a solid. The *J*-integral for a two-dimensional crack in the x_1 - x_2 plane with the crack front parallel to the x_2 axis is the line integral,

$$J = \int_{\Gamma} (W dx_2 - T_i \frac{\partial u_i}{\partial x_1} ds) \quad (4.8)$$

where W is the strain energy density per unit volume, Γ is the path of the integral which encloses or contains the crack tip, and \mathbf{T} is the outward traction vector on ds . The *J*-integral is a path-independent line integral in a homogeneous and non-dissipative medium that represents the energy release rate per unit virtual crack advance. In the case of a linearly elastic solid under plane stress, the *J*-integral can be directly related to the applied (global) K_I [53, 55],

$$J = \frac{K_I^2}{E} \quad (4.9)$$

ABAQUS computes the *J*-integral around the crack tip as a post-processing activity, based on domain integrals. The stresses, strains, and internal energies are used in the calculation of the *J*-integral. The constitutive law is not directly considered. For the computation of the stresses, strains, and internal energies, there is an evolution of strains imposed, and the constitutive law then determines what the stresses are. The material routine also returns the elastic strain energy and the inelastic strain energy, the sum of which is the internal energy.

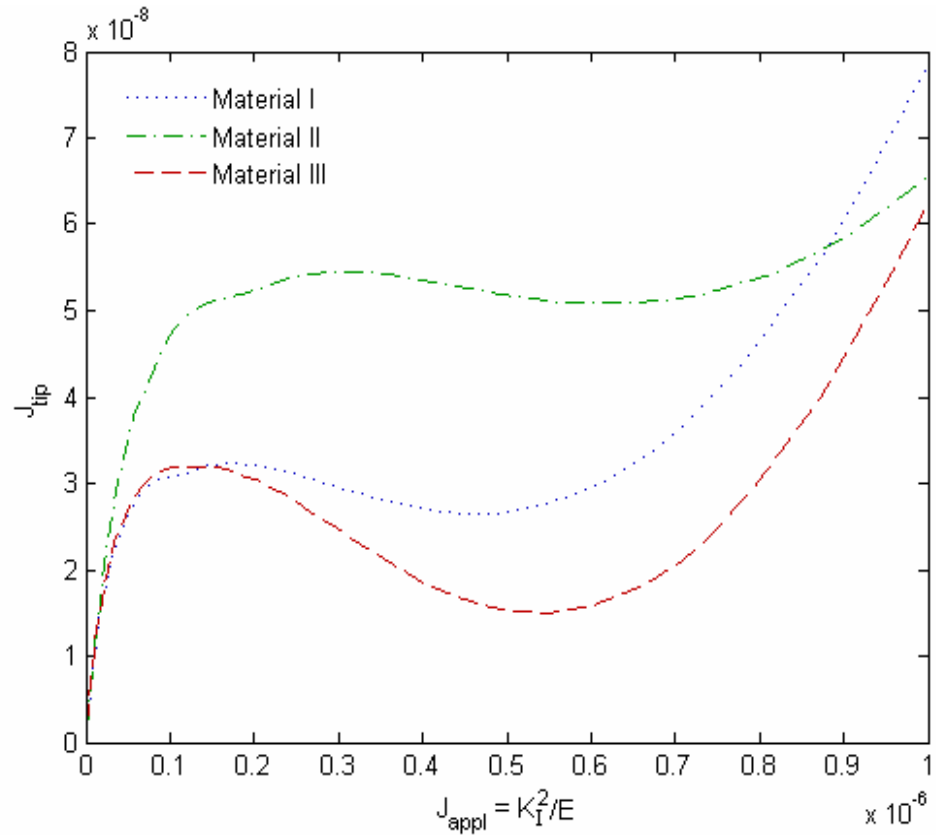


Figure 4.9. J_{tip} versus $J_{applied}$ (K_I^2/E_A) for various materials (I, II, III) of the material parameters. Note that J_{tip} is normalized with E_A and R .

The curve marked as Material I in Figure 4.9 shows the variation in the J -integral calculated directly around the crack tip versus the globally applied J . The globally applied J is taken to be (K_I^2 / E_A) under plane stress (Equation 4.9), where E_A has been non-dimensionalized to 1. Note that the value of the J -integral at the crack tip can be significantly smaller than the applied J . This reflects the fact that the material is no longer homogeneous following transformation. It has been verified that J_{tip} (respectively $J_{applied}$) is path independent as long as the path is chosen to lie within the fully transformed region (respectively untransformed region). The reduced value of J_{tip} compared to $J_{applied}$ reflects the shielding provided by the transformation. This is one contribution to toughening. A second

contribution arises in steady crack propagation due to dissipation (hysteresis) which has not been considered here.

4.4 Sensitivity to Material Parameters

Two additional materials representing the range of material behavior of Nitinol in addition to material I (Figure 4.1) are considered to explore the effects of material parameters describing their constitutive behavior, which are shown in Figure 4.10 in the form of uniaxial stress-strain curves. For material II, the parameters are the same as in material I except that the entire hysteresis loop is shifted upwards by 100 MPa. This would correspond to a case where the material in material I is deformed at a higher temperature ($T \sim 40^\circ\text{C}$). For material III, parameters are the same as in material I except that the transformation strain ϵ^{\perp} is halved from 0.04 to 0.02.

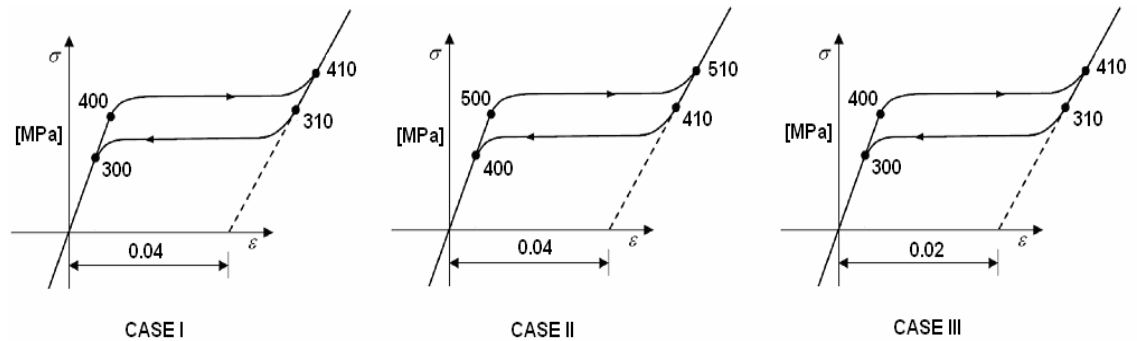


Figure 4.10. Typical stress-strain curves of Nitinol (materials I, II, and III) used to study the effect of material parameters on small scale transformation analysis

The dependence of $\sigma_{22}(K_I, r)$ plotted versus the angle θ on material parameters can be seen in Figures 4.11a - c. The martensite, transition, and austenitic regions were determined by tracing the circular arc around the farthest element from the crack with the appropriate

strain. This approximates the regions as semi-circles. It was seen in Figure 4.4 that for a constant set of material parameters, in any given region, the normalized $\sigma_{22}(K_I, r)$ is independent of K_I . As seen in Figure 4.11, changing the material parameters affects σ_{22} only in the martensitic region, where the stresses in the martensite region vary with ε^L . This is due to the dependence of the strain value at which saturation is complete on ε^L .

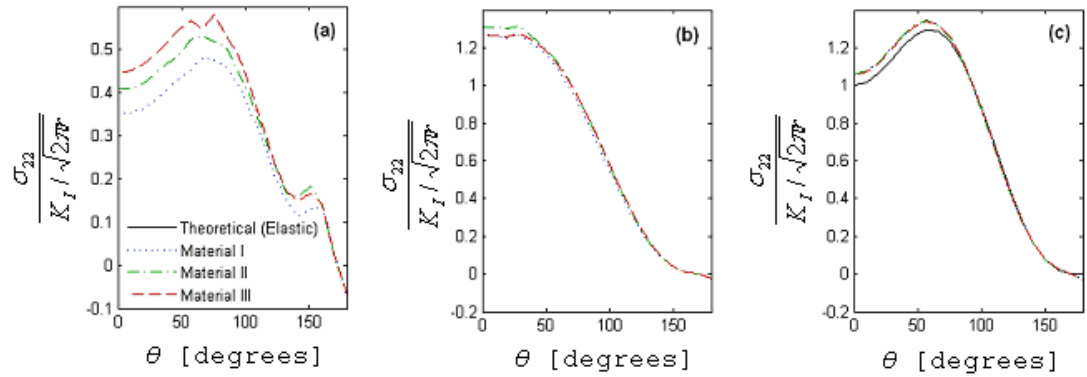


Figure 4.11. Angular variation of the normalized stress component σ_{22} versus θ for normalized $K_I=0.001$ in the (a) fully transformed (martensite), (b) partially transformed (mixed phase), and (c) untransformed (austenite) regions, for various materials (I, II, III) of the material parameters. The theoretical (elastic) solution is compared only in the austenitic region.

One can directly relate the strain at which saturation and phase transition is complete to the material parameters (Equation 4.10) as follows,

$$\begin{aligned} \varepsilon_{sat} &= \frac{\sigma_L^S}{E_A} \\ \varepsilon_{pt} &= \varepsilon_L + \frac{\sigma_L^E}{E_M} \end{aligned} \quad (4.10)$$

Figure 4.12a shows $\sigma_{22}(K_I, r)$ plotted versus the radial distance r in a logarithmic scale along $\theta=0$ for materials I and II. As expected, the translation to higher loading stresses causes an increase in $\sigma_{22}(K_I, r)$ along the crack tip. The general character of the curves with

respect to variation in K_I remains the same regardless of material parameters. In Figure 4.12b, halving ε^L decreases the size of the region of constant stress and shifts it farther from the crack tip.

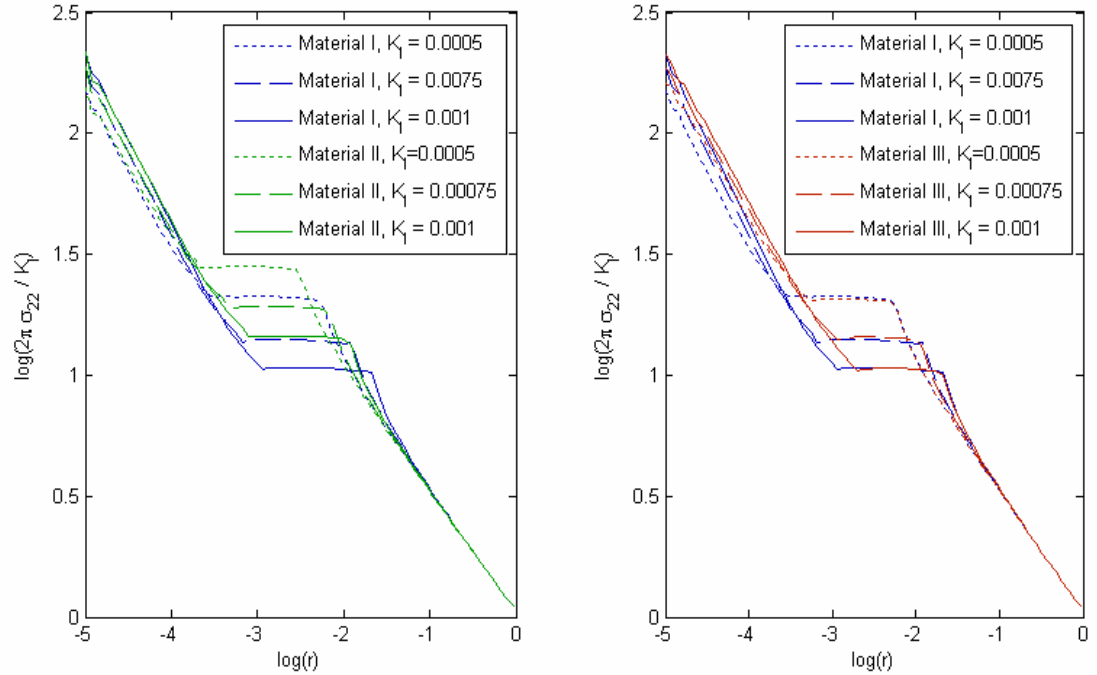


Figure 4.12. Normalized stress component σ_{22} as a function of distance ahead of the crack tip, along $\theta=0$, for normalized $K_I = [0.0005, 0.00075, 0.001]$ for various materials (I, II, III) of the material parameters

It can be seen from Figures 4.13a and b that the dependence of the radii of the saturated (r_{sat}) and phase transforming transition (r_{tru}) zones on K_I are highly sensitive to the material parameters, and have a linear dependence with $\frac{K_I^2}{2\pi(\sigma_L^S)^2}$. This is in contrast to plasticity, where the dependence of the size of the plastic zone would be fairly insensitive to the transformation stress. However, the dependence of the martensitic zone on σ_L^S is not surprising, considering the behavior of the region is strongly dependent on E_M and ν_M . From the data shown in Figs. 4.13a and b, the saturation and transforming zone radii can be

related to the applied far field stress intensity factor, K_I , for materials II and III in Equations 4.11 and 4.12 respectively,

$$r_{sat}^{II} = 0.036 \frac{K_I^2}{2\pi(\sigma_L^S)^2} \quad (4.11)$$

$$r_{tra}^{II} = 2.650 \frac{K_I^2}{2\pi(\sigma_L^S)^2}$$

$$r_{sat}^{III} = 0.057 \frac{K_I^2}{2\pi(\sigma_L^S)^2} \quad (4.12)$$

$$r_{tra}^{III} = 2.827 \frac{K_I^2}{2\pi(\sigma_L^S)^2}$$

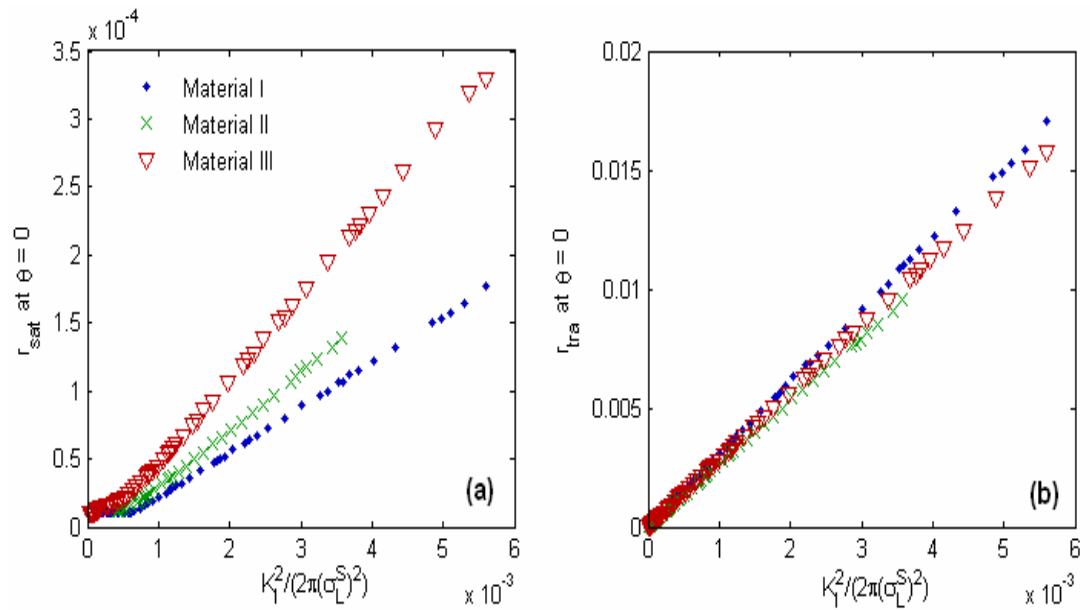


Figure 4.13. The radii of the saturation and transition zones ahead of the crack tip ($\theta=0$) as a function of normalized K_I for various materials (I, II, III) of the material parameters.

The radial development of the saturation zone along $\theta=0$ shown in Fig. 4.13a is examined first. For material II, the normalizing factor σ_L^S (where σ_L^S is the macroscopic plateau stress) is higher, and martensitic saturation occurs at a higher σ_L^E than in material I.

Because of these two factors, the equation for the $r_{sat}-K_I$ relationship has a higher slope, as seen in Equation 4.11 when compared to Equation 4.6. The slope for the $r_{sat}-K_I$ relationship in material III is even higher (Equation 4.12) because of the large effect that transformation strain has on the strain at which martensitic saturation is reached (Equation 4.10). Because of this, saturation zone begins to enlarge at lower K_I and higher amounts of transformation are achieved. These differences also influence the behavior of materials II and III in Figure 4.13b. For material II, the high σ_L^S result in a lower slope in the $r_{tra}-K_I$ relationship than for material I (Equation 4.7). In material III, the low ε^L makes saturation preferential, so that when K_I increases the saturation zone size increases, while the transition zone stays relatively small.

Figure 4.9 shows the variation in the J -integral calculated directly around the crack tip versus the globally applied J , as a function of material parameters. Since material II has a higher plateau stress than material I and hence the resulting J_{tip} vs. $J_{applied}$ graph is stretched. It takes more globally applied K_I to initiate the phase transformation, corresponding to a delayed and slightly higher first local maximum J_{tip} , and a delayed approach to eventually asymptote to 1 at higher values of $J_{applied}$. In material III, there is a lower transformation strain ε^L . There is no deviation of material III from material I at low values of $J_{applied}$, because the decreased ε^L does not affect the austenitic regime or the onset of phase transformation. The effect becomes apparent as we increase K_I and the phase transition zone begins to saturate earlier than it would in material I. The earlier saturation shields the crack tip and leads to a lower J_{tip} .

4.5 Conclusions

A small-scale transformation analysis for a crack in a shape memory alloy Nitinol subjected to mode-I loading under plane stress conditions was performed for the first time. The material parameters for a typical Nitinol alloy that undergoes stress-induced phase transformation (material I) was first considered and it was demonstrated that there is no variation with K_I in normalized $\sigma_{ij}(K_I, r)$ versus the angle θ , provided that the material parameters are held constant. However, for a set of constant material parameters, there is a variation in the stress $\sigma_{22}(K_I, r)$ versus r in front of the crack tip ($\theta = 0$) with K_I . As K_I increases, the radius at which phase transition occurs increases, but the stress $\sigma_{22}(K_I, r)$ at which transition occurs decreases. Regardless of K_I , the length of the transition region in front of the crack tip stays approximately the same. A linear relationship between the radii of the saturation and transition zones with respect to K_I^2 or $J_{applied}$ was found. A case study was then conducted to consider the sensitivity of these results to varying material parameters. It was discovered that $\sigma_{ij}(K_I, r)$ versus angle θ depends on material parameters only in the saturation region, and that $\sigma_{22}(K_I, r)$ in front of the crack tip depends heavily on material parameters. The general character of the variation of $\sigma_{22}(K_I, r)$ versus K_I does not change with material parameters. The relationship between J_{tip} and $J_{applied}$ was also explored, and the impact of these discoveries on the understanding of fracture toughening and crack shielding in Nitinol under plane stress conditions was discussed.

The present analysis has provided new and detailed insights concerning the structure of the crack tip fields and phase transformation under mode-I loading and plane stress conditions in shape memory alloys. This analysis should be further extended to plane strain and 3D under mixed mode loading conditions to provide a general framework of fracture mechanics in shape memory alloys such as Nitinol. The analysis also needs to be extended

to large-scale transformation and crack growth in such phase transforming alloys, which are also of practical interest in applications for design and evaluation. These aforementioned issues are subjects of ongoing investigations.

5 Summary

In this thesis, Digital Image Correlation was used to experimentally obtain, for the first time, full-field quantitative strain maps of localization in Nickel-Titanium (Nitinol). These strain mappings were used to track phase transformation propagation in thin sheets of Nitinol. The results painted a much more complex mechanism behind transformation than previously assumed, and gave numerous insights into the deformation and failure mechanisms of Nitinol. DIC can be easily extended to other shape memory alloys as a method of characterization. In addition to the experimental results, a finite element study was performed on the fracture of Nitinol. This study was one of the first of its type. It underscored the importance of cracktip shielding in martensitic transformation, and also raised a number of important questions that are reserved for future study.

In Chapter 2, we use Digital Image Correlation to study the quantitative full-field strain maps of thin sheets of Nitinol subjected to quasi-static uniaxial tension. We observe strain localization consistent with the work of other researchers, and for the first time have been able to probe its development in terms of strain. This has revealed a much more complex mechanism than assumed in the literature. We find that the transformation initiates in a macroscopically homogeneous but microscopically heterogeneous manner. The transformation proceeds through the nucleation and growth of localized bands of high strain. However, the strain within the bands at formation is significantly smaller than the value at saturation, and gradually increases as the band grows. The transformation is not complete even on apparent saturation of the stress-strain curve. The stress-strain behavior shows a dependence on orientation with respect to the rolling axis consistent with its texture. We find that the commonly used resolved stress criterion or Clausius-Clapeyron relation does not hold. We have probed the role of geometric defects and shown that

localization in shape-memory alloys is not purely a geometric instability, but a competition between material and geometric instabilities.

In Chapter 3, we experimentally investigated martensitic transformation around the crack tip in thin sheets of Nitinol. Many applications of Nitinol require its use in the form of thin sheets. One of the important failure criteria for the analysis and design of such devices is the fracture toughness, of which there are currently no recorded values for thin sheets on the order of 100 microns thickness. Using edge-cracked specimens, an average fracture toughness (K_{IC}) value of $51.4 \pm 3.6 \text{ MPa}\sqrt{\text{m}}$ for fine-grained polycrystalline Nitinol sheets ($A_f = 11.4 \text{ }^\circ\text{C}$) at room temperature was measured.

The use of DIC in these fracture experiments enabled a non-contact optical method of obtaining information about the crack tip fields in these thin sheets under displacement-controlled uniaxial tension. The shape of the transformation zone can be described in the form of three lobes, one along the x_1 axis that grows larger with the load, and two lobes pointing at 60 degrees from the x_1 axis that appear at larger values of K_I . Using the strain fields obtained from DIC, and assuming that phase transformation occurs from 1.5% to 4.5% strain, the approximate lengths of the saturation and transformation zones for various values of K_I were determined. The use of DIC enabled the first full-field quantitative mapping of the strain fields in the vicinity of the crack tip of edge-cracked specimens of Nitinol. The images, combined with the relatively high value of fracture toughness for thin sheets of Nitinol, indicate a complex mechanism where phase transformation contributes to toughening around the crack tip. The criteria for phase transformation and saturation near the crack tip need further investigation. The results presented here, including the full-field evolution of strain fields, could provide important insights for developing appropriate fracture criteria, as well as for phase transformation under multi-axial loading conditions.

In Chapter 4, a small-scale transformation analysis for a crack in a shape-memory alloy Nitinol subjected to mode-I loading under plane stress conditions was performed for the first time. The material parameters for a typical Nitinol alloy that undergoes stress-induced phase transformation (material I) was first considered and it was demonstrated that there is no variation with K_I in normalized $\sigma_{ij}(K_I, r)$ versus the angle ($\theta < \pi$) provided that the material parameters are held constant. However, for a set of constant material parameters, there is a variation in the stress $\sigma_{22}(K_I, r)$ versus r in front of the crack tip ($\theta = 0$) with K_I . As K_I increases, the radius at which phase transition occurs increases, but the stress $\sigma_{22}(K_I, r)$ at which transition occurs decreases. Regardless of K_I , the length of the transition region in front of the crack tip stays approximately the same. A linear relationship between the radii of the saturation and transition zones with respect to K_I^2 or $J_{applied}$ was found. A case study was then conducted to consider the sensitivity of these results to varying material parameters. It was discovered that $\sigma_{ij}(K_I, r)$ versus angle θ depends on material parameters only in the saturation region, and that $\sigma_{22}(K_I, r)$ in front of the crack tip depends heavily on material parameters. The general character of the variation of $\sigma_{22}(K_I, r)$ versus K_I does not change with material parameters. The relationship between J_{tip} and $J_{applied}$ was also explored, and the impact of these discoveries on the understanding of fracture toughening and crack shielding in Nitinol under plane stress conditions was discussed.

There are several topics of interest when considering directions for ongoing and future research. Experiments directly following the line of thought of those described in this thesis would be to (a) repeat these experiments in compression, shear, and torsion, and (b) to study of the effect of grain size on the tensile response of thin sheets. Also of immediate interest is to explore the effect of sample aspect ratio, temperature, and strain rate on phase transformation. Initial studies on the effect of sample aspect ratio on band formation have

been performed. Quasi-static uniaxial tension tests on dogbone-shaped specimens of Nitinol that are significantly larger and thicker (≈ 1 mm) show the same pattern of formation and propagation as that which appears in the thin sheet samples, and appear to show the same (scaled) band spacing. However, in future work, it would be interesting to see the effects of plane strain conditions on stress-induced martensitic phase propagation in Nitinol.

The effect of temperature can be viewed through a combination of Digital Image Correlation and thermal imaging. There have been recent experiments using high-sensitivity infrared imaging to view phase boundary propagation in Nitinol through tracking the release of latent heat [9], but these are largely qualitative measurements. Combining these measurements with the deformation mappings captured by Digital Image Correlation would provide a means of comparing energy of transformation from spatially averaged macroscopic plots with energy attributed to the release of latent heat, captured by thermal imaging. Another interesting experiment would be to coat the samples in silicon before testing, thereby preventing the release of latent heat. Additionally, there has been recent interest in the development of Digital Image Correlation at high temperatures. The main challenge for testing at temperatures greater than nominally 100°F is to find stable, traceable surface features that do not change with extended periods at high temperature. Traditional painting materials tend to shrink first, and then break down and release noxious fumes as temperatures increase. An option is to use high-temperature paints like those used in fireplaces, but the thickness and consistency of these paints makes coating samples with suitably small trackers difficult.

Interest in Digital Image Correlation is steadily increasing in experimental mechanics as a non-intrusive, highly scalable way of looking at surface deformation. One of the current challenges is to apply DIC to investigate strain rate sensitivity, particularly the dynamic

response of materials. There are several experimental challenges in this field, including image acquisition, lighting techniques, and the integration of cameras into the testing setup.

However, once these issues are resolved, Digital Image Correlation is a promising way to get both meso- and macro-scale measurements of deformation. Unlike strain gages, which are a traditional method of measuring strain in techniques like Hopkinson bar testing, DIC is non-contact. Using DIC also gives both a meso-scale and macro-scale full-field picture of the strain, versus the local strain values determined by strain gages. Digital Image Correlation is a promising technique in experimental mechanics because it is so scalable in terms of space and time, and also because it is capable of giving full-field quantitative information.

Although this thesis has been concerned primarily with macroscopic tests, an example of possible future small-scale work is to use photolithography to transfer a random gold masking on to a sample of Nitinol or other active material for SEM testing.

Currently, we are utilizing a combination of transmission x-ray and digital image correlation to obtain simultaneous macro-, meso-, and micro-scale observations of the deformation, transformation, and plasticity mechanisms of Nitinol. A joint research project at the Stanford Synchrotron Radiation Laboratory (SSRL), a division of the Stanford Linear Accelerator Center (SLAC) operated by Stanford University for the Department of Energy, has been undertaken in collaboration with industry leaders Nitinol Devices and Components (NDC) towards this end. The Stanford Synchrotron Radiation Laboratory is a facility where electrons circulate in a storage ring at nearly the speed of light, producing extremely bright, high-energy x-rays that can be used for transmission microscopy on relatively thick sheet samples.

Figure 5.1 shows the setup for these simultaneous experiments. The sample is placed in a custom micrometer rig, which is attached to a load cell and placed inside the hutch

between the beam emitter and beam stop. The sample is loaded by displacement control to a predetermined amount, and pictures are taken throughout this loading process for on-the-spot digital image correlation, in order to get a pseudo real-time idea of the mesoscopic transformation.

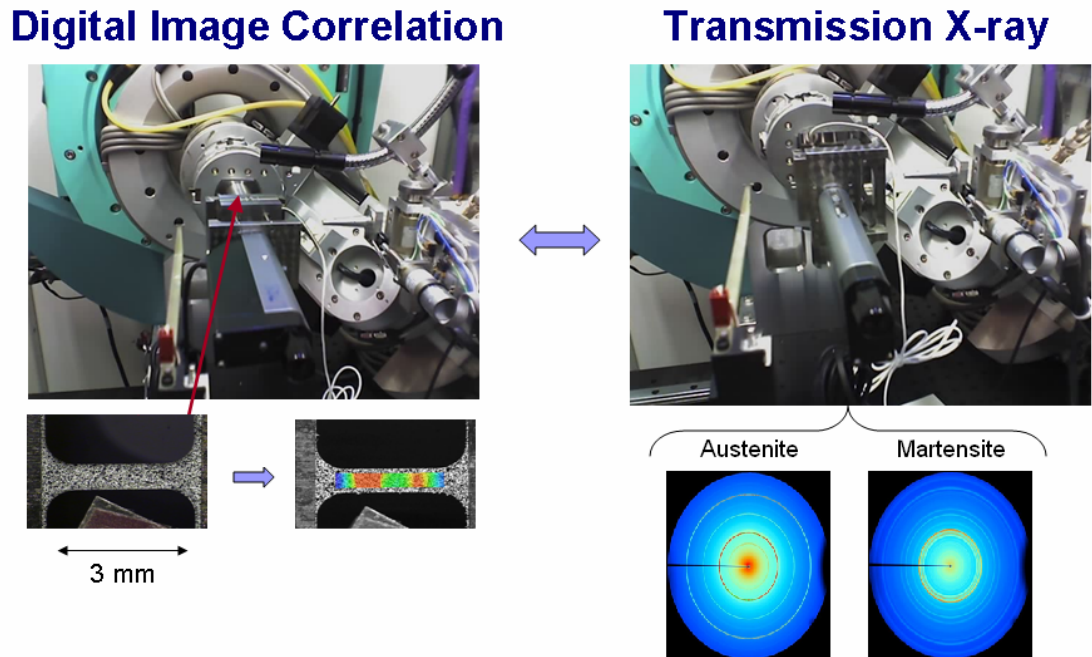


Figure 5.1: Simultaneous digital image correlation and transmission x-ray setup at the Stanford Synchrotron Radiation Laboratory (SSRL)

When the displacement reaches a pre-determined level, images are no longer taken. With the displacement held constant, the micrometer rig is rotated 90 degrees to the right, and x-ray diffraction data is taken. Because there is stress relaxation during the x-ray collection process, the load is continually recorded. When the x-ray data collection is completed, the sample is rotated 90 degrees to the left, and a new reference image is taken. The sample is then loaded under displacement control to another pre-determined stop point while

simultaneously collecting images for DIC, and this process is repeated until the sample breaks.

Because images for DIC are taken during loading, and transmission x-ray is taken during subsequent pauses in the loading, there is stress relaxation in the resulting macroscopic stress-strain curve that one needs to be aware of. The macroscopic stress strain curve is obtained through a similar process to that described in the experimental observations of strain localization in dogbone specimens of Nitinol sheet (Chapter 2). The strain values at each pixel are extracted from each DIC image and spatially averaged to get one average strain value, which is then plotted against the engineering stress value calculated from the load cell readout at the time the DIC image was taken. This process can be done in approximately five minutes, providing a useful feedback detailing local strain inside the gage section to help determine the next loading step.

The current experiments combining digital image correlation and transmission x-ray are not limited to Nitinol. In order to get a better fundamental understanding of deformation and plasticity mechanisms in nanocrystalline materials, iron (BCC), titanium (HCP), and aluminum (FCC) are also being investigated. Preliminary results indicate that the local averaged strain values from DIC plotted against stress obtained from the load cell can yield values for the Young's modulus of these materials that is consistently within 0.5% of the actual known value. This is another indication of the viability of this process. Digital image correlation is a perfect partner to transmission x-ray, since one of the main issues when looking at strain localization inside of these samples is knowing where to look, given the small spot size that transmission x-ray is capable of and the high demand for time on the synchrotron.

From the experiments performed in Chapter 2, it is clear that the transformation mechanism for polycrystalline SMAs is much more complex than previously assumed. There is much work that needs to be done in building a theoretical model to explain the onset and saturation of localization in these polycrystals. Understanding the phenomenology behind these transformations is instrumental in understanding the strain localization observed in experiments, and in developing finite element methods that accurately predict this localization.

The finite element analysis discussed in Chapter 4 is one of the first fracture analyses of Nitinol, and provides new and detailed insights concerning the structure of the crack tip fields and phase transformation under mode-I loading and plane stress conditions in shape memory alloys. However, it should be further extended to plane strain and 3-D under mixed mode loading conditions in order to provide a general framework of fracture mechanics in shape memory alloys such as Nitinol. The analysis also needs to be extended to large scale transformation and crack growth in such phase transforming alloys, which are also of practical interest in applications for design and evaluation. These aforementioned issues are subjects of ongoing investigations.

Nickel-Titanium is a specific example of the fact that virtually every material is made up of different structures at different length scales. Understanding the link between these scales, or how the behavior at one scale affects the properties of another, is an important issue. This is especially relevant as we enter a generation where greater demands are being put on material functionality, particularly in biomedical and small-scale applications. Establishing a relationship between the microscopic behavior of a material and its macroscopic properties facilitates the development of these types of new materials and the prediction of their behavior in practical applications. Digital Image Correlation (DIC), due to

its highly scalable and non-intrusive nature, is a promising experimental means of exploring deformation. Combining Digital Image Correlation with other methods of characterization, like electron microscopy, will paint a much more complete picture of the multi-scale interactions in the future.

6 References

- [1] Kauffman G and Mayo I. The story of Nitinol: the serendipitous discovery of the memory metal and its applications. *The Chemical Educator* 1996; 2 (2).
- [2] Pelton A, Duerig T, and Steckel D. A guide to shape memory and superelasticity in Nitinol medical devices. *Minimally Invasive Therapy & Allied Technologies* 2004; 13:218 - 221.
- [3] Duerig T, Pelton A, and Steckel D. Superelastic Nitinol for medical devices. *Medical Plastics and Biomaterials Magazine* March 1997.
- [4] Advanced Materials and Technologies. Herk-de-Stad, Belgium, <http://www.amtbe.com>.
- [5] Miyazaki S, Kimura S, Takei F, Muira T, Otsuka K, and Suzuki Y. Shape memory effect and pseudoelasticity in a Ti-Ni Single-Crystal. *Scripta Mat.* 1983; 17:1057 - 1062.
- [6] Shield TW. Orientation dependence of the pseudoelastic behavior of single-crystals of Cu-Al-Ni in tension. *J. Mech. Phys. Solids* 1995; 43 (6):869 - 895.
- [7] Shaw JA and Kyriakides S. Thermomechanical aspects of NiTi. *J. Mech. Phys. Solids* 1995; 43:1243 – 1281.
- [8] Shaw JA and Kyriakides S. On the nucleation and propagation of phase transformation fronts in a NiTi alloy. *Acta Metall.* 1997; 45(2):683 – 700.
- [9] Pieczyska EA, Gadaj SP, Nowacki WK, and Tobushi H. Thermomechanical investigations of martensitic and reverse transformations in TiNi shape memory alloy. *Bull. Pol. Acad. Sci., Tech. Sci.* 2004; 52(3):165 - 171.
- [10] Brinson LC, Schmidt I, and Lammering R. Stress-induced transformation behavior of a polycrystalline NiTi shape memory alloy: micro and macromechanical investigations via in situ optical microscopy. *J. Mech. Phys. Solids* 2004; 52(7):1549 - 1571.
- [11] Feng P and Sun QP. Experimental investigation on macroscopic domain formation and evolution in polycrystalline NiTi microtubing under mechanical force. *J. Mech. Phys. Solids* 2006; 54(8):1568 - 1603.
- [12] Yi S and Gao S. Experimental study on the anisotropic behavior of textured NiTi pseudoelastic shape memory alloys. *Mat. Sci. and Eng. A.* 2003; 362: 107 - 111.
- [13] Jiang XP, Hida M, Takemoto Y, Sakakibara A, Yasuda H, and Mori H. In situ observation of stress-induced martensitic transformation and plastic deformation in a TiNi alloy. *Mat. Sci. Engrg. A – Structural Materials Properties Microstructure and Processing* 1997; 238 (2): 303 - 308.
- [14] Schmahl WW, Khalil-Allafi J, Hasse B, Wagner M, Heckmann A, and Somsen C. Investigation of the phase evolution in a super-elastic NiTi shape memory alloy (50.7 at.%)

- Ni) under extensional load with synchrotron radiation. *Mat. Sci. Engng. A*. 2004; 378 (1-2):81 – 85.
- [15] Schryvers D, Tirry W, and Yang ZQ. Measuring strain fields and concentration gradients around Ni₄Ti₃ precipitates. *Mat. Sci. and Engrg. A – Structural Materials Properties Microstructure and Processing* 2006; 438: 485 - 488.
- [16] Xiong F, Liu Y, and Pagounis E. Thermally induced fracture of single crystal Ni-Mn-Ga ferromagnetic shape memory alloy. *J. Alloys and Compounds* 2006; 415:188 - 192.
- [17] Loughran GM, Shield TW, and Leo PH. Fracture of shape memory CuAlNi single crystals. *Int. J. Solids Struct.* 2003; 40 (2): 271 - 294.
- [18] Vasko GM, Leo PH, and Shield TW. Prediction and observation of crack tip microstructure in shape memory CuAlNi crystals. *J. Mech. Phys. Solids* 2002; 50 (9) 1843 - 1867.
- [19] Shek CH, Lin GM, Lai JKL, and Tang ZF. Fractal fracture and transformation toughening in CuNiAl single crystal. *Metall. Mat. Trans. A – Physical Metallurgy and Materials Science* 1997; 28 (6): 1337 - 1340.
- [20] Leo PH, Shield TW, and Bruno OP. Transient heat-transfer effects on the pseudoelastic behavior of shape-memory wires. *Acta Metall. et. Mat.* 1993; 41(8):2477 - 2485.
- [21] Shaw JA and Kyriakides S. Initiations and propagation of localized deformation in elasto-plastic strips under uniaxial tension. *Int. J. Plast.* 1997; 13 (10): 837 - 871.
- [22] Sittner P, Liu Y, and Novak V. On the origin of Luders-like deformation of NiTi shape memory alloys. *J. Mech. Phys. Solids* 2005; 53 (8):1719 – 1746.
- [23] Niemczura J and Ravi-Chandar K. Dynamics of propagating phase boundaries in NiTi. *J. Mech. Phys Solids* 2006; 54:2136 – 2161.
- [24] Barney M. and Mehta A., *Private Communication*.
- [25] Sutton MA, Cheng MQ, Peters WH, Chao YJ, and McNeill SR. Application of an optimized digital image correlation method to planar deformation analysis. *Img. Vis. Comp.* 1986; 4(3):143 - 151.
- [26] Shabalovskaya SA, Anderegg J, Laab F, Thiel PA, and Rondelli G. Surface conditions of Nitinol wires, tubing, and as-cast alloys. The effect of chemical etching, aging in boiling water, and heat treatment. *J. Biomed. Mater. Res B* 2003; 65B(1):193 - 203.
- [27] Correlated Solutions. West Columbia, South Carolina, www.correlatedsolutions.com.
- [28] Sittner P and Novak V. Anisotropy of martensitic transformations in modeling of shape memory alloy polycrystals. *Int. J. Plast.* 2000; 16 (10-11):1243 - 1268.

- [29] Bhattacharya K and Kohn RV. Symmetry, texture and the recoverable strain of shape-memory polycrystals. *Acta Mat.* 1996; 44(2):529 - 542.
- [30] Shu YC and Bhattacharya K. The influence of texture on the shape-memory effect in polycrystals. *Acta Mat.* 1998; 46(15):5457 - 5473.
- [31] Novak V and Sittner P. A network micromechanics model of thermomechanical behaviors of SMA polycrystals. *Scripta Mat* 2004; 50 (2): 199 - 206.
- [32] Bhattacharya K and Schlömerkemper A. Transformation yield surface of shape memory alloys. *JPhy4* 2004; 115:155 - 162.
- [31] Schlömerkemper A. *PAMM Proc. Appl. Math. Mech.* 2006; preprint.
- [32] Chopra HD, Bailly C, and Wuttig M. Domain structures in bent In-22.5 at.%Ti polydomain crystals. *Acta Mat.* 1996; 44 (2):747 - 751.
- [33] McKelvey AL and Ritchie RO. Fatigue-crack growth behavior in the superelastic and shape-memory alloy Nitinol. *Metall. and Mat. Trans.* 2001; A 32 (3A), 731 - 743.
- [34] McKelvey AL and Ritchie RO. Fatigue-crack propagation in Nitinol, a shape-memory and superelastic endovascular stent material. *J. of Biomedical Mat. Research* 1999; 47 (3): 301.
- [35] Melton KN and Mercier O. Fatigue of NiTi thermoelastic martensites. *Acta Metall.* 1979; 27(1): 137 - 144.
- [36] Filip P. Fatigue crack propagation in pseudoelastic TiNi smart microcomponents. *Zeitschrift für Metallkunde* 2004; 95:356 - 361.
- [37] Robertson SW and Ritchie RO. In vitro fatigue-crack growth and fracture toughness behavior of thin-walled superelastic Nitinol tube for endovascular stents: A basis for defining the effect of crack-like defects. *Biomaterials* 2007; 28 (4): 700 - 709.
- [38] Eggeler G. Structural and functional fatigue of NiTi shape memory alloys. *Mat. Sci. and Eng. A – Struct. Mat. Prop. Microstructure and Processing* 2004; 378: 24.
- [39] Shen LC, He JY, Su YJ, Chu W, and Qiao L. In-situ study of cracking for Ni₂MnGa ferromagnetic shape memory alloy. *Acta Metall. Sin.* 2006; 42(8):810 - 814.
- [40] Lu YH, Qiao LJ, and Chu WY. Characteristics of microcrack initiation in CuNiAl shape memory alloy. *Fatigue and Fracture of Eng. Mat. Struct.* 2002; 25 (5): 509 - 518.
- [41] Crone WC, Brock H, and Creuziger A..Nanoindentation and microindentation of CuAlNi shape memory alloy. *Exp. Mech.* 2007; 47 (1): 133 - 142.

- [42] He JY, Gao KW, Su YJ, Qiao LJ, and Chu WY. The effect of hydride and martensite on the fracture toughness of TiNi shape memory alloy. *Smart Mater. Struct.* 2004; 13 (2): N24 - N28.
- [43] He JY, Gao KW, Su YJ, Qiao L, and Chu WY. Hydrogen-induced delayed fracture in TiNi shape memory alloy. *Acta Metall. Sinica* 2004; 40 (4): 342 - 346.
- [44] Shih, GC. *Handbook of stress-intensity factors for researchers and engineers*. Institute of Fracture and Solids Mechanics, Lehigh University, Bethlehem, PA, 1973.
- [45] Yi S and Gao S. Fracture toughening mechanism of shape memory alloys due to martensite transformation. *Int. J. Solids Struct.* 2000; 37(38): 5315 - 5327.
- [46] Yi S and Gao S. Shen LX. Fracture toughening mechanism of shape memory alloys under mixed-mode loading due to martensite transformation. *Int. J. Solids Struct.* 2001; 38 (24-25): 4463 - 4476.
- [47] Birman V. On mode I fracture of shape memory alloy plates. *Smart Mater. Struct.* 2001; 7: 433 - 437.
- [48] Tanaka K and Sato Y. Analysis of superplastic deformation during isothermal martensitic transformation. *Res. Mech.* 1986; 17(3): 241 - 252.
- [49] Dang P and Grujicic M. Transformation toughening in the gamma-TiAl-beta-Ti-V system .2. A molecular dynamics study. *J. Mat. Sci.* 1997; 32 (18): 4875 - 4887.
- [50] Auricchio F and Taylor R.L. Shape-memory alloys: modeling and numerical simulations of the finite-strain superelastic behavior. *Comput. Methods. Appl. Mech. Engrg.* 1997; 143 (1 - 2):175 - 194.
- [51] Auricchio F, Taylor R.L, and Lubliner J. Shape-memory alloys: macromodelling and numerical simulations of the superelastic behavior. *Comput. Methods Appl. Mech. Engrg.* 1997; 146 (3 - 4):281 - 312.
- [52] ABAQUS. UMAT and VUMAT routines for the simulation of Nitinol. *Answer ID# 1658*, Abaqus, Inc, Pawtucket, RI.
- [53] Wang XM, Wang YF, Baruj A, Eggeler G, and Yue Z. On the formation of martensite in front of cracks in pseudoelastic shape memory alloys. *Mat Sci Eng A – Struct* 2005; 394 (1 - 2): 393 - 398.
- [54] Rice JR. A path independent integral and approximate analysis of strain concentration by notches and cracks. *J. Appl. Mech.* 1968; 35:379 - 386.
- [55] Otsuka K andWayman CM. Mechanism of shape memory effect and superelasticity. In: Otsuka K and Wayman CM, Ed. *Shape Memory Materials*. Cambridge University Press, 1998.

[56] Bhattacharya K. *Microstructure of Martensite: Why it forms and how it gives rise to the shape-memory effect*. Oxford University Press, 2004.

[57] Lawn BR. *Fracture of Brittle Solids*. Cambridge University Press, 1993.